

FAILURE PREDICTION FOR COMPOSITE MATERIALS  
WITH GENERALIZED STANDARD MODELS

A Dissertation

Submitted to the Faculty

of

Purdue University

by

Zhenyuan Gao

In Partial Fulfillment of the

Requirements for the Degree

of

Doctor of Philosophy

December 2019

Purdue University

West Lafayette, Indiana

**THE PURDUE UNIVERSITY GRADUATE SCHOOL  
STATEMENT OF DISSERTATION APPROVAL**

Dr. Wenbin Yu, Chair

School of Aeronautics and Astronautics

Dr. R. Byron Pipes

School of Aeronautics and Astronautics

Dr. Arun Prakash

School of Civil Engineering

Dr. Vikas Tomar

School of Aeronautics and Astronautics

**Approved by:**

Dr. Weinong Wayne Chen

Aeronautics and Astronautics Associate Head for Graduate Education

## ACKNOWLEDGMENTS

I am deeply grateful to my advisor Dr. Wenbin Yu for his guidance, support, and encouragement throughout my graduate studies at Purdue University. He showed me the way to become a professional and effective researcher, and provided me with various opportunities for career and personal development.

I would like to thank my committee members, Dr. R. Byron Pipes, Dr. Arun Prakash, and Dr. Vikas Tomar, for their advice, comments, and criticisms on my dissertation.

This work is supported, in part, by the US Army Research Laboratory. This support is gratefully acknowledged. Special thanks go to Dr. Robert A. Haynes for the fruitful technical discussions and collaboration during the development of the present fatigue models.

I would like to thank Dr. Liang Zhang for his continuous guidance and collaboration during my graduate studies.

I would also like to thank Dr. Victor Oancea from Dassault Systemes for his support and collaboration during and after my internship at the company.

Last but not the least, I would like to express particular gratitude to my wife, Ziping Hua, for her caring and support during my Ph.D study, and in my life.

## TABLE OF CONTENTS

	Page
LIST OF TABLES . . . . .	vii
LIST OF FIGURES . . . . .	viii
ABSTRACT . . . . .	xi
1 INTRODUCTION . . . . .	1
1.1 Overview . . . . .	1
1.2 Brittle fracture . . . . .	3
1.3 Fatigue damage . . . . .	6
1.4 Interlaminar delamination . . . . .	10
1.5 Fatigue delamination . . . . .	14
2 NONLOCAL DAMAGE MODEL . . . . .	17
2.1 Thermodynamics and energy equivalence . . . . .	17
2.2 Nonlocal damage model . . . . .	20
2.3 Explicit integration scheme . . . . .	25
2.4 Numerical examples . . . . .	30
2.4.1 SiC–SiC woven composite . . . . .	30
2.4.2 SENB tests . . . . .	32
2.4.3 Mixed-mode fracture test on a DEN specimen . . . . .	41
2.5 Conclusions . . . . .	44
3 FATIGUE CONTINUUM DAMAGE MODEL . . . . .	48
3.1 Thermodynamics and energy equivalence . . . . .	48
3.2 Viscodamage model . . . . .	49
3.3 Governing equation for damage evolution . . . . .	49
3.4 Incremental constitutive relation . . . . .	51
3.5 Stress or strain decomposition . . . . .	54

	Page	
3.6	Partial derivatives . . . . .	55
3.7	Numerical examples . . . . .	57
3.7.1	Concrete in compression . . . . .	58
3.7.2	Concrete in tension . . . . .	62
3.7.3	Fiber-reinforced composite in tension . . . . .	65
3.8	Conclusions . . . . .	70
4	COHESIVE ZONE MODEL FOR QUASI-STATIC DELAMINATION . . . . .	71
4.1	Basic ideas and thermodynamics . . . . .	71
4.2	Damage model . . . . .	76
4.3	Cohesive law . . . . .	78
4.4	Path dependence function . . . . .	79
4.5	Numerical examples . . . . .	85
4.5.1	Calibration of interface parameters . . . . .	85
4.5.2	Validation examples . . . . .	91
4.5.3	Parametric study . . . . .	100
4.5.4	Conclusions . . . . .	103
5	COHESIVE ZONE MODEL FOR FATIGUE DELAMINATION . . . . .	107
5.1	String-based CZM . . . . .	107
5.2	Implicit integration scheme . . . . .	108
5.3	Partial derivatives . . . . .	112
5.4	UMAT algorithm . . . . .	113
5.5	Numerical examples . . . . .	115
5.5.1	Mode I fatigue delamination and calibration of interface parameters . . . . .	115
5.5.2	Mode II fatigue delamination . . . . .	120
5.5.3	Mixed mode fatigue delamination . . . . .	124
5.6	Conclusions . . . . .	125
6	CONCLUSIONS AND RECOMMENDATIONS OF FUTURE WORK . . . . .	128

	Page
6.1 Conclusions . . . . .	128
6.2 Recommendations of Future Work . . . . .	129
REFERENCES . . . . .	130
VITA . . . . .	141

## LIST OF TABLES

Table	Page
2.1	Predetermined material parameters of a SiC–SiC woven composite. . . . . 31
2.2	Specimen dimensions (all in mm) and numbers of elements. . . . . 34
2.3	Predetermined material parameters of a type of concrete. . . . . 35
2.4	Fitted parameters of a type of concrete. . . . . 37
3.1	Predetermined parameters of a concrete. . . . . 60
3.2	Fitted parameters of a concrete. . . . . 60
3.3	Predetermined parameters of another concrete. . . . . 62
3.4	Fitted parameters of another concrete. . . . . 63
3.5	Predetermined parameters of a fiber-reinforced composite. . . . . 68
3.6	Fitted parameters of a fiber-reinforced composite. . . . . 68
4.1	Predetermined interface parameters. . . . . 87
4.2	Fitted interface parameters. . . . . 89
4.3	Interface parameters for a bilinear cohesive law. . . . . 89
4.4	Experimental parameters. . . . . 92
4.5	$G_c$ (J/m <sup>2</sup> ) of the rightmost cohesive element from each test. . . . . 96
4.6	$G_c$ 's (J/m <sup>2</sup> ) of the rightmost five cohesive elements from the 50% MMB test. 99
4.7	Interface parameters in three cases. . . . . 101
5.1	Predetermined interface parameters . . . . . 116
5.2	Elastic constants of each laminate . . . . . 117
5.3	Calibrated interface parameters . . . . . 119
5.4	Assumed $G_c$ - $\beta_2$ and $J$ - $\beta_2$ relationships. . . . . 125

## LIST OF FIGURES

Figure	Page
1.1 Typical traction–separation relationships in CZMs. . . . .	11
2.1 A ply of a SiC–SiC woven composite (adapted from Ref. [110]). . . . .	30
2.2 Experimental and fitted stress–strain curves of a SiC–SiC woven composite.	33
2.3 Sketch of an SENB specimen. . . . .	34
2.4 Finite element model of the left half of the smallest SENB specimen. . . .	34
2.5 Experimental and fitted load–deflection curves of different specimens. . . .	37
2.6 Case 2 load–deflection curves for different values of $l_c$ . . . . .	38
2.7 Case 2 contour plots of $d_{11}$ at different stages of deformation (height: 160 mm). . . . .	39
2.8 Eventual fracture paths in different cases. . . . .	40
2.9 Sketch of a DEN specimen (adapted from Ref. [118]). . . . .	41
2.10 Typical fracture paths during a mixed-mode fracture test: solid line—front view; dash line—back view (duplicated from Ref. [118]). . . . .	42
2.11 Finite element model of a DEN specimen. . . . .	43
2.12 Contour plots of $d_{11}$ at different stages of deformation (height: 200 mm). .	45
2.13 Contour plots of $d_{22}$ at different stages of deformation (height: 200 mm). .	46
3.1 A horizontal crack subject to in-plane biaxial loading. . . . .	55
3.2 (a) S–N and (b) modulus degradation–cycle curves of a concrete in com- pression. . . . .	59
3.3 Empirical S–N curve. . . . .	62
3.4 (a) S–N and (b) maximum strain–cycle curves of a concrete in tension. . .	66
3.5 (a) S–N and (b) maximum strain–cycle curves of a fiber-reinforced com- posite in tension. . . . .	67
4.1 Craze ahead of a crack tip (adapted from Ref. [127]). . . . .	72
4.2 Schematic of a deformed cohesive element. . . . .	74

Figure	Page
4.3 Schematics of (a) a simple (proportional, monotonic) and (b) a complex (nonproportional, unloading–reloading) separation paths. . . . .	77
4.4 Traction–separation curve of a cohesive element deformed along a proportional, unloading–reloading separation path. The element has been deformed along $OP_1P_2$ till $t$ . It can either be unloaded and reloaded along $P_2OP_2$ or be further loaded along $P_2P_3$ , where $P_3$ is the failure point at time $t_c$ . Let $A_{(\cdot)}$ denote the area enclosed by a curve in the figure. At $t$ , $G = A_{OP_1P_2O}$ and $\Psi_e = A_{OP_2P_4O}$ ; at $t_c$ , $G_c = A_{OP_1P_2P_3O}$ and $(\Psi_e)_c \rightarrow 0$ (see Eq. (4.45)). . . . .	81
4.5 Critical energy release rate–mode mixture ratio curves predicted by different CZMs. . . . .	90
4.6 Traction–separation curves predicted by different CZMs. . . . .	90
4.7 Experimental settings. . . . .	93
4.8 Sample finite element model of an MMB specimen. . . . .	94
4.9 Applied load–load point displacement curves predicted by different CZMs. . . . .	95
4.10 Variation in the orientation of the rightmost cohesive element during each test. . . . .	97
4.11 Variations in the orientations of the rightmost five cohesive elements during the 50% MMB test. . . . .	99
4.12 Mode I traction–separation curves for different interfacial strengths. . . . .	102
4.13 Critical energy release rate–mixed-mode ratio curves for different interfacial strengths. . . . .	102
4.14 Applied load–load point displacement curves for different interfacial strengths. . . . .	103
4.14 Applied load–load point displacement curves for different interfacial strengths (continued). . . . .	104
4.14 Applied load–load point displacement curves for different interfacial strengths (continued). . . . .	105
5.1 UMAT algorithm. . . . .	114
5.2 Finite element model for the DCB specimen. . . . .	118
5.3 (a) G–N and (b) crack growth rate curves for DCB tests. . . . .	121
5.4 Compliance evolution curve for $G_{\text{Imax}} = 0.3G_{\text{Ic}}$ . . . . .	122
5.5 Crack growth rate curve for ENF tests. . . . .	124

Figure	Page
5.6 Sample finite element model for a MMB specimen. . . . .	126
5.7 Simulated crack growth rate curves for DCB and MMB tests. . . . .	126

## ABSTRACT

Gao, Zhenyuan Ph.D. candidate, Purdue University, December 2019. Failure Prediction for Composite Materials with Generalized Standard Models. Major Professor: Dr. Wenbin Yu.

Despite the advances of analytical and numerical methods for composite materials, it is still challenging to predict the onset and evolution of their different failure mechanisms. Because most failure mechanisms are irreversible processes in thermodynamics, it is beneficial to model them within a unified thermodynamic framework. Noting the advantages of so-called generalized standard models (GSMs) in this regard, the objective of this work is to formulate constitutive models for several main failure mechanisms: brittle fracture, interlaminar delamination, and fatigue behavior for both continuum damage and delamination, in a generalized standard manner.

For brittle fracture, the numerical difficulties caused by damage and strain localization in traditional finite element analysis will be addressed and overcome. A nonlocal damage model utilizing an integral-type regularization technique will be derived based on a recently developed “local” continuum damage model. The objective is to make this model not only rigorously handle brittle fracture, but also incorporate common damage behavior such as damage anisotropy, distinct tensile and compressive damage behavior, and damage deactivation. A fully explicit integration scheme for the present model will be developed and implemented.

For fatigue continuum damage, a viscodamage model, which can handle frequently observed brittle damage phenomena, is developed to produce stress-dependent fatigue damage evolution. The governing equation for damage evolution is derived using an incremental method. A class of closed-form incremental constitutive relations is derived.

For interlaminar delamination, a cohesive zone model (CZM) will be proposed. Focus is placed on making the associated cohesive elements capable of displaying experimental critical energy release rate–mode mixture ratio relationships. To achieve this goal, each cohesive element is idealized as a deformable string exhibiting path dependent damage behavior. A damage model having a path dependence function will be developed, which will be constructed such that each cohesive element can exhibit designated, possibly sophisticated mixed-mode behavior. The rate form of the cohesive law will be subsequently derived.

Finally, a CZM for interlaminar fatigue, capable of handling brittle damage behavior, is developed to produce realistic interlaminar crack propagation under high-cycle fatigue. An implicit integration scheme, which can handle complex separation paths and mixed-mode delamination, is developed. Many numerical examples will be utilized to clearly demonstrate the capabilities of the proposed nonlocal damage model, continuum fatigue damage model, and CZMs for quasi-static and fatigue delamination.

# 1. INTRODUCTION

## 1.1 Overview

Composite materials are widely used in aerospace and automotive industries due to their high strength-to-weight ratio, improved ultimate strength, improved resistance to corrosion, or improved thermomechanical properties. Since the birth of composite materials, research on their various failure mechanisms has attracted significant attention. While the different forms of failure and their causes have been well established over the years, the prediction of the onset and evolution of such phenomenon is still an ongoing challenge. Analytically, applying traditional mechanical theories (e.g., fracture mechanics, continuum damage mechanics, plasticity theory, etc.) to composite materials requires more robust and rigorous extensions to account for the complex stress states and material interfaces. Numerically, conventional finite element method (FEM) often meets with difficulties when modeling damage and fracture in composite materials due to mesh induced directional bias and strain/damage localization, which has motivated researchers to develop mesh-less methods (e.g., peridynamics [1]), or to extend FEM with various nonlocal damage models [2]. Moreover, different failure mechanisms also poses additional challenges on their constitutive modeling and numerical implementation. The failure mechanisms in composite materials of interest in this work are:

1. Brittle fracture: failure that often happens within matrix materials due to their relatively lower strength, or due to transverse loading with respect to fiber directions in fiber-reinforced composites;
2. Interlaminar delamination: the formation and growth of cracks along the laminar interfaces under static or cyclic loads, especially in fiber-reinforced com-

posite laminates, which is mainly caused by insufficient reinforcement in their thickness directions;

3. Fatigue damage: the formation and coalescence of micro-cracks at one or more locations within composite materials after exposure to extensive cyclic loading, which can happen both within interfaces or at the continuum level.

While different constitutive models are usually developed for different failure mechanisms, it is beneficial to develop models based on a unified theory that governs such irreversible processes. For this reason, so-called generalized standard models (GSMs) have been attracting considerable attention for decades. Halphen and Nguyen [3] first introduced the concept of GSM, and several authors [4–8] enriched this concept in succession. Following Ref. [6], a rate-independent damageable material is said to be generalized standard only if:

1. there exist a potential function specifying the relation between each pair of state variable (e.g., the elastic stain tensor and the damage factor/tensor) and its conjugated thermodynamic driving force (e.g., the stress tensor and the damage conjugate force (tensor)), and a damage function specifying the proportionality limit (damages initiate and evolve beyond this limit);
2. the material obeys the principle of maximum dissipation.

According to Ref. [6], such a generalized standard model possesses the following advantageous features:

1. it specifies the potential function, the damage function, and the damage evolution laws in a mathematically rigorous manner;
2. it leads to an associated flow rule and the Kuhn–Tucker loading/unloading conditions and therefore eliminates the arbitrariness in the selection of the flow rule and the loading/unloading conditions;
3. it regularizes damage evolution along nonproportional loading paths by requiring the material to obey a unified principle.

With GSM, it is possible to derive constitutive relations for the aforementioned failure mechanisms using the same thermodynamic framework. In the following sections of this chapter, popular models previously developed by researchers for different failure mechanisms will be reviewed, and methods to extend the models to generalized standard forms will be briefed.

## 1.2 Brittle fracture

Continuum damage mechanics (CDM) is concerned with the modeling of various damage behavior of various materials. A number of pioneer authors [5, 9–19] established the theoretical framework of CDM based on the thermodynamics of irreversible processes. The laws of thermodynamics describe how the state variables selected for a thermodynamic system behave under various conditions. The elastic strain tensor, the damage tensor, the plastic hardening state variable(s), and the damage accumulation state variable(s) form a complete set of state variables for a damageable material. A generalized standard continuum damage model regularizes an irreversible process obeying thermodynamics. It relies on the existences of: 1. a free energy specifying the relation between each pair of state variable and its conjugated thermodynamic driving force; 2. a dissipation potential describing the irreversible process [20]. Theoretically speaking, there exists a state coupling between two phenomena if the free energy contains one or more product terms of the variables describing these phenomena; there exists a dissipation coupling if there exist multiple dissipation potentials [20].

Despite advances in CDM, locally defined continuum damage models often encounter difficulties when implemented in finite element codes for fracture prediction. This is because: 1. a real material often has a characteristic length of heterogeneity (e.g., the maximum aggregate size in concrete [21]), but a “local” continuum damage model assumes a material to be homogeneous on any length scales; 2. such a model often produces localized displacement, stress, and strain fields and highly mesh-dependent fracture paths in the presence of strain softening [22]. Therefore,

there is a need for a “nonlocal” continuum damage model capable of producing realistic fracture paths and capturing size effects in real materials.

With a so-call regularization technique, a nonlocal model can be developed based on a “local” model. A regularization technique involves replacing one (or more) locally defined state variable with a corresponding nonlocally regularized state variable. An extensive review of early nonlocal models can be found in Ref. [2]. Recently developed nonlocal models can be classified into two groups, according to their regularization techniques:

1. integral-type—a nonlocal variable is a spatially weighted integral of its corresponding local variable over the neighborhood of a damaged material point [23–29];
2. gradient-enhanced—a nonlocal variable is related to its corresponding local variable via a nonhomogeneous Poisson/Helmholtz equation [30–35].

Gradient-enhanced models are derived from integral-type models. Peerlings et al. [30] expanded a local variable to be regularized into a Taylor series in the neighborhood of a damaged material point, substituted the expression for a nonlocal variable in an integral-type model into this Taylor series, and achieved a Poisson/Helmholtz equation. Integral-type and gradient-enhanced models have their respective advantages and drawbacks. An integral-type model, as a nonlocal model in its original form, is more general because: 1. it imposes no restrictions on the material properties, the characteristic length, or the gradients of the local variable; 2. it only requires the local field to be integrable. However, its integral form makes its implementation in an incremental finite element framework not straightforward. A gradient-enhanced model, as a derivative nonlocal model, is more restrictive because: 1. it requires the material to be isotropic [30]; 2. the characteristic length and the gradients of the local variable must be sufficiently small so that high-order terms in the Taylor series can be omitted; 3. its weak form requires  $C^0$  continuity of the local field. Fortunately, the weak form of a Poisson/Helmholtz equation can be conveniently implemented in

a finite element framework. In this work, focus is placed on integral-type models to seek generality.

Different choices on the local variables to be regularized also lead to different nonlocal models. One option is to regularize the strain tensor or an equivalent strain [28, 30–33, 35]. One motivation of choosing this option is probably to avoid strain localization simply by smoothing the local strain field. In fact, from the thermodynamic point of view, strain localization is a consequence rather than a cause of damage evolution. It is more reasonable to regularize the local variable(s) governing damage evolution. Another motivation is that people often assume the damage factor to be a function of an equivalent strain (see Ref. [30] for example). This assumption, however, contradicts the principle of maximum dissipation. The resulting models therefore do not possess the advantageous features of generalized standard models. Other options include regularizing: 1. the damage factor/tensor [34]; 2. the damage conjugate force (tensor) [23]; 3. both [24–26]. The principle of maximum dissipation suggests that the damage conjugate force is one controlling factor of damage evolution. The latter two options are therefore more favorable. Lorentz and Andrieux [27] recast the nonlocal models by Pijaudier-Cabot and Bažant [23], and Comi and Perego [26] within the framework of generalized standard models and found that: 1. the two recast models were slightly different; 2. the recast model by Comi and Perego [26] was energetically equivalent to its corresponding “local” model, but the other was not. Recall that a “local” model cannot well capture damage and fracture in a real material having a characteristic length [22]. Despite an attractive term, it is questionable whether the above “energetic equivalence” should be satisfied. In fact, the second option has the following advantages over the third option, due to its simplicity: 1. it facilitates the model development; 2. it endows a model with better convergence. Therefore, in this work, the damage conjugate force tensor will be chosen as the local variable to be regularized. Despite advances in integral-type models:

1. most existing models assume damage isotropy, and there is a need for a generalized standard model capable of handling real, complex brittle damage behavior, especially damage anisotropy;
2. although explicit finite element analysis codes are widely used to simulate damage and fracture, there is not a fully explicit integration scheme for integral-type models.

In summary, there is a critical need for overcoming these shortcomings.

In this work, the objective regarding prediction of brittle fracture is to develop a nonlocal continuum damage model. A nonlocal damage conjugate force tensor will be obtained from the “local” one using an integral-type regularization technique. The thermodynamic equations will be formulated in a nonlocally generalized standard manner based on a recently proposed “local” model [36], which can rigorously handle damage anisotropy, tension-compression asymmetry, and damage deactivation. A fully explicit integration scheme for the present model will be developed and then implemented in Abaqus/Explicit via VUMAT. The present model will be validated through: 1. simulating cyclic uniaxial tests on a SiC–SiC woven composite; 2. calibrating its associated material parameters via single edge notched bend (SENB) tests on concrete beams. Its versatility will be demonstrated through simulating a mixed-mode fracture test on a double edge notched (DEN) specimen. The size effects on fracture paths will be investigated. This part of the work (Chapter 2) has been published.<sup>1</sup>

### 1.3 Fatigue damage

Engineering materials often fail by microcrack initiation, propagation, and coalescence when subject to intensive cyclic loading. Despite advances in non-destructive

---

<sup>1</sup>Gao, Zhenyuan, Liang Zhang, and Wenbin Yu, “A nonlocal continuum damage model for brittle fracture,” *Engineering Fracture Mechanics*, vol. 189, pp. 481–500, 2018.

As the author of this Elsevier article, I retain the right to include it in a thesis or dissertation, provided it is not published commercially.

testing, manual testing can be labor-intensive, time-consuming, and error-prone. Fatigue life prediction therefore plays an important role in ensuring structural integrity and reliability. The versatility of a generalized standard continuum damage model also makes it a favorite candidate for modeling fatigue damage. Compared with other fatigue models, they have great potential to achieve a good balance between accuracy and efficiency. In this work, focus is placed on continuum damage models for high-cycle fatigue.

Fatigue damage evolution possesses one unique feature, i.e., its rate depends on the mean stress and the stress amplitude. Simo and Ju [5] first derived a class of viscodamage evolution laws based on the thermodynamics of irreversible processes. Noting that fatigue damage evolution is essentially viscodamage evolution, Fish and coworkers [37, 38] first modeled fatigue damage evolution using these viscodamage evolution laws. Fatigue models calibrated via fatigue tests (e.g., those involving uniaxial, constant amplitude loading) must remain valid in real-world applications (e.g., under multiaxial, spectrum loading). The goal is to seek for anisotropic generalized standard rate-dependent models.

A major branch of existing rate-dependent models derives from the model by Marigo [39]. Such a model involves:

1. formulating a damage criterion for a rate-independent model;
2. determining the so-called brittle damage rate from the consistency condition;
3. setting the fatigue damage rate to be the brittle damage rate times a viscous function.

According to the controlling factors of damage evolution, these models can be classified into (1) strain-controlling [39–42], (2) stress-controlling [43], and (3) damage conjugate force-controlling models [44–47]. However, the dissipation attains its maximum only if the damage conjugate force, neither the stresses nor the strains, is one controlling factor (see Section 3.1 for more details). The three steps also suggest the following:

1. Brittle damage and fatigue damage share some common features.
2. Brittle damage evolution and fatigue damage evolution are linked.

Inspired by this, Mai et al. [42] first calibrated their material parameters irrelevant to the viscous function, via monotonic tests, and then calibrated those in the viscous function, from S–N curves. Despite success, from a thermodynamic perspective, brittle damage evolution and fatigue damage evolution are mostly irrelevant: they have their respective initial damage thresholds and damage accumulation laws (see Section 3.2 for more details), not to mention rate dependence. First, the above assumed fatigue damage rate involves terms resulting from the consistency condition, but a rate-dependent model has no consistency condition. Therefore, the above models cannot be said to be generalized standard. Second, several authors [48, 49] reported both S–N curves and fatigue damage/modulus degradation/maximum strain–cycle curves, which should be sufficient for calibration. These curves, however, have seldom been used for calibration simultaneously. Other rate-dependent models involve relating the fatigue damage increment to the stresses [50–52], attributing fatigue damage evolution to plastic deformation [33, 53], viscoplastic deformation [54], or even entropy production [55], or investigating micromechanisms at the molecular level [56]. Nevertheless, there is still a lack of generalized standard rate-dependent models.

Despite differences, brittle damage and fatigue damage do share some common features. One prominent feature is that, if not evolving, the same amount of damage should identically degrade a material. This led Marigo [39] and other authors to develop their rate-dependent models based on rate-independent models. When developing rate-dependent models, researchers most frequently considered tension–compression asymmetry. When modeling this behavior, some researchers chose strain decomposition [57, 58], and some others chose stress decomposition [14, 59, 60]. In fact, it can be verified that only stress decomposition is valid (see 3.5 for more details). Recently Zhang and Yu [36] developed a rate-independent model capable of handling various brittle damage phenomena based on stress decomposition. A rate-dependent

model developed based on this model will most likely possess the advantages of the rate-independent model.

A further challenge is to derive a closed-form incremental constitutive relation (or to say, an incremental stress–strain relation). Such an incremental relation can be implemented in an explicit finite element analysis code for the fatigue life prediction of engineering structures. One of the few closed-form relations is due to Mai [42], where damage isotropy and strain-controlling damage evolution reduced the complexity of derivation. Two challenges arise when considering damage anisotropy and damage conjugate force-controlling damage evolution:

- Eliminate the damage increment in the incremental relations.
- Properly handle rate-dependent terms in the incremental relations.

Failing to overcome the first challenge often causes an additional computational cost (e.g., 6 more degrees of freedom at each node, due to damage anisotropy). The second challenge can be better understood by considering a similar case in viscoplasticity: to handle rate-dependent terms, several authors [61–64] resorted to the Laplace transform and its inverse but obtained complicated constitutive relations. Due to these challenges, many researchers only developed explicit integration schemes involving solving for the increments in different state variables step by step. Fortunately, Doghri et al. [65] developed an incremental method for elasto-viscoplastic materials, which involves first discretizing the time domain into numerous small intervals and then deriving an incremental constitutive relation over each interval (without the Laplace transform and its inverse), and Zhang and Yu [66] made this method more versatile. One possible solution appears to apply this incremental method to materials undergoing fatigue.

In this work, the objective regarding prediction of continuum fatigue is to develop an anisotropic continuum damage model for high-cycle fatigue. A viscodamage model, which can handle frequently observed brittle damage phenomena, is developed to produce stress-dependent fatigue damage evolution. The governing equation for

damage evolution is derived using an incremental method. A closed-form incremental constitutive relation is derived at last. The present model is validated through model calibration via (1) cyclic compression tests on a concrete, (2) cyclic tensile tests on another concrete, and (3) cyclic tensile tests on a unidirectional IM7/8552 fiber-reinforced composite in its longitudinal and transverse directions, respectively. Different calibration methods are proposed. The feasibility of calibrating a continuum damage model from S–N and modulus degradation/maximum strain–cycle curves are evaluated.

#### 1.4 Interlaminar delamination

Cohesive zone models (CZMs), firstly proposed by Dugdale and Donald [67], and Barenblatt and Isaakovichand [68], can handle interlaminar delamination well without assuming preexisting cracks and small fracture process zones (FPZs). A CZM involves idealizing the FPZ as a separable interface, often ahead of a crack tip, and discretizing this interface into a layer of cohesive elements obeying a cohesive law. A cohesive element can be a line or a surface element with a zero or a nonzero thickness, depending on circumstances [69]. Despite the diversity of cohesive elements, it is a cohesive law that makes a CZM different from others. A cohesive law at least specifies the relation between the interfacial traction and the interfacial separation under various modes of fracture. A monotonic traction–separation curve generally possesses the following features [70]: 1. it often consists an initial increasing portion and a subsequent decreasing/softening portion (see Figure 1.1(a)); 2. when the traction decreases to zero, the element completely fails; 3. for a given separation path, the maximum traction that the element can sustain is referred to as the interfacial strength, and the area underneath the curve equals the critical energy release rate,  $G_c$ . Despite the development of CZMs, researchers are still attempting to make cohesive elements:

1. behave reliably and consistently when deformed along complex (e.g., nonproportional, unloading–reloading) separation paths;

2. display experimental critical energy release rate–mode mixture ratio relationships ( $G_c$ – $G_{II}/G$  relationships), which vary from case to case and can be somewhat complex (see Ref. [71] for examples).

Nonproportional, unloading–reloading separation paths are always more realistic than proportional, monotonic ones. Turon and his coworkers [72,73] observed that, even in a finite element model of a mixed-mode bending (MMB) specimen, cohesive elements were often deformed along nonproportional separation paths. During the development of CZM in this work, focus is placed on achieving these two goals.

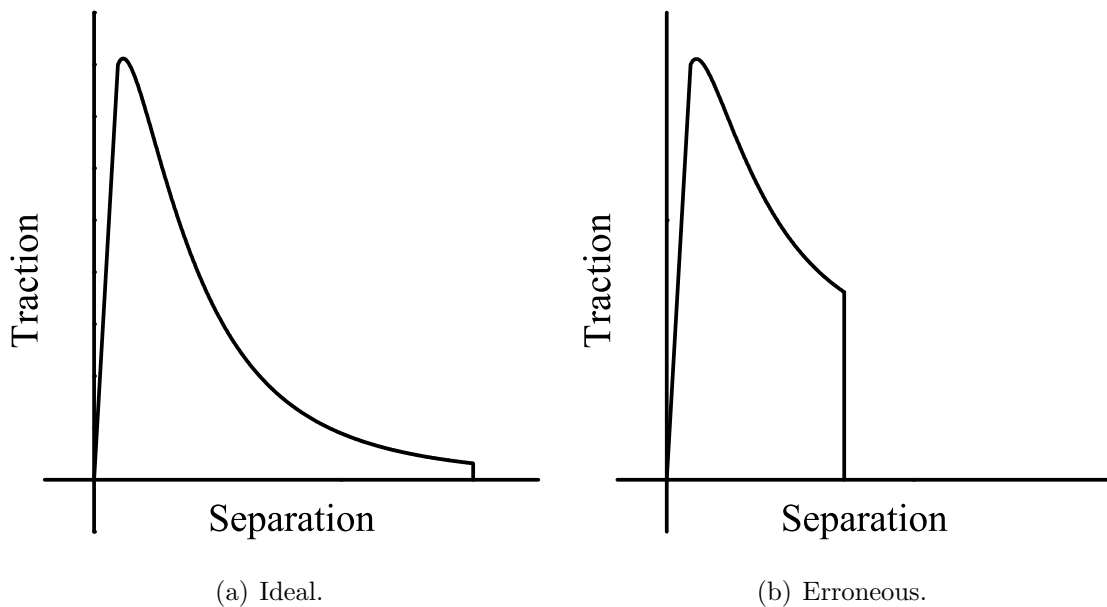


Fig. 1.1. Typical traction–separation relationships in CZMs.

Recently developed CZMs for interlaminar delamination can be classified into potential-based CZMs and damage-type CZMs. A potential-based CZM involves: 1. assuming the existence of a potential function capable of specifying the pointwise traction–separation relation; 2. properly formulating the potential function such that the associated cohesive elements exhibit designated behavior. A detailed review of potential-based CZMs can be found in Ref. [74]. In this work, focus is placed on

damage-type CZMs. A cohesive element and a damageable material actually share many common features:

1. both of them exhibit damage-type behavior (e.g., degradation and softening) and are often deformed along complex separation/loading paths;
2. delamination and damage are essentially irreversible processes that can be described by thermodynamics.

Researchers developed various damage-type CZMs, and some of them referred to generalized standard continuum damage models. Despite the aforementioned advantages, one must face a dilemma when developing a generalized standard CZM. Specifically, one can choose either a scalar-valued damage factor or a damage vector as the measure of the degradation of a cohesive element. On one hand, a damage factor leads to an element always identically degraded in all directions. In a generalized standard CZM, its associated scalar-valued damage conjugate force prevents a cohesive element from exhibiting sophisticated mixed-mode behavior, due to its simplicity. On the other hand, a damage vector leads to an element that can be differently degraded in different directions. It is expected that such an element fails when the projection of the damage vector onto a certain direction is close to unity, or to say, when the element cannot even sustain a small traction in a certain direction (see Figure 1.1(a)). Numerical experiments indicate that, in a finite element model of an MMB specimen, such an element, associated with a generalized standard CZM, often fails when the resultant traction is not so small (see Figure 1.1(b)). At the structural level, this causes a predicted load–displacement curve to have a sudden drop right after delamination initiation, indicating that progressive delamination is highly unstable. This kind of predicted load–displacement curves, however, contradict experimental data (e.g., those in Ref. [75]). This dilemma makes generalized standard CZMs less popular than non-generalized standard CZMs.

A non-generalized standard CZM imposes few restrictions on the damage function and allows a non-associated flow rule. Allix and his coworkers [76–78] first developed

a class of damage-type CZMs within the framework of thermodynamics. Such a typical non-generalized standard CZMs involves: 1. choosing a damage vector and also a damage function being a function of the damage conjugate force vector; 2. assuming a non-associated flow rule forcing all components of the damage vector to approach unity simultaneously at the onset of failure. Borg and his coworkers [79, 80] developed similar CZMs except that they assumed a damage function being a function of the traction vector. Camanho et al. [69] developed a bilinear damage-type CZM and achieved good agreement between their predictions and the experimental data in Ref. [75]. Turon et al. [81, 82] developed a damage model similar to a generalized standard one except that, in its damage function and damage evolution laws, an effective separation took the place of a damage conjugate force. Overgaard et al. [83] further applied the principle of maximum dissipation to its damage function and obtained the same damage evolution laws. Despite improvements, it is rare that a GSM has a flow rule directly related to an effective separation rather than a damage conjugate force. Mosler and Scheider [84] developed another class of damage-type CZMs involving: 1. assuming a damage factor being a function of the damage conjugate force, which is also the state variable describing damage accumulation (this allows a user to customize the traction–separation relation); 2. requiring each cohesive element to obey the so-called principle of minimum stress power. Despite improvements, these CZMs are not generalized standard because: 1. in thermodynamics, it is rare that a thermodynamic driving force is also a state variable; 2. the principle of minimum stress power is not equivalent to the principle of maximum dissipation (see Ref. [8] for more details). Therefore, there is still a need for a versatile generalized standard CZM developed in a thermodynamically rigorous manner.

In this work, the objective regarding prediction of interlaminar delamination is to develop a string-type CZM. Focus is placed on making the cohesive elements associated with the present CZM: 1. behave reliably and consistently when deformed along complex separation paths; 2. capable of displaying experimental critical energy release rate–mode mixture ratio relationships. To achieve the first goal, the thermo-

dynamic equations will be formulated in a generalized standard manner. To resolve the aforementioned dilemma, each cohesive element will be idealized as a deformable string exhibiting path dependent damage behavior. To achieve the second goal, a damage model having a path dependence function will be developed, and the path dependence function will be constructed such that each cohesive element can exhibit designated, possibly sophisticated mixed-mode behavior. The rate form of the cohesive law can be subsequently derived. The interface parameters associated with the present CZM will be calibrated from experimental data. The present CZM will then be validated through simulating a series of flexural tests using Abaqus/Explicit. The effect of the interfacial strength on a load–displacement curves will also be evaluated. This part of the work (Chapter 4) has been published.<sup>2</sup>

## 1.5 Fatigue delamination

Long-term cyclic load is one of the most prevalent service load in engineering structures, which is also another common cause for fatigue delamination. Manual fatigue life testing for composite delamination can be time-consuming and expensive, due to the large number of cycles required for each test, and different factors that can affect interlaminar fatigue behavior (e.g., mode mixture ratio, cyclic load profile, and material configuration). It is desirable to develop a rigorous numerical model for interlaminar fatigue that accounts for these factors and can be easily implemented in complex structural analysis.

To extend the quasi-static CZMs for interlaminar fatigue, De-Andrés et al. [85] first decoupled the damage parameter into one part due to quasi-static loading and another part due to cyclic loading, where the damage rate was directly formulated as increment per cycle. Several authors implemented Paris’ law [86–89] or other power law like [90,91] empirical relations into cyclic damage rate formulation. Such models usually

---

<sup>2</sup>Zhang, Liang, Zhenyuan Gao, and Wenbin Yu, “A string-based cohesive zone model for interlaminar delamination,” *Engineering Fracture Mechanics*, vol. 180, pp. 1–22, 2017.

As the author of this Elsevier article, I retain the right to include it in a thesis or dissertation, provided it is not published commercially.

only depend on the computation of energy release rates or stress intensity factors, without an intrinsic implementation of rate-dependency. Consequently, additional parameters and assumptions are required for each load-related factor (e.g., mode mixture ratio, load ratio, and fatigue limit). To include effects of different loading profiles, Yang et al. [92] and Nguyen et al. [93] developed CZMs that defined different stiffness degradation rates for loading and unloading, which were nonlinear functions of separation rate. With the same idea, several authors [94–96] developed CZMs that formulated mixed-mode damage evolution laws as different functions of separation rate for loading and unloading. With this approach, effects of rate-dependent cyclic loading are explicitly described in the traction separation law. Thus, interlaminar fatigue behavior can be numerically reproduced in a cycle by cycle manner.

To avoid the possible arbitrariness in formulating the traction separation law, another approach to formulate rate-dependency is to include viscous effect in the CZM formulation following unified thermodynamic principles. Corigliano and Ricci [97] first presented both a softening viscoplastic CZM and a viscodamage CZM for generalized standard materials to capture rate-dependent delamination. Both double cantilever beam (DCB) and end-notched flexure (ENF) tests are simulated in monotonic loading conditions with success. The goal now is to apply a similar CZM to cyclic loading conditions. On the one hand, viscoplastic CZM is not suitable for high-cycle fatigue in a physical sense because:

- For fiber-matrix interfacial debonding, the fracture can be considered brittle under high-cycle dynamic loads.
- Crack formation and propagation during delamination is essentially damage mechanics instead of plasticity.

On the other hand, the viscodamage CZM in Ref. [97] considers the viscous effects in mode I, II and III as independent. This assumption is not suitable for complex separation paths, as the crazing and fibril formation ahead of crack tips (observed by Kramer and Berger [98,99] for polymer interfaces) cannot be described. Musto and

Alfano [100, 101] and Parrinello et al. [102] presented thermodynamically consistent viscodamage CZMs with unified scalar damage parameter and viscosity function, and showed that a rate-independent mixed-mode fracture energy can be obtained. Because these CZMs are not designed to predict fatigue life, the so-called consistency condition is applied to regularize the damage surface during damage evolution. This makes them unable to capture rate-dependent behavior during unloading and reloading. Therefore, there is still a lack of generalized standard viscodamage CZM for interlaminar fatigue.

In this work, the objective regarding interlaminar fatigue is to extend the previously developed string-based CZM to produce rate-dependent damage evolution. A viscodamage model, capable of handling brittle damage behavior, will be developed to produce realistic interlaminar crack propagation under high-cycle fatigue. An implicit integration scheme, which can handle complex separation paths and mixed-mode delamination, is developed and implemented in Abaqus/Standard via UMAT. The material properties associated with the present model are first selected and calibrated from double cantilever beam (DCB) fatigue tests. The present model is then validated through producing G–N and crack growth rate curves for both DCB and end-notched flexure (ENF) tests. Finally, its capability to handle mixed-mode fatigue delamination is demonstrated through simulating a series of mixed-mode bending (MMB) tests.

## 2. NONLOCAL DAMAGE MODEL

### 2.1 Thermodynamics and energy equivalence

This chapter uses the same notation system as that in Chapter 3, and different from those in Chapter 4 and 5. Let  $\psi$  denote the Helmholtz free energy per unit mass of a material. It can be treated as a function of a suitable set of independent state variables describing the elasticity and damage of the material, e.g.,

$$\psi = \psi(\boldsymbol{\epsilon}, \mathbf{d}, \beta), \quad (2.1)$$

where  $\boldsymbol{\epsilon}$  denotes the elastic strain tensor,  $\mathbf{d}$  is a symmetric second-order tensor measuring damages, namely the second-order damage tensor, and  $\beta$  is a scalar describing damage accumulation. Following Ref. [20], assume that  $\psi$  can be decomposed into its elastic and damage accumulation parts, i.e.,

$$\psi(\boldsymbol{\epsilon}, \mathbf{d}, \beta) = \psi_e(\boldsymbol{\epsilon}, \mathbf{d}) + \psi_d(\beta). \quad (2.2)$$

The thermodynamic driving forces conjugate to the state variables in Eq. (2.2) are defined as

$$\boldsymbol{\sigma} = \rho \frac{\partial \psi}{\partial \boldsymbol{\epsilon}} = \rho \frac{\partial \psi_e}{\partial \boldsymbol{\epsilon}}, \quad \mathbf{y} = -\rho \frac{\partial \psi}{\partial \mathbf{d}} = -\rho \frac{\partial \psi_e}{\partial \mathbf{d}}, \quad B = \rho \frac{\partial \psi}{\partial \beta} = \rho \frac{d\psi_d}{d\beta}, \quad (2.3)$$

where  $\boldsymbol{\sigma}$  denotes the stress tensor,  $\mathbf{y}$  denotes the damage conjugate force tensor, and  $B$  denotes the damage accumulation conjugate force.

For isothermal deformation, the Clausius–Duhem inequality can be written as

$$\Phi = \boldsymbol{\sigma} : \dot{\boldsymbol{\epsilon}} - \rho \dot{\psi} \geq 0, \quad (2.4)$$

where  $\Phi$  denotes the dissipation per unit volume, and the overdot denotes the time derivative of a quantity. Combining Eqs. (2.2)–(2.4) gives

$$\Phi = \mathbf{y} : \dot{\mathbf{d}} - B \dot{\beta} \geq 0. \quad (2.5)$$

Let  $\Omega$  denote the domain occupied by the material (with boundary  $\partial\Omega$ ), and let  $\langle \cdot \rangle = \int_{\Omega} (\cdot) dV$  denote the volume integral of a quantity over  $\Omega$ . Define nonlocal damage conjugate force tensor  $\bar{\mathbf{y}}$  as

$$\bar{\mathbf{y}} = \int_{\Omega} \bar{w}(\mathbf{x} - \boldsymbol{\xi}) \mathbf{y}(\boldsymbol{\xi}) d\boldsymbol{\xi}, \quad (2.6)$$

where  $\bar{w} = w/\langle w \rangle$  is a normalized weight function with

$$w(\mathbf{x}) = \exp\left(-\frac{\|\mathbf{x}\|^2}{l_c^2}\right) \quad (2.7)$$

and  $l_c$  being the characteristic length of heterogeneity [103], where  $\|\mathbf{x}\|$  denotes the distance of material point  $x$  from a designated origin within  $\Omega$ . Also define nonlocal damage dissipation as

$$\bar{\Phi} = \bar{\mathbf{y}} : \dot{\mathbf{d}} - B\dot{\beta}. \quad (2.8)$$

Let  $f$  denote the nonlocal damage function. Following Ref. [7], assume that the following principle of maximum nonlocal dissipation applies throughout this paper: for fixed but otherwise arbitrary  $\dot{\mathbf{d}}$  and  $\dot{\beta}$ , the actual  $\bar{\mathbf{y}}$  and  $B$  should maximize  $\bar{\Phi}$  subject to constraint  $f \leq 0$ , or mathematically speaking, should make Lagrange functional

$$L(\bar{\mathbf{y}}, B, \dot{\lambda}; \dot{\mathbf{d}}, \dot{\beta}) = \bar{\mathbf{y}} : \dot{\mathbf{d}} - B\dot{\beta} - \dot{\lambda}f \quad (2.9)$$

attain its extremum, where  $\dot{\lambda}$  is a positive Lagrange multiplier. This is the equivalent of solving associated damage evolution laws

$$\dot{\mathbf{d}} = \dot{\lambda} \frac{\partial f}{\partial \bar{\mathbf{y}}} \quad \text{and} \quad \dot{\beta} = -\dot{\lambda} \frac{\partial f}{\partial B} \quad (2.10)$$

subject to Kuhn–Tucker conditions, or loading/unloading conditions,

$$f \leq 0, \quad \dot{\lambda} \geq 0, \quad \dot{\lambda}f = 0, \quad (2.11)$$

which physically mean that damage evolution is irreversible. Eq. (2.10) implies that  $f$  must be a function of  $\bar{\mathbf{y}}$  and  $B$ .

The effective space is where a fictitious, undamaged material is obtained from a real, damaged one by removing all damage so that a set of so-called effective quantities

can be defined to facilitate the derivation. The energy equivalence hypothesis [104] specifies the correspondence between effective quantities and quantities measurable in the real space, namely apparent quantities. It follows the definition of the effective stress tensor: the effective stress tensor should be applied to an undamaged material element such that it produces the same elastic Helmholtz free energy as that observed on a damaged material element subject to the apparent stress tensor [20], i.e.,

$$\rho\psi_e = \frac{1}{2}\boldsymbol{\epsilon} : \boldsymbol{\mathcal{C}} : \boldsymbol{\epsilon} = \frac{1}{2}\tilde{\boldsymbol{\epsilon}} : \tilde{\boldsymbol{\mathcal{C}}} : \tilde{\boldsymbol{\epsilon}}, \quad (2.12)$$

where  $\boldsymbol{\mathcal{C}}$  denotes the apparent elasticity tensor, and the overtilde denotes an effective quantity (e.g.,  $\tilde{\boldsymbol{\mathcal{C}}}$  denotes the effective or the initial elasticity tensor, which remains constant during continued deformation). Following Ref. [105], let  $\tilde{\boldsymbol{\sigma}}$  be related to  $\boldsymbol{\sigma}$  by

$$\tilde{\boldsymbol{\sigma}} = \boldsymbol{\mathcal{M}} : \boldsymbol{\sigma} \quad \text{or} \quad \boldsymbol{\sigma} = \boldsymbol{\mathcal{M}}^{-1} : \tilde{\boldsymbol{\sigma}}, \quad (2.13)$$

where  $\boldsymbol{\mathcal{M}}$  denotes the fourth-order damage effect tensor. Following Ref. [36], let

$$\boldsymbol{\mathcal{D}} = \sum_{i=1}^3 \sum_{j=1}^3 d_{ij} \mathbf{e}_i \otimes \mathbf{e}_j \otimes \mathbf{e}_i \otimes \mathbf{e}_j \quad (2.14)$$

denote a fourth-order diagonal damage tensor, where  $\mathbf{e}_i$  denotes the unit vector. Let  $\boldsymbol{\mathcal{M}}^{-1}$  be related to  $\boldsymbol{\mathcal{D}}$  by

$$\boldsymbol{\mathcal{M}}^{-1} = \boldsymbol{\mathcal{I}} - \boldsymbol{\mathcal{D}}, \quad (2.15)$$

where  $\boldsymbol{\mathcal{I}}$  denotes the fourth-order identity tensor. Hooke's law can be written as

$$\boldsymbol{\sigma} = \boldsymbol{\mathcal{C}} : \boldsymbol{\epsilon} \quad \text{and} \quad \tilde{\boldsymbol{\sigma}} = \tilde{\boldsymbol{\mathcal{C}}} : \tilde{\boldsymbol{\epsilon}} \quad (2.16)$$

in the apparent and the effective spaces, respectively. Combining Eqs. (2.12), (2.13), and (2.16) gives

$$\tilde{\boldsymbol{\epsilon}} = \boldsymbol{\mathcal{M}}^{-1} : \boldsymbol{\epsilon} \quad \text{or} \quad \boldsymbol{\epsilon} = \boldsymbol{\mathcal{M}} : \tilde{\boldsymbol{\epsilon}}. \quad (2.17)$$

Substituting Eq. (2.17) into Eq. (2.12) gives

$$\boldsymbol{\mathcal{C}} = \boldsymbol{\mathcal{M}}^{-1} : \tilde{\boldsymbol{\mathcal{C}}} : \boldsymbol{\mathcal{M}}^{-1}. \quad (2.18)$$

## 2.2 Nonlocal damage model

In this section, a nonlocal damage model will be developed based on the “local” model in Ref. [36] so that it can rigorously handle damage anisotropy, tension-compression asymmetry, and damage deactivation. One major difference between these two models is that here  $\bar{\mathbf{y}}$  rather than  $\mathbf{y}$  is one controlling factor of damage evolution. More details on some derivation in this section can be found in Ref. [36].

Suppose that the material exhibits damage anisotropy, tension-compression asymmetry, and damage deactivation. It is beneficial to first specify all damage parameters to be calibrated via a series of tension/compression and pure shear tests. Assume that the material obeys damage criterion

$$f^\pm(\bar{\mathbf{y}}, B^\pm) = (1 - \chi) \|\bar{\mathbf{y}}\|_{\mathcal{J}^\pm} + \chi \mathbf{j}^\pm : \bar{\mathbf{y}} - k^\pm - B^\pm \leq 0 \quad (2.19)$$

in entire tension/compression, where the superscript  $+/-$  denotes a parameter measured via tension/compression tests unless otherwise specified,

$$\|\bar{\mathbf{y}}\|_{\mathcal{J}^\pm} = \sqrt{\bar{\mathbf{y}} : \mathcal{J}^\pm : \bar{\mathbf{y}}} \quad (2.20)$$

with  $\mathcal{J}^\pm$  being a fourth-order tensor describing damage anisotropy,  $k^\pm$  denotes the initial damage threshold,  $0 \leq \chi \leq 1$  denotes a parameter describing the curvature of the damage surface, and  $\mathbf{j}^\pm$  is a second-order tensor also describing damage anisotropy. Let  $\mathcal{J}^\pm$  be related to  $\mathbf{j}^\pm$  by

$$\mathcal{J}_{iii}^\pm = (j_{ii}^\pm)^2 \quad \text{and} \quad \mathcal{J}_{ijij}^\pm = 2(j_{ij}^\pm)^2 \quad (i \neq j, \text{ and no summation over } i \text{ or } j) \quad (2.21)$$

(the other components of  $\mathcal{J}^\pm$  vanish), and set  $j_{11}^\pm = 1$  and  $\mathcal{J}_{1111}^\pm = 1$ . Eqs. (2.2) and (2.3) imply that  $B$  is a function of  $\beta$ , i.e.,  $B = B(\beta)$ , which is referred to as the damage accumulation law, whose form varies from case to case. Assume that the damage accumulation law takes the form of  $B^\pm = B^\pm(\beta)$  in entire tension/compression, whose specific form is to be determined. It can be verified that, if  $\boldsymbol{\epsilon}$  and  $\mathbf{d}$  are uniformly distributed over  $\Omega$ , so does  $\mathbf{y}$  (see Eq. (2.54) for more details). In Eq. (2.6), setting  $\mathbf{y}$  to be constant in  $\Omega$  gives  $\bar{\mathbf{y}} = \mathbf{y}$  everywhere. In this case, there is no numerical

difference between a nonlocal model and a “local” one. This implies that the above damage parameters can be calibrated via tension/compression and pure shear tests, similarly to Ref. [36].

The basic idea of modeling tension/compression asymmetry is to treat tensile and compressive stresses as another cause of damage anisotropy, just like texture patterns and external loads, and to treat tension/compression asymmetry as another consequence of damage anisotropy. With this idea, one can properly define the parameters describing damage anisotropy to produce tension/compression asymmetry. Specifically,  $\tilde{\boldsymbol{\sigma}}$  can be expressed as

$$\tilde{\boldsymbol{\sigma}} = \sum_{i=1}^3 \tilde{\sigma}_i \mathbf{p}_i \otimes \mathbf{p}_i, \quad (2.22)$$

where  $\mathbf{p}_i$  denotes its  $i$ th principal unit vector, and  $\tilde{\sigma}_i = \mathbf{p}_i \cdot \tilde{\boldsymbol{\sigma}} \cdot \mathbf{p}_i$  denotes its  $i$ th eigenvalue. Following Ref. [14], define two fourth-order projection tensors

$$\mathcal{P}^- = \sum_{i=1}^3 \tilde{H}(-\tilde{\sigma}_i) \mathbf{p}_i \otimes \mathbf{p}_i \otimes \mathbf{p}_i \otimes \mathbf{p}_i \quad \text{and} \quad \mathcal{P}^+ = \mathbf{I} - \mathcal{P}^- \quad (2.23)$$

so that  $\mathcal{P}^\pm$  can project a second-order tensor onto the tensile/compressive part of  $\tilde{\boldsymbol{\sigma}}$ , say  $\tilde{\boldsymbol{\sigma}}^\pm$ , i.e.,

$$\tilde{\boldsymbol{\sigma}}^\pm = \mathcal{P}^\pm : \tilde{\boldsymbol{\sigma}}, \quad (2.24)$$

where

$$\tilde{H}(\tilde{\sigma}_i) = \begin{cases} 0 & \tilde{\sigma}_i < 0, \\ H(\tilde{\sigma}_m) & \tilde{\sigma}_i = 0, \\ 1 & \tilde{\sigma}_i > 0 \end{cases} \quad \text{with} \quad H(x) = \begin{cases} 0 & x < 0, \\ 1 & x \geq 0. \end{cases} \quad (2.25)$$

In Eq. (2.25),  $H(x)$  is the Heaviside step function, and  $\tilde{\sigma}_m$  denotes the mean effective stress.  $\tilde{H}(\tilde{\sigma}_i)$  is so defined that damages are entirely tensile/compressive in uniaxial/biaxial tension/compression. Let  $\zeta = k^+/k^-$  be a parameter describing the contrast between tensile and compressive damage behavior. Assume that the material obeys damage criterion

$$f(\bar{\mathbf{y}}, B) = \bar{\mathbf{y}}_{eq} - k - B \leq 0 \quad (2.26)$$

regardless of loading, where

$$\bar{\mathbf{y}}_{eq} = (1 - \chi) \sqrt{\bar{\mathbf{y}} : \mathcal{J} : \bar{\mathbf{y}}} + \chi \mathbf{j} : \bar{\mathbf{y}} \equiv (1 - \chi) \|\bar{\mathbf{y}}\|_{\mathcal{J}} + \chi \mathbf{j} : \bar{\mathbf{y}}, \quad (2.27)$$

$$\mathbf{j} = \mathcal{P}^+ : \mathbf{j}^+ + \zeta \mathcal{P}^- : \mathbf{j}^-, \quad \mathcal{J} = \mathcal{P}^+ : \mathcal{J}^+ : \mathcal{P}^+ + \zeta^2 \mathcal{P}^- : \mathcal{J}^- : \mathcal{P}^-, \quad (2.28)$$

$$k = k^+ = \zeta k^-, \quad B = B^+ = \zeta B^-, \quad (2.29)$$

so that Eq. (2.26) is equivalent to Eq. (2.19) in entire tension/compression.

Substituting Eq. (2.26) into Eq. (2.10) gives

$$\dot{\mathbf{d}} = \dot{\lambda} \mathbf{n} \quad \text{and} \quad \dot{\beta} = \dot{\lambda}, \quad (2.30)$$

where  $\mathbf{n} = \partial f / \partial \bar{\mathbf{y}} = \partial \bar{y}_{eq} / \partial \bar{\mathbf{y}}$  denotes the normal to the damage surface. Taking time derivatives on both sides of Eq. (2.26) gives the consistency condition as

$$\dot{f} = \dot{y}_{eq} - \frac{dB}{d\beta} \dot{\beta} = 0, \quad (2.31)$$

from which the governing equations of damage evolution can be derived. It is beneficial to find the relationship between  $\dot{\mathcal{P}}^-$  and  $\dot{\check{\boldsymbol{\epsilon}}}$ . According to Ref. [106], if  $\check{\boldsymbol{\sigma}}$  has three distinct eigenvalues,  $\dot{\mathbf{p}}_i$  can be related to  $\dot{\check{\boldsymbol{\sigma}}}$  by

$$\begin{aligned} \dot{\mathbf{p}}_i &= \left( \sum_{j=1; j \neq i}^3 \frac{\mathbf{p}_j \otimes \mathbf{p}_j \otimes \mathbf{p}_i}{\tilde{\sigma}_i - \tilde{\sigma}_j} \right) : \dot{\check{\boldsymbol{\sigma}}} \\ &= \frac{1}{2} \left[ \sum_{j=1; j \neq i}^3 \frac{\mathbf{p}_j \otimes (\mathbf{p}_j \otimes \mathbf{p}_i + \mathbf{p}_i \otimes \mathbf{p}_j)}{\tilde{\sigma}_i - \tilde{\sigma}_j} \right] : \dot{\check{\boldsymbol{\sigma}}} \equiv \mathcal{B}_i : \dot{\check{\boldsymbol{\sigma}}}, \end{aligned} \quad (2.32)$$

where the second equality holds because  $\dot{\check{\boldsymbol{\sigma}}}$  is symmetric.  $\mathcal{B}_i$  actually relates the rotation of the principal stress axes to  $\dot{\check{\boldsymbol{\sigma}}}$ . If  $\check{\boldsymbol{\sigma}}$  does not have three distinct eigenvalues,  $\mathcal{B}_i$  can be numerically determined. Taking time derivatives on both sides of the first equation of Eq. (2.23) gives

$$\begin{aligned} \dot{\mathcal{P}}_{mnpq}^- &= \sum_{i=1}^3 \tilde{H}(-\tilde{\sigma}_i) \left[ (\dot{p}_i)_m (p_i)_n (p_i)_p (p_i)_q + (p_i)_m (\dot{p}_i)_n (p_i)_p (p_i)_q \right. \\ &\quad \left. + (p_i)_m (p_i)_n (\dot{p}_i)_p (p_i)_q + (p_i)_m (p_i)_n (p_i)_p (\dot{p}_i)_q \right]. \end{aligned} \quad (2.33)$$

Eq. (2.32) can be further expressed as

$$(\dot{p}_i)_j = (\mathcal{B}_i)_{jrs} \dot{\check{\sigma}}_{rs} = (\mathcal{B}_i)_{jrs} \tilde{\mathcal{C}}_{rskl} \dot{\check{\epsilon}}_{kl}. \quad (2.34)$$

Substituting Eq. (2.34) into Eq. (2.33) gives

$$\begin{aligned} \dot{\mathcal{P}}_{mnpq}^- = & \left\{ \sum_{i=1}^3 \tilde{H}(-\tilde{\sigma}_i) \left[ (\mathcal{B}_i)_{mrs} (p_i)_n (p_i)_p (p_i)_q + (p_i)_m (\mathcal{B}_i)_{nrs} (p_i)_p (p_i)_q \right. \right. \\ & \left. \left. + (p_i)_m (p_i)_n (\mathcal{B}_i)_{prs} (p_i)_q + (p_i)_m (p_i)_n (p_i)_p (\mathcal{B}_i)_{qrs} \right] \right\} \tilde{\mathcal{C}}_{rskl} \dot{\epsilon}_{kl} \equiv \mathcal{Q}_{mnklpq}^- \dot{\epsilon}_{kl}. \end{aligned} \quad (2.35)$$

$\dot{\bar{y}}_{eq}$  can be obtained through some derivation as

$$\dot{\bar{y}}_{eq} = \mathbf{n} : \dot{\bar{\mathbf{y}}} - \boldsymbol{\kappa} : \dot{\bar{\boldsymbol{\epsilon}}}, \quad (2.36)$$

where

$$\begin{aligned} \mathbf{n} = & (1 - \chi) \frac{\mathcal{J} : \bar{\mathbf{y}}}{\|\bar{\mathbf{y}}\|_{\mathcal{J}}} + \chi \mathbf{j}, \quad (2.37) \\ \kappa_{ij} = & \frac{1 - \chi}{2\|\bar{\mathbf{y}}\|_{\mathcal{J}}} \bar{y}_{kl} \left[ \mathcal{Q}_{kljppq}^- (\mathcal{J}_{pqrs}^+ \mathcal{P}_{rsmn}^+ - \zeta^2 \mathcal{J}_{pqrs}^- \mathcal{P}_{rsmn}^-) \right. \\ & \left. + (\mathcal{P}_{klpq}^+ \mathcal{J}_{pqrs}^+ - \zeta^2 \mathcal{P}_{klpq}^- \mathcal{J}_{pqrs}^-) \mathcal{Q}_{rsijmn}^- \bar{y}_{mn} + \chi \bar{y}_{kl} \mathcal{Q}_{kljijmn}^- (j_{mn}^+ - \zeta j_{mn}^-) \right]. \end{aligned} \quad (2.37')$$

More details on the derivation of Eqs. (2.32)–(2.37) can be found in Ref. [36]. Substituting Eq. (2.36) into Eq. (2.31) and rearranging the equation give

$$\dot{\beta} = \dot{\lambda} = \frac{\mathbf{n} : \dot{\bar{\mathbf{y}}} - \boldsymbol{\kappa} : \dot{\bar{\boldsymbol{\epsilon}}}}{\frac{dB}{d\beta}}. \quad (2.38)$$

Substituting Eq. (2.38) into the first equation of Eq. (2.30) gives

$$\dot{\mathbf{d}} = \frac{\mathbf{n} : \dot{\bar{\mathbf{y}}} - \boldsymbol{\kappa} : \dot{\bar{\boldsymbol{\epsilon}}}}{\frac{dB}{d\beta}} \mathbf{n} = \frac{\mathbf{n} \otimes \mathbf{n}}{\frac{dB}{d\beta}} : \dot{\bar{\mathbf{y}}} - \frac{\mathbf{n} \otimes \boldsymbol{\kappa}}{\frac{dB}{d\beta}} : \dot{\bar{\boldsymbol{\epsilon}}} \equiv \mathcal{S} : \dot{\bar{\mathbf{y}}} - \mathcal{R} : \dot{\bar{\boldsymbol{\epsilon}}}, \quad (2.39)$$

which is the governing equation of damage evolution.  $-\boldsymbol{\kappa} : \dot{\bar{\boldsymbol{\epsilon}}}$  in Eq. (2.38) (or  $-\mathcal{R} : \dot{\bar{\boldsymbol{\epsilon}}}$  in Eq. (2.39)) can be nonzero when the principal stress axes rotate in combined tension–compression.  $\boldsymbol{\kappa} : \dot{\bar{\boldsymbol{\epsilon}}}$  can be so large that it makes  $\dot{\lambda}$  negative. In this case, loading/unloading conditions Eq. (2.11) is not satisfied, and damages neither initiate nor evolve.

The key point of modeling damage deactivation is to distinguish between tensile and compressive damages. Substituting Eq. (2.28) into Eq. (2.37) gives

$$\begin{aligned} \mathbf{n} = & \left[ (1 - \chi) \frac{\mathcal{P}^+ : \mathcal{J}^+ : \mathcal{P}^+ : \bar{\mathbf{y}}}{\|\bar{\mathbf{y}}\|_{\mathcal{J}}} + \chi \mathcal{P}^+ : \mathbf{j}^+ \right] \\ & + \left[ (1 - \chi) \frac{\zeta^2 \mathcal{P}^- : \mathcal{J}^- : \mathcal{P}^- : \bar{\mathbf{y}}}{\|\bar{\mathbf{y}}\|_{\mathcal{J}}} + \chi \zeta \mathcal{P}^- : \mathbf{j}^- \right] \equiv \mathbf{n}^+ + \mathbf{n}^-, \end{aligned} \quad (2.40)$$

where  $\mathbf{n}^\pm$  denotes the projection of  $\mathbf{n}$  onto  $\boldsymbol{\sigma}^\pm$ . Substituting Eq. (2.40) into Eq. (2.30) gives

$$\dot{\mathbf{d}} = \dot{\lambda} \mathbf{n}^+ + \dot{\lambda} \mathbf{n}^- \equiv \dot{\mathbf{d}}^+ + \dot{\mathbf{d}}^-, \quad (2.41)$$

where  $\dot{\mathbf{d}}^+$  and  $\dot{\mathbf{d}}^-$  denote the tensile and compressive parts of  $\dot{\mathbf{d}}$ , respectively. The tensile and compressive parts of  $\mathbf{d}$  can then be obtained as

$$\mathbf{d}^+ = \int_0^t \dot{\mathbf{d}}^+ dt \quad \text{and} \quad \mathbf{d}^- = \mathbf{d} - \mathbf{d}^+, \quad (2.42)$$

respectively. In the presence of damage deactivation, state function  $\psi_e$  (see Eq. (2.2)) should be an explicit function of a measure of active damages rather than that of  $\mathbf{d}$ , a measure of active and inactive damages, and so should  $\mathcal{D}$ . Following Ref. [107], we assume that: 1. a constant portion of tensile damages are inactive in compression; 2. all compressive damages are active all the time. Let  $\eta \mathbf{d}^+$  denote the portion of  $\mathbf{d}^+$  remaining active in compression so that

$$\mathbf{d}^* (\mathbf{d}, \mathbf{d}^+) = \mathbf{d} - (1 - \eta) \mathcal{P}^- : \mathbf{d}^+, \quad (2.43)$$

namely the nominal second-order damage tensor, measures active damages. Eqs. (2.2), (2.3), and (2.14) can then be amended as

$$\psi_e = \psi_e (\boldsymbol{\epsilon}, \mathbf{d}^*), \quad \boldsymbol{\sigma} = \rho \left( \frac{\partial \psi_e}{\partial \boldsymbol{\epsilon}} \right)_{\mathbf{d}^*}, \quad \mathbf{y} = -\rho \left( \frac{\partial \psi_e}{\partial \mathbf{d}^*} \right)_{\boldsymbol{\epsilon}}, \quad (2.44)$$

$$\mathcal{D} = \sum_{i=1}^3 \sum_{j=1}^3 d_{ij}^* \mathbf{e}_i \otimes \mathbf{e}_j \otimes \mathbf{e}_i \otimes \mathbf{e}_j, \quad (2.45)$$

respectively. In fact, in Eqs. (2.43)–(2.45),  $\mathbf{d}^*$  serves as a pseudo-state variable, and  $\mathbf{d}$  a variable of  $\mathbf{d}^*$ .

### 2.3 Explicit integration scheme

The finite element implementation of a nonlocal model has been extensively studied (see Refs. [30], [25], [33], and [35] for examples). Nowadays a nonlocal model can be implemented in commercial finite element code Abaqus/Explicit via user subroutine VUMAT, for structural analysis, where:

1. Abaqus/Explicit can be used to solve complicated quasi-static problems;
2. VUMAT is used to define the constitutive behavior of a material [108].

Let  $(\cdot)_n$  denote a quantity at a given instant of time,  $t_n$ . When calling VUMAT at an integration point, Abaqus/Explicit passes in  $\boldsymbol{\sigma}_n$  and  $\Delta\boldsymbol{\epsilon}$  and gets back  $\boldsymbol{\sigma}_{n+1}$ , where  $\Delta(\cdot)$  denotes the increment in a quantity over time interval  $[t_n, t_{n+1}]$ . Note that, for a state variable, its increment can be related to its rate using the Euler method (e.g,  $\Delta\boldsymbol{\epsilon} = \dot{\boldsymbol{\epsilon}}\Delta t$ ). Suppose that all the state variables at  $t_n$ , as well as  $\dot{\boldsymbol{\epsilon}}$ , are known. The task is then to find the other rates of state variables.

It is beneficial to find the relationship between  $\dot{\check{\boldsymbol{\epsilon}}}$  and  $\dot{\boldsymbol{\epsilon}}$ . Taking time derivatives on both sides of the first equation of Eq. (2.17) gives

$$\dot{\check{\boldsymbol{\epsilon}}} = \dot{\mathcal{M}}^{-1} : \boldsymbol{\epsilon} + \mathcal{M}^{-1} : \dot{\boldsymbol{\epsilon}}. \quad (2.46)$$

Firstly  $\dot{\mathcal{M}}^{-1}$  awaits determination. Taking time derivatives on both sides of Eq. (2.15) gives

$$\dot{\mathcal{M}}^{-1} = -\dot{\mathcal{D}}. \quad (2.47)$$

$\dot{\mathcal{D}}$  can be obtained through some derivation as [36]

$$\dot{\mathcal{D}}_{ijmn} = \mathcal{I}_{ijklmn}\dot{d}_{kl} - (1 - \eta) \mathcal{I}_{ijpqmn}\mathcal{Q}_{pqklrs}^- d_{rs}^+ \dot{\check{\boldsymbol{\epsilon}}}_{kl} \equiv \mathcal{I}_{ijklmn}\dot{d}_{kl} - \mathcal{R}_{ijklmn}\dot{\check{\boldsymbol{\epsilon}}}_{kl}, \quad (2.48)$$

where

$$\mathcal{I} = \sum_{i=1}^3 \sum_{j=1}^3 \mathbf{e}_i \otimes \mathbf{e}_j \otimes \mathbf{e}_i \otimes \mathbf{e}_j \otimes \mathbf{e}_i \otimes \mathbf{e}_j. \quad (2.49)$$

$-\mathcal{R}_{ijklmn}\dot{\tilde{\epsilon}}_{kl}$  in Eq. (2.48) is nonzero when some active/inactive damages become inactive/active due to the rotation of the principal stress axes. Noting that, in Eq. (2.48),  $\dot{\tilde{\epsilon}}$  and  $\dot{\mathbf{d}}$  can be arbitrarily chosen gives  $\mathcal{D} = \mathcal{D}(\tilde{\epsilon}, \mathbf{d})$  (or  $\mathcal{M}^{-1} = \mathcal{M}^{-1}(\tilde{\epsilon}, \mathbf{d})$ ) and

$$\frac{\partial \mathcal{D}_{ijmn}}{\partial d_{kl}} = -\frac{\partial \mathcal{M}_{ijmn}^{-1}}{\partial d_{kl}} = \mathcal{I}_{ijklmn} \quad \text{and} \quad \frac{\partial \mathcal{D}_{ijmn}}{\partial \tilde{\epsilon}_{kl}} = -\frac{\partial \mathcal{M}_{ijmn}^{-1}}{\partial \tilde{\epsilon}_{kl}} = -\mathcal{R}_{ijklmn}. \quad (2.50)$$

The first term on the right side of Eq. (2.46) can then be expressed as

$$\dot{\mathcal{M}}_{ijmn}^{-1} \epsilon_{mn} = -\mathcal{I}_{ijklmn} \epsilon_{mn} \dot{d}_{kl} + \mathcal{R}_{ijklmn} \epsilon_{mn} \dot{\tilde{\epsilon}}_{kl}. \quad (2.51)$$

Substituting Eq. (2.51) into Eq. (2.46) gives

$$(\mathcal{I} - \mathcal{R} : \epsilon) : \dot{\tilde{\epsilon}} = -(\mathcal{I} : \epsilon) : \dot{\mathbf{d}} + \mathcal{M}^{-1} : \dot{\epsilon}. \quad (2.52)$$

Eq. (2.52) leads one to find the relationship between  $\dot{\mathbf{d}}$  and  $\dot{\epsilon}$ . Recall that

$$\rho \psi_e(\epsilon, \mathbf{d}^*) = \frac{1}{2} \epsilon : \mathbf{C} : \epsilon = \frac{1}{2} \epsilon : (\mathcal{M}^{-1} : \tilde{\mathcal{C}} : \mathcal{M}^{-1}) : \epsilon. \quad (2.53)$$

Substituting Eq. (2.53) into the third equation of Eq. (2.44) gives

$$\begin{aligned} \mathbf{y} &= -\rho \left( \frac{\partial \psi_e}{\partial \mathbf{d}^*} \right)_{\epsilon} = \frac{1}{2} \epsilon : (\mathcal{I} : \tilde{\mathcal{C}} : \mathcal{M}^{-1} + \mathcal{M}^{-1} : \tilde{\mathcal{C}} : \mathcal{I}) : \epsilon \\ &= \frac{1}{2} \tilde{\epsilon} : \mathcal{M} : (\mathcal{I} : \tilde{\mathcal{C}} : \mathcal{M}^{-1} + \mathcal{M}^{-1} : \tilde{\mathcal{C}} : \mathcal{I}) : \mathcal{M} : \tilde{\epsilon}, \end{aligned} \quad (2.54)$$

which indicates that  $\mathbf{y} = \mathbf{y}(\tilde{\epsilon}, \mathbf{d})$  and that

$$\dot{\mathbf{y}} = \frac{\partial \mathbf{y}}{\partial \tilde{\epsilon}} : \dot{\tilde{\epsilon}} + \frac{\partial \mathbf{y}}{\partial \mathbf{d}} : \dot{\mathbf{d}}. \quad (2.55)$$

The partial derivatives in Eq. (2.55) await determination. Note that

$$\mathcal{M} : \mathcal{M}^{-1} = \mathcal{I}. \quad (2.56)$$

Taking time derivatives on both sides of Eq. (2.56) gives

$$\dot{\mathcal{M}} : \mathcal{M}^{-1} = -\mathcal{M} : \dot{\mathcal{M}}^{-1} \quad \text{or} \quad \dot{\mathcal{M}} = -\mathcal{M} : \dot{\mathcal{M}}^{-1} : \mathcal{M}. \quad (2.57)$$

Combining Eqs. (2.50) and (2.57) gives

$$\frac{\partial \mathcal{M}_{ijmn}}{\partial d_{kl}} = \mathcal{M}_{ijpq} \mathcal{I}_{pqklrs} \mathcal{M}_{rsmn} \quad \text{and} \quad \frac{\partial \mathcal{M}_{ijmn}}{\partial \tilde{\epsilon}_{kl}} = -\mathcal{M}_{ijpq} \mathcal{R}_{pqklrs} \mathcal{M}_{rsmn}. \quad (2.58)$$

The partial derivatives can then be expressed as

$$\begin{aligned} \frac{\partial \mathbf{y}}{\partial \tilde{\epsilon}} &= \frac{1}{2} \left[ \mathcal{M} : \left( \mathcal{J} : \tilde{\mathcal{C}} : \mathcal{M}^{-1} + \mathcal{M}^{-1} : \tilde{\mathcal{C}} : \mathcal{J} \right) : \mathcal{M} : \tilde{\epsilon} \right. \\ &\quad \left. + \tilde{\epsilon} : \mathcal{M} : \left( \mathcal{J} : \tilde{\mathcal{C}} : \mathcal{M}^{-1} + \mathcal{M}^{-1} : \tilde{\mathcal{C}} : \mathcal{J} \right) : \mathcal{M} \right] \\ &\quad + \frac{1}{2} \tilde{\epsilon} : \left[ -\mathcal{M} : \mathcal{R} : \mathcal{M} : \left( \mathcal{J} : \tilde{\mathcal{C}} : \mathcal{M}^{-1} + \mathcal{M}^{-1} : \tilde{\mathcal{C}} : \mathcal{J} \right) : \mathcal{M} \right. \\ &\quad \left. + \mathcal{M} : \left( \mathcal{J} : \tilde{\mathcal{C}} : \mathcal{R} + \mathcal{R} : \tilde{\mathcal{C}} : \mathcal{J} \right) : \mathcal{M} \right. \\ &\quad \left. - \mathcal{M} : \left( \mathcal{J} : \tilde{\mathcal{C}} : \mathcal{M}^{-1} + \mathcal{M}^{-1} : \tilde{\mathcal{C}} : \mathcal{J} \right) : \mathcal{M} : \mathcal{R} : \mathcal{M} \right] : \tilde{\epsilon}, \end{aligned} \quad (2.59)$$

$$\begin{aligned} \frac{\partial \mathbf{y}}{\partial d} &= \frac{1}{2} \tilde{\epsilon} : \left[ \mathcal{M} : \mathcal{J} : \mathcal{M} : \left( \mathcal{J} : \tilde{\mathcal{C}} : \mathcal{M}^{-1} + \mathcal{M}^{-1} : \tilde{\mathcal{C}} : \mathcal{J} \right) : \mathcal{M} \right. \\ &\quad \left. - 2\mathcal{M} : \mathcal{J} : \tilde{\mathcal{C}} : \mathcal{J} : \mathcal{M} \right. \\ &\quad \left. + \mathcal{M} : \left( \mathcal{J} : \tilde{\mathcal{C}} : \mathcal{M}^{-1} + \mathcal{M}^{-1} : \tilde{\mathcal{C}} : \mathcal{J} \right) : \mathcal{M} : \mathcal{J} : \mathcal{M} \right] : \tilde{\epsilon}. \end{aligned} \quad (2.59')$$

Substituting Eq. (2.39) into Eq. (2.52) gives

$$\left[ \mathcal{I} - \mathcal{R} : \epsilon - (\mathcal{J} : \epsilon) : \mathcal{R} \right] : \dot{\tilde{\epsilon}} = -(\mathcal{J} : \epsilon) : \mathcal{S} : \dot{\mathbf{y}} + \mathcal{M}^{-1} : \dot{\epsilon}. \quad (2.60)$$

Let

$$\mathcal{I}^* = \left[ \mathcal{I} - \mathcal{R} : \epsilon - (\mathcal{J} : \epsilon) : \mathcal{R} \right]^{-1}. \quad (2.61)$$

Premultiplying both sides of Eq. (2.60) by  $\mathcal{I}^*$  gives

$$\dot{\tilde{\epsilon}} = -\mathcal{I}^* : (\mathcal{J} : \epsilon) : \mathcal{S} : \dot{\mathbf{y}} + \mathcal{I}^* : \mathcal{M}^{-1} : \dot{\epsilon}. \quad (2.62)$$

Substituting Eq. (2.62) into Eq. (2.39) gives

$$\dot{d} = \left[ \mathcal{I} + \mathcal{R} : \mathcal{I}^* : (\mathcal{J} : \epsilon) \right] : \mathcal{S} : \dot{\mathbf{y}} - \mathcal{R} : \mathcal{I}^* : \mathcal{M}^{-1} : \dot{\epsilon}. \quad (2.63)$$

Substituting Eqs. (2.62) and (2.63) into Eq. (2.55) gives

$$\begin{aligned} \dot{\mathbf{y}} &= \left( \frac{\partial \mathbf{y}}{\partial \tilde{\epsilon}} - \frac{\partial \mathbf{y}}{\partial d} : \mathcal{R} \right) : \mathcal{I}^* : \mathcal{M}^{-1} : \dot{\epsilon} \\ &\quad + \left[ \frac{\partial \mathbf{y}}{\partial d} - \left( \frac{\partial \mathbf{y}}{\partial \tilde{\epsilon}} - \frac{\partial \mathbf{y}}{\partial d} : \mathcal{R} \right) : \mathcal{I}^* : (\mathcal{J} : \epsilon) \right] : \mathcal{S} : \dot{\mathbf{y}}. \end{aligned} \quad (2.64)$$

Substituting Eq. (2.64) into Eq. (2.6) gives

$$\begin{aligned} \dot{\mathbf{y}}(\mathbf{x}) &= \int_{\Omega} \bar{w}(\mathbf{x} - \boldsymbol{\xi}) \left[ \left( \frac{\partial \mathbf{y}}{\partial \tilde{\epsilon}} - \frac{\partial \mathbf{y}}{\partial d} : \mathcal{R} \right) : \mathcal{I}^* : \mathcal{M}^{-1} \right] (\boldsymbol{\xi}) : \dot{\epsilon}(\boldsymbol{\xi}) d\boldsymbol{\xi} \\ &\quad + \int_{\Omega} \bar{w}(\mathbf{x} - \boldsymbol{\xi}) \left\{ \left[ \frac{\partial \mathbf{y}}{\partial d} - \left( \frac{\partial \mathbf{y}}{\partial \tilde{\epsilon}} - \frac{\partial \mathbf{y}}{\partial d} : \mathcal{R} \right) : \mathcal{I}^* : (\mathcal{J} : \epsilon) \right] : \mathcal{S} \right\} (\boldsymbol{\xi}) : \dot{\mathbf{y}}(\boldsymbol{\xi}) d\boldsymbol{\xi}. \end{aligned} \quad (2.65)$$

For notational convenience, let

$$\dot{\mathbf{y}}_0(\mathbf{x}) = \int_{\Omega} \bar{w}(\mathbf{x} - \boldsymbol{\xi}) \left[ \left( \frac{\partial \mathbf{y}}{\partial \tilde{\boldsymbol{\epsilon}}} - \frac{\partial \mathbf{y}}{\partial \mathbf{d}} : \mathcal{R} \right) : \mathcal{I}^* : \mathcal{M}^{-1} \right] (\boldsymbol{\xi}) : \dot{\boldsymbol{\epsilon}}(\boldsymbol{\xi}) \, \mathrm{d}\boldsymbol{\xi}, \quad (2.66)$$

$$\mathcal{K}(\mathbf{x}, \boldsymbol{\xi}) = \bar{w}(\mathbf{x} - \boldsymbol{\xi}) \left\{ \left[ \frac{\partial \mathbf{y}}{\partial \mathbf{d}} - \left( \frac{\partial \mathbf{y}}{\partial \tilde{\boldsymbol{\epsilon}}} - \frac{\partial \mathbf{y}}{\partial \mathbf{d}} : \mathcal{R} \right) : \mathcal{I}^* : (\mathcal{J} : \boldsymbol{\epsilon}) \right] : \mathcal{S} \right\} (\boldsymbol{\xi}). \quad (2.66')$$

Eq. (2.65) can then be rewritten as

$$\dot{\mathbf{y}}(\mathbf{x}) = \dot{\mathbf{y}}_0(\mathbf{x}) + \int_{\Omega} \mathcal{K}(\mathbf{x}, \boldsymbol{\xi}) : \dot{\mathbf{y}}(\boldsymbol{\xi}) \, \mathrm{d}\boldsymbol{\xi}, \quad (2.67)$$

which is a Fredholm integral equation of the second kind [109]. Eq. (2.67) can be solved by iteratively finding  $\dot{\mathbf{y}}_i$ 's ( $i = 1, 2, \dots, n$ ) as follows:

$$\dot{\mathbf{y}}_1(\mathbf{x}) = \dot{\mathbf{y}}_0(\mathbf{x}) + \int_{\Omega} \mathcal{K}(\mathbf{x}, \boldsymbol{\xi}) : \dot{\mathbf{y}}_0(\boldsymbol{\xi}) \, \mathrm{d}\boldsymbol{\xi}, \quad (2.68)$$

$$\dot{\mathbf{y}}_2(\mathbf{x}) = \dot{\mathbf{y}}_0(\mathbf{x}) + \int_{\Omega} \mathcal{K}(\mathbf{x}, \boldsymbol{\xi}) : \dot{\mathbf{y}}_1(\boldsymbol{\xi}) \, \mathrm{d}\boldsymbol{\xi}, \quad (2.68')$$

$$\dots, \quad (2.68'')$$

$$\dot{\mathbf{y}}_n(\mathbf{x}) = \dot{\mathbf{y}}_0(\mathbf{x}) + \int_{\Omega} \mathcal{K}(\mathbf{x}, \boldsymbol{\xi}) : \dot{\mathbf{y}}_{n-1}(\boldsymbol{\xi}) \, \mathrm{d}\boldsymbol{\xi}. \quad (2.68''')$$

The Neumann series solution is then

$$\dot{\mathbf{y}}(\mathbf{x}) = \lim_{n \rightarrow \infty} \dot{\mathbf{y}}_n(\mathbf{x}), \quad (2.69)$$

from which  $\dot{\mathbf{y}}$  can be computed. According to numerical experiments, it generally takes less than 20 iterations for Eq. (2.69) to converge (i.e.,  $n \leq 20$ ). After having reached convergence, substituting  $\dot{\mathbf{y}}$  and  $\dot{\boldsymbol{\epsilon}}$  into Eqs. (2.62) and (2.63) gives  $\dot{\tilde{\boldsymbol{\epsilon}}}$  and  $\dot{\mathbf{d}}$ .

$\dot{\boldsymbol{\sigma}}$  still awaits determination. Taking time derivatives on both sides of the first equation of Eq. (2.16) gives

$$\dot{\boldsymbol{\sigma}} = \dot{\mathcal{C}} : \boldsymbol{\epsilon} + \mathcal{C} : \dot{\boldsymbol{\epsilon}}. \quad (2.70)$$

The first term on the right side of Eq. (2.70) can be further expressed as

$$\begin{aligned}
\dot{\mathbf{c}}_{ijrs}\epsilon_{rs} &= \left( \dot{\mathcal{M}}_{ijmn}^{-1} \tilde{\mathcal{C}}_{mnpq} \mathcal{M}_{pqrs}^{-1} + \mathcal{M}_{ijmn}^{-1} \tilde{\mathcal{C}}_{mnpq} \dot{\mathcal{M}}_{pqrs}^{-1} \right) \epsilon_{rs} \\
&= - \left[ \left( \mathcal{I}_{ijklmn} \dot{d}_{kl} - \mathcal{R}_{ijklmn} \dot{\epsilon}_{kl} \right) \tilde{\mathcal{C}}_{mnpq} \mathcal{M}_{pqrs}^{-1} \right. \\
&\quad \left. + \mathcal{M}_{ijmn}^{-1} \tilde{\mathcal{C}}_{mnpq} \left( \mathcal{I}_{pqklrs} \dot{d}_{kl} - \mathcal{R}_{pqklrs} \dot{\epsilon}_{kl} \right) \right] \epsilon_{rs} \\
&= - \left[ \left( \mathcal{I}_{ijklmn} \tilde{\mathcal{C}}_{mnpq} \mathcal{M}_{pqrs}^{-1} + \mathcal{M}_{ijmn}^{-1} \tilde{\mathcal{C}}_{mnpq} \mathcal{I}_{pqklrs} \right) \epsilon_{rs} \right] \dot{d}_{kl} \\
&\quad + \left[ \left( \mathcal{R}_{ijklmn} \tilde{\mathcal{C}}_{mnpq} \mathcal{M}_{pqrs}^{-1} + \mathcal{M}_{ijmn}^{-1} \tilde{\mathcal{C}}_{mnpq} \mathcal{R}_{pqklrs} \right) \epsilon_{rs} \right] \dot{\epsilon}_{kl} \\
&\equiv - (\mathcal{F}_{ijklrs} \epsilon_{rs}) \dot{d}_{kl} + (\mathcal{G}_{ijklrs} \epsilon_{rs}) \dot{\epsilon}_{kl}.
\end{aligned} \tag{2.71}$$

Substituting Eq. (2.71) into Eq. (2.70) gives

$$\dot{\boldsymbol{\sigma}} = - (\mathcal{F} : \boldsymbol{\epsilon}) : \dot{\mathbf{d}} + (\mathcal{G} : \boldsymbol{\epsilon}) : \dot{\boldsymbol{\epsilon}} + \mathbf{C} : \dot{\boldsymbol{\epsilon}}. \tag{2.72}$$

Since  $\dot{\mathbf{d}}$ ,  $\dot{\boldsymbol{\epsilon}}$ , and  $\dot{\boldsymbol{\epsilon}}$  are all known at the current stage,  $\dot{\boldsymbol{\sigma}}$  can be uniquely determined from Eq. (2.72). Till now, all rates of state variables necessary for updating state variables have been determined. In this work, the present explicit integration scheme is implemented in a Euler–Trapezoidal predictor–corrector method to achieve second-order accuracy.

In this work, the chosen option is to regularize  $\mathbf{y}$ . Another frequently chosen option is to regularize  $\mathbf{d}$  and  $\mathbf{y}$  simultaneously [24–26]. An in-depth investigation indicates that the latter option leads to an integral equation similar to Eq. (2.67) except that this equation is two-level (given that Eq. (2.67) can be treated as a single-level integral equation). Unfortunately, a two-level integral equation cannot be solved explicitly. Although Borino et al. [25] developed a companion implicit time integration scheme, this scheme requires additional degrees of freedom (DOFs) associated with damage (e.g., 2 times more DOFs for materials exhibiting damage anisotropy). As a result, this scheme is somewhat computationally costly and cannot be straightforwardly implemented in a commercial finite element code.

## 2.4 Numerical examples

In this section, the present model will be validated through: 1. simulating cyclic uniaxial tests on a SiC–SiC woven composite; 2. calibrating its associated material parameters via SENB tests on concrete beams. Its versatility will be demonstrated through simulating a mixed-mode fracture test on a DEN specimen. The size effects on fracture paths will be investigated.

### 2.4.1 SiC–SiC woven composite

Ladevèze et al. [110] performed both  $0^\circ$  and  $45^\circ$  cyclic uniaxial tests on a SiC–SiC woven composite having 11 plies (see Figure 2.1 for a schematic of a ply). Zhang and Yu [36] calibrated this composite’s undetermined parameters associated with their “local” model, from these experimental data. Recall that, given uniformly distributed  $\boldsymbol{\epsilon}$  and  $\boldsymbol{d}$ , a nonlocal model is numerically equivalent to a “local” one (so that the characteristic length,  $l_c$ , does not affect the predictions). Considering the similarities between the present model and the model in Ref. [36], here the parameters calibrated by Zhang and Yu [36] will be adopted for validation purposes.

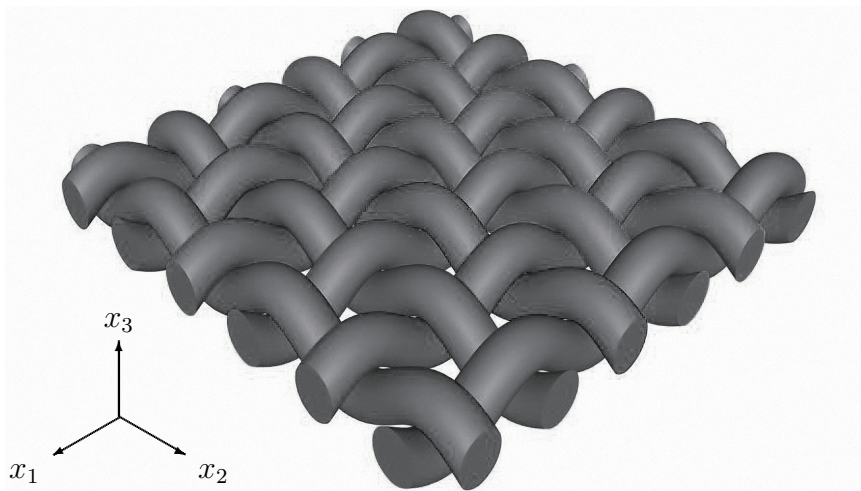


Fig. 2.1. A ply of a SiC–SiC woven composite (adapted from Ref. [110]).

Choose the two mutually perpendicular fiber directions as the  $x_1$ - and  $x_2$ -directions and the thickness direction as the  $x_3$ -direction. Experimental and numerical results [36, 110] indicate that the composite exhibits elastic orthotropy (specifically,  $\tilde{E}_1 = \tilde{E}_2$  due to rotational symmetry, but the composite is not isotropic because  $\tilde{G}_{12} \neq \tilde{E}_1/2(1 + \tilde{\nu}_{12})$ ), damage anisotropy, no compressive damage initiation or evolution, and full damage deactivation. Due to a lack of necessary experimental data, set  $\tilde{E}_3 = \tilde{E}_1$ ,  $\tilde{\nu}_{13} = \tilde{\nu}_{23} = \tilde{\nu}_{12}$ ,  $\tilde{G}_{13} = \tilde{G}_{23} = \tilde{G}_{12}$ ,  $\chi = 1$ ,  $j_{11} = j_{22} = j_{33} = 1$ , and  $j_{12} = j_{13} = j_{23}$  [36]. Figure 2.2 shows the experimental cyclic uniaxial stress–strain curves, and Table 2.1 lists the material parameters directly calibrated from Figure 2.2. Zhang and Yu [36] found that  $j_{12} = 1.06809$  and that

$$B(\beta) = -17.1525\beta^6 + 139.499\beta^5 - 112.650\beta^4 + 37.1191\beta^3 - 2.65531\beta^2 + 0.396641\beta \quad (2.73)$$

(see Ref. [36] for more details on the calibration). The task is then to simulate the cyclic uniaxial tests with all aforementioned parameters.

Table 2.1.  
Predetermined material parameters of a SiC–SiC woven composite.

$\tilde{E}_1$ (GPa)	$\tilde{\nu}_{12}$	$\tilde{G}_{12}$ (GPa)	$k$ (MPa)	$\eta$	$\zeta$
228.379	0.168085	91.1597	0.0230776	0	0

In this work, Abaqus/Explicit is used to simulate all tests, and the present model is implemented in Abaqus/Explicit via VUMAT. Since during a uniaxial test, the stress and the strain fields are uniform in the section of interest (e.g., a gauge section), it is sufficient to simulate such a test with one plane stress, 4-node quadrilateral element (CPS4). Especially, for the 45° test, VUMAT solves the problem in material coordinates  $\boldsymbol{x}$ . It can be verified that here

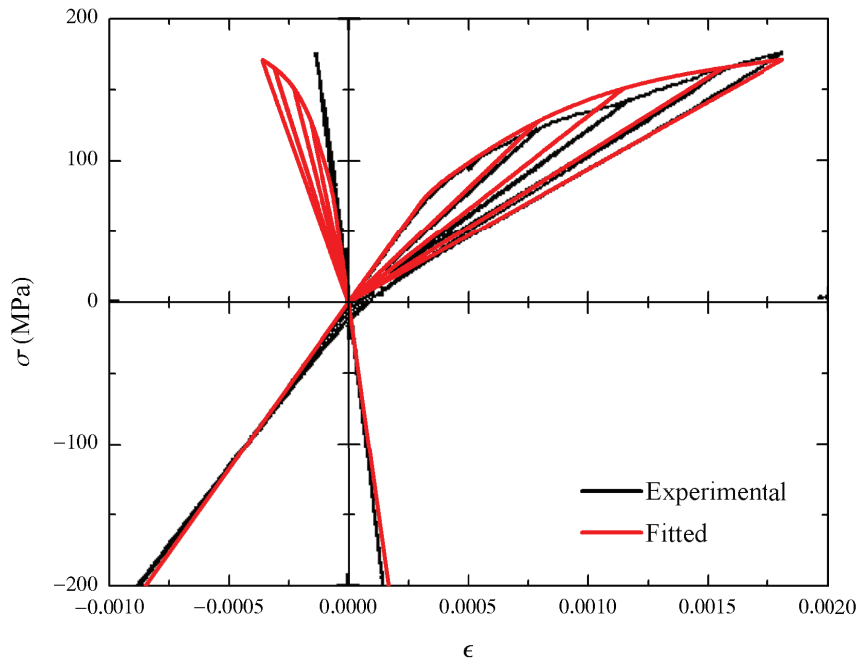
$$\boldsymbol{\sigma} = \begin{bmatrix} \frac{\sigma_{45^\circ}}{2} & \frac{\sigma_{45^\circ}}{2} & 0 \\ \frac{\sigma_{45^\circ}}{2} & \frac{\sigma_{45^\circ}}{2} & 0 \\ 0 & 0 & 0 \end{bmatrix} \quad (2.74)$$

in  $\boldsymbol{x}$ , which is a combination of equal biaxial loading and in-plane shear. Figure 2.2 shows the experimental and the fitted stress–strain curves. As can be seen, for the  $0^\circ$  test, the predictions fit the experimental data well, but for the  $45^\circ$  test, the predictions are slightly overestimated. One possible reason for the overestimation is that Eq. (2.73), as a polynomial fit to the numerical solution of  $B(\beta)$ , causes slight loss of accuracy.

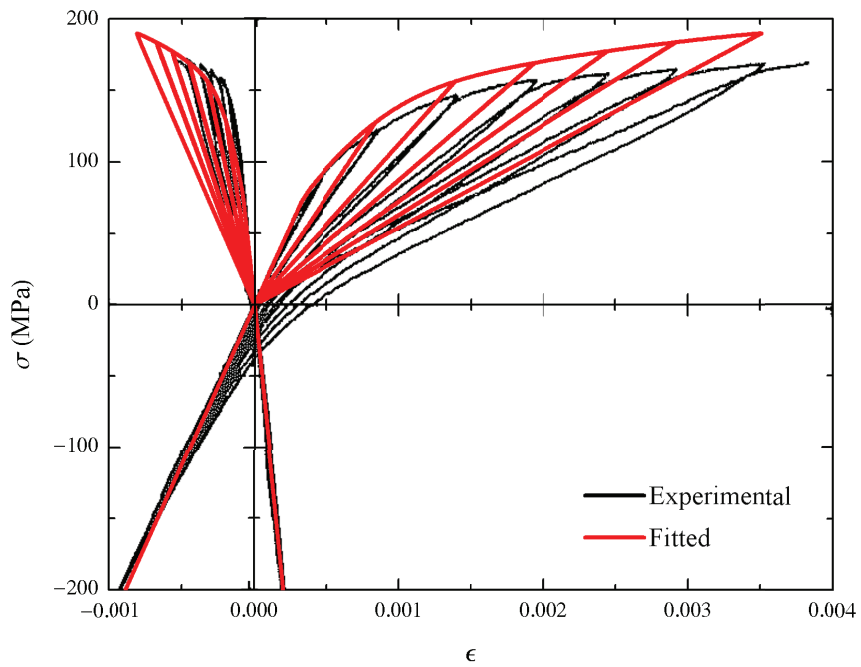
#### 2.4.2 SENB tests

SENB tests are widely used to measure the mode I behavior of concrete [111–114]. Le Bellégo et al. [115, 116] performed a series of SENB tests on concrete beams having different dimensions, measured the load–deflection curve during each test, and calibrated the material parameters associated with their nonlocal model. In this section, the present model will be validated through calibrating its associated material parameters from these experimental data.

Table 2.2 lists the dimensions of different specimens, and Figure 2.3 depicts the experimental setting of the test on the smallest SENB specimens. In each case: 1. the beam width is much smaller than the span length; 2. the front and rear faces of the beam are traction free; 3. the geometry and the loads are both symmetric with respect to the vertical axis of symmetry of the specimen. It is then reasonable to: 1. assume that plane stress conditions prevail over a 2D beam; 2. only consider the left half of the geometry for efficiency purposes. Figure 2.4 shows the finite element model of the left half of the smallest specimen. Each 2D finite element model is meshed with plane stress elements with reduced integration (CPS4R for 4-node, quadrilateral elements and CPS3 for 3-node, triangular elements). Table 2.2 also lists the number of elements in each case. Each region surrounding a potential crack is found to be well resolved, and the sizes of quadrilateral elements in such regions are set to be identical in all cases to accurately capture size effects. Each finite element model is found to be capable of producing converged results.



(a) 0° stress-strain curves.



(b) 45° stress-strain curves.

Fig. 2.2. Experimental and fitted stress-strain curves of a SiC-SiC woven composite.

Table 2.2.  
Specimen dimensions (all in mm) and numbers of elements.

	Span length	Height	Width	Edge notch length	Number of elements
Case 1	240	80	40	8	2,576
Case 2	480	160	40	16	10,944
Case 3	960	320	40	32	43,024

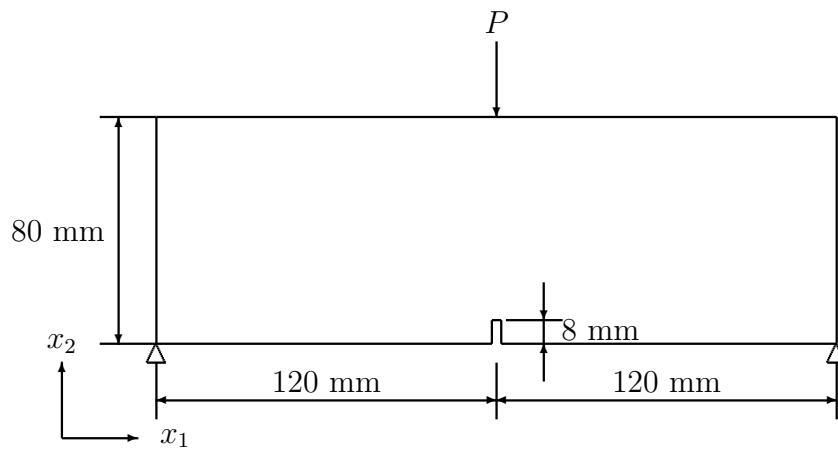


Fig. 2.3. Sketch of an SENB specimen.

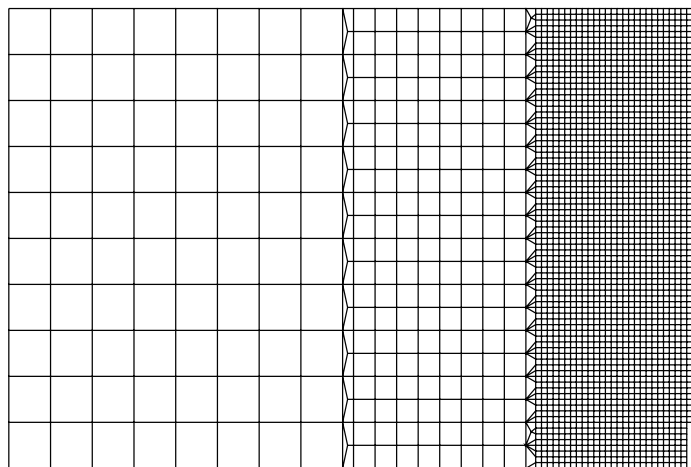


Fig. 2.4. Finite element model of the left half of the smallest SENB specimen.

Experimental observations indicate that all specimens degraded by tensile damage evolution. To facilitate the calibration, assume that the concrete exhibits full damage deactivation ( $\eta = 0$ ) and no compressive damage initiation or evolution ( $\zeta = 0$ ). Due to a lack of necessary experimental data (e.g., those from uniaxial and biaxial tests), assume that the concrete exhibits elastic isotropy, like most other concrete, and for demonstration purposes, set  $\chi = 1$  and  $j_{ij} = 1$  so that the concrete exhibits damage isotropy. Figure 2.5 shows the experimental load–deflection curves (one experimental curve for Case 3 is abandoned because it suggests a much stiffer material), and Table 2.3 lists the material parameters directly calibrated from Figure 2.5. Numerical experiments indicate that an exponential damage accumulation law,

$$B(\beta) = Q [\exp(b\beta) - 1], \quad (2.75)$$

makes the predictions have good fits to the experimental data, where  $b$  describes the rate of damage accumulation, and  $Q$ , together with  $b$ , determines the maximum value of  $B$ , say  $B_{\max}$ . For materials exhibiting damage isotropy,  $0 \leq \beta \leq 1$ , and  $B_{\max} = Q (e^b - 1)$ . The fitted parameters are therefore  $Q$ ,  $b$ , and  $l_c$ .

Table 2.3.  
Predetermined material parameters of a type of concrete.

$\tilde{E}$ (GPa)	$\tilde{\nu}$	$k$ (MPa)	$\eta$	$\zeta$
45.0	0.24	$2.6 \times 10^{-5}$	0	0

The calibration process is primarily a manual trial-and-error process. It consists of the following steps:

1. given that the concrete has an ultimate tensile strength (UTS) of about 1.6 MPa [116], find the values of  $Q$  and  $b$  making the material have this UTS;
2. for Case 1, iteratively adjust  $Q$ ,  $b$ , and  $l_c$ , and find the values of  $Q$ ,  $b$ , and  $l_c$  making the predictions have the best fit to the experimental data;

3. for Cases 2 and 3, repeat the operations at Step 2.

Table 2.4 lists the fitted parameters, and Figure 2.5 shows the experimental and the fitted load–deflection curves. It can be seen that the predictions by the present model fit the experimental data as well as the predictions by Ref. [116]. Despite this similarity, the predictions by the present model are different from those by Ref. [116], mainly in three aspects. First, most fitted parameters here and those in Ref. [116] are not comparable. On one hand,  $Q$  and  $b$ , as two parameters describing damage accumulation, have their respective physical meanings and dimensions. On the other hand, Le Bellégo et al. [116] assumed the damage factor to be a function of an equivalent strain. Recall that this assumption contradicts the principle of maximum dissipation. The fitted parameters in Ref. [116] (except  $l_c$ ) therefore do not have clear physical meanings. Second, Le Bellégo et al. [116] found that their predictions are insensitive to  $l_c$  and suggested that  $l_c$  could vary from 7 mm to 14 mm, but these findings contradict experimental observations. Peerlings et al. [31] and Desmorat et al. [33] found that, for concrete,  $l_c$  might vary from 1 mm to 2 mm. Table 2.4 is in agreement with this finding. Figure 2.6 shows Case 2 load–deflection curves for different values of  $l_c$ , where  $Q$  and  $b$  are held fixed. It can be seen that, as  $l_c$  increases, the load reaches a higher peak value at a larger deflection and more rapid drops afterwards. In fact,  $l_c$  directly determines the width of a strain localization band due to fracture: a low value of  $l_c$  leads to a narrow band, and a high value a wide band. On one hand, creating a wide band requires more work to be done and therefore a high load; on the other hand, the growth of a wide band tends to be unstable and may cause a sudden drop in the load. Third, it is possible that the fracture paths in different specimens are not similar, due to size effects. Le Bellégo et al. [116], however, did not address this issue. There is a need for looking into this issue.

Figure 2.7 shows Case 2 contour plots of  $d_{11}$ , at different stages of deformation, where  $u$  denotes the load point deflections. Recall that  $\chi$  and  $j_{ij}$  are so chosen that the concrete exhibits damage isotropy, or to say, all complements of  $\mathbf{d}$  are equal in entire

Table 2.4.  
Fitted parameters of a type of concrete.

$Q$ (MPa)	$b$	$l_c$ (mm)
$1.235 \times 10^{-5}$	7.5	2.0

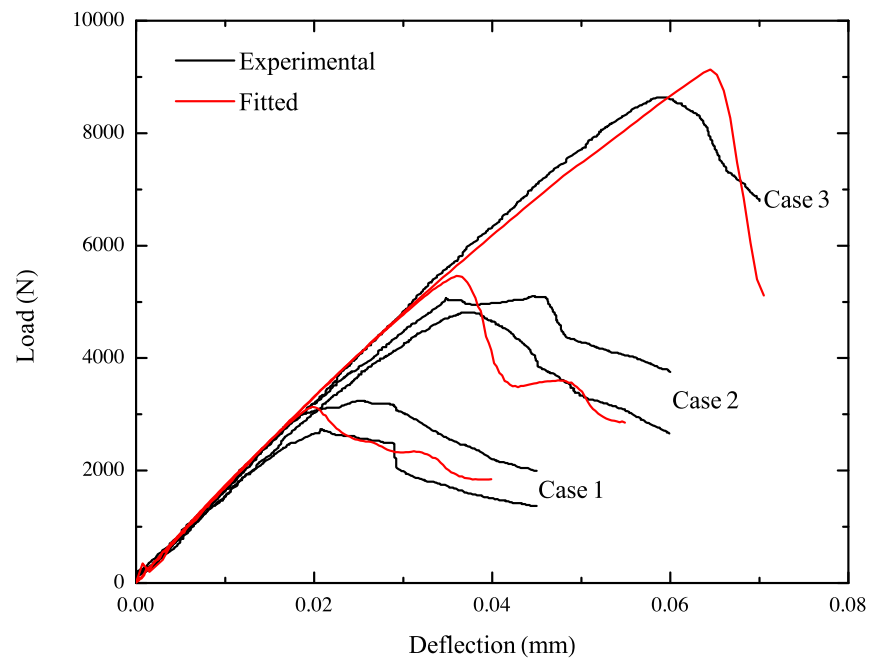


Fig. 2.5. Experimental and fitted load–deflection curves of different specimens.

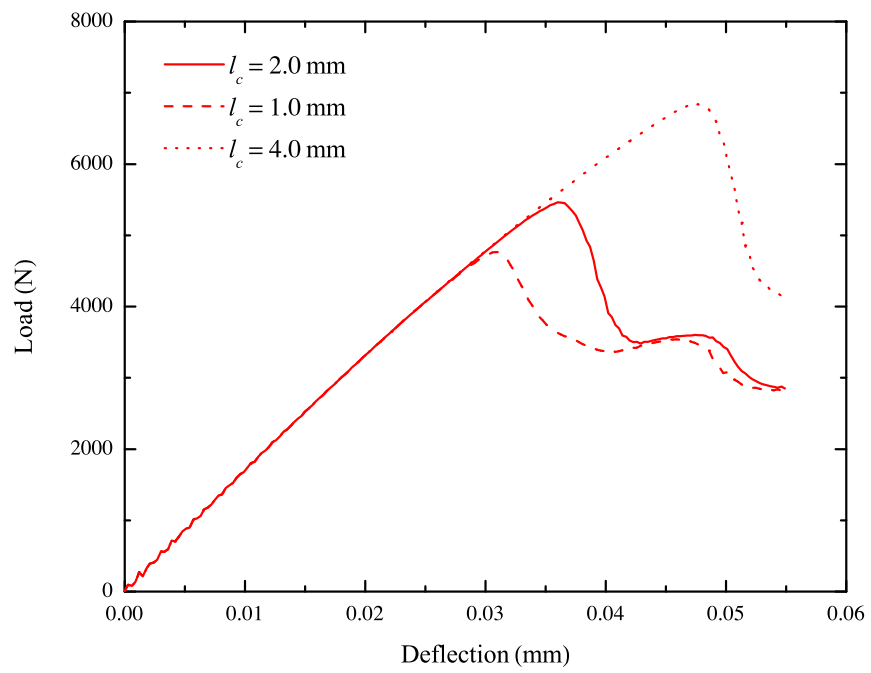


Fig. 2.6. Case 2 load–deflection curves for different values of  $l_c$ .

tension. Accordingly, Figure 2.7 actually indicates that a central crack nucleates at the end notch, propagates along the axis of symmetry, and finally causes structural failure. Similar fracture paths can be found in Refs. [114] and [117]. Figure 2.8 shows the eventual fracture paths in different cases. Since  $l_c$  is held constant in all cases, all strain localization bands in Figure 2.8 have very close widths. In Figure 2.8(a), the central band width approximately equal the edge notch width; in Figure 2.8(b), the central band width is smaller than the edge notch width; in Figure 2.8(c), the edge notch is so wide that two bands nucleate at two corners of the edge notch and propagate simultaneously (only the left half of the geometry is shown). Fracture paths similar to those in Figure 2.8(c) can be found in Ref. [34]. Such differences in fracture paths more or less cause the curves in Figure 2.5 to exhibit different trends. Figure 2.8 again indicates the significance and necessity of calibrating  $l_c$  via experiments.

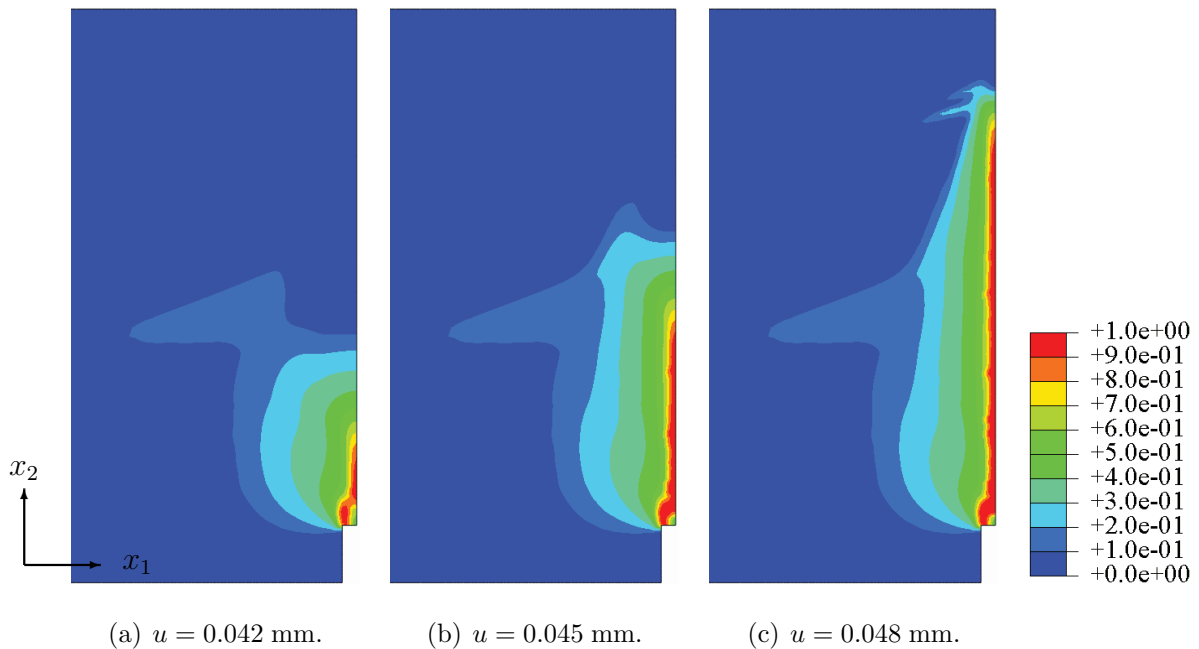


Fig. 2.7. Case 2 contour plots of  $d_{11}$  at different stages of deformation (height: 160 mm).

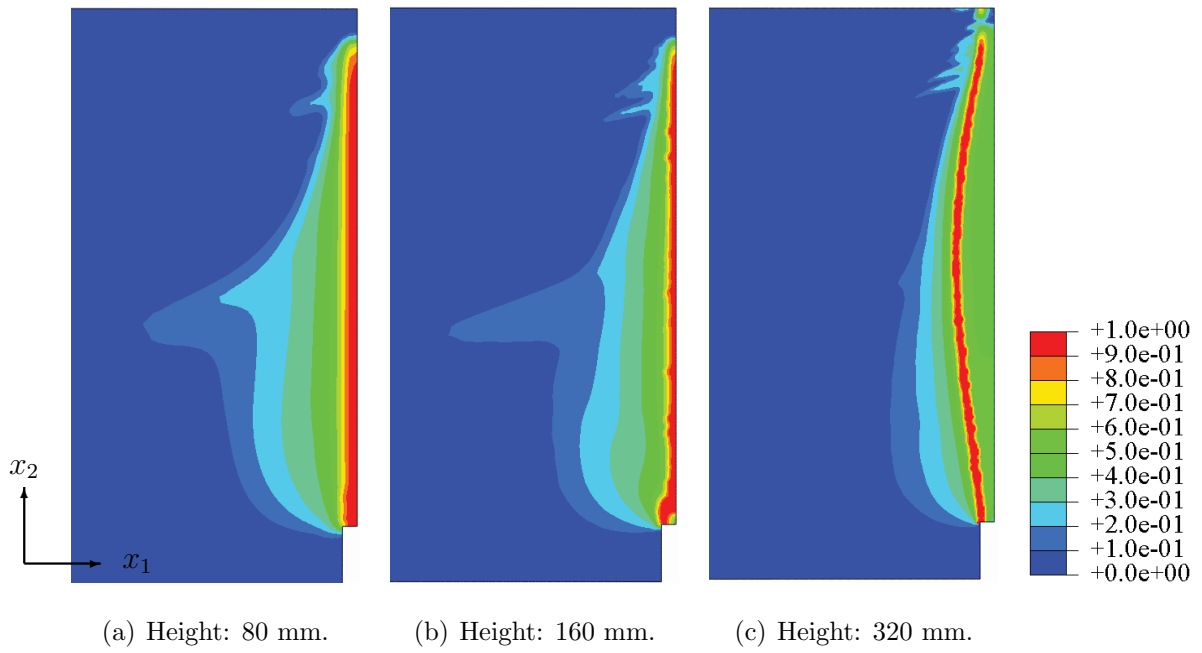


Fig. 2.8. Eventual fracture paths in different cases.

### 2.4.3 Mixed-mode fracture test on a DEN specimen

Nooru-Mohamed [118] designed the so-called mixed-mode fracture test on a DEN specimen, to measure the mixed-mode behavior of concrete. Figure 2.9 depicts the experimental setting of such a test, and Figure 2.10 depicts typical fracture paths during such a test. In Figure 2.9, a DEN specimen is fixed to two pairs of stiff loading frames. One pair of frames moving horizontally, namely the outer frames, can produce a pair of lateral compressive shear forces ( $P_s$ 's), and the other pair moving vertically, namely the inner frames, can produce a pair of axial tensile/compressive forces ( $P_t$ 's). During a test, these two pairs of frames can be moved to produce different combinations of  $P_s$  and  $P_t$  at different instants of time and therefore different loading paths throughout the deformation process. More details on experimental settings can be found in Ref. [118]. In this section, such a test will be simulated to further demonstrate the present model's capability of producing realistic fracture paths.

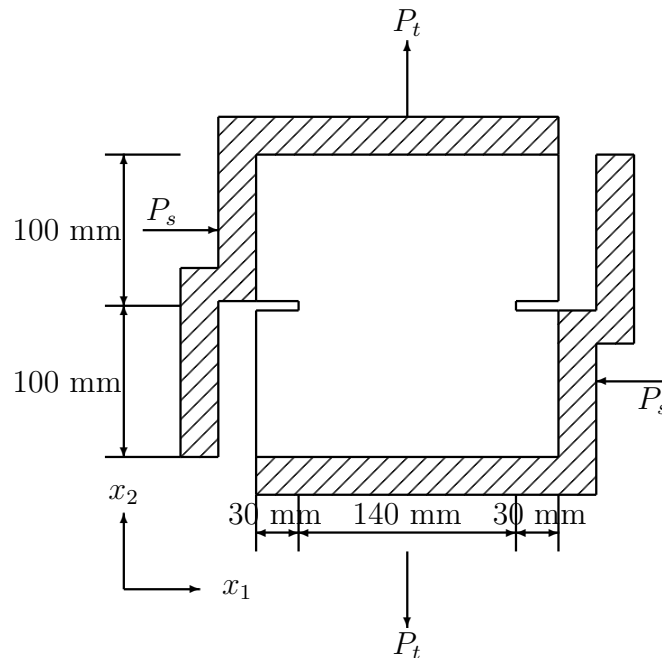


Fig. 2.9. Sketch of a DEN specimen (adapted from Ref. [118]).

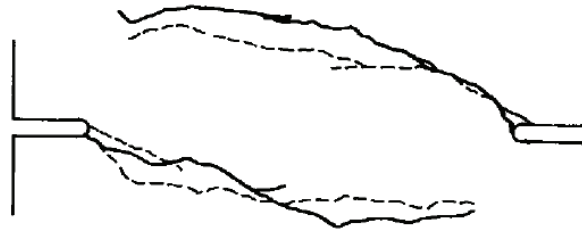


Fig. 2.10. Typical fracture paths during a mixed-mode fracture test: solid line—front view; dash line—back view (duplicated from Ref. [118]).

Figure 2.11 shows the finite element model of the DEN specimen depicted in Figure 2.9. Similarly to Section 2.4.2, assume that plane stress conditions prevail over the specimen. The 2D finite element model is meshed with plane stress 4-node, quadrilateral elements with reduced integration (CPS4R), and the meshed model consists of 20,510 elements. The region surrounding potential cracks is found to be well resolved, and the finite element model is found to be capable of producing converged results. For demonstration purposes, assume that the specimen is made of the same type of concrete as that in Section 2.4.2, and set the loading path to be a proportional loading path described in Ref. [118]. Here a pair of  $P_s$ 's and tensile  $P_t$ 's are applied to the specimen, in a displacement-controlled manner, such that the ratio of the displacement due to each  $P_s$  to the displacement due to each  $P_t$  remains 0.5 throughout the test.

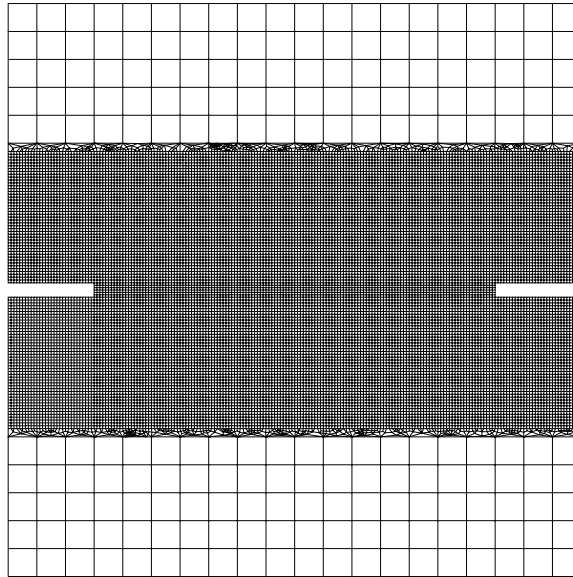


Fig. 2.11. Finite element model of a DEN specimen.

Figure 2.12 shows the contour plots of  $d_{11}$ , at different stages of deformation, and Figure 2.13 the contour plots of  $d_{22}$ , where  $u_t$  denotes the vertical displacement of the top surface of the specimen relative to the bottom surface. Similarly to Figure 2.10, the contour plots in Figures 2.12 and 2.13 are all 180° rotationally symmetric with

respect to the geometric center of the specimen. This is because the geometry and the loads are both rotationally symmetric. Similar findings can be found in Refs. [118] and [119]. Despite some similarities, the contour plots of  $d_{22}$  are prominently different from those of  $d_{11}$ : clearly,  $d_{22}$ 's increase more rapidly than  $d_{11}$ 's during continued deformation. Recall that the concrete is set to exhibit damage isotropy and no compressive damage initiation or evolution. All these indicate that:

1. many material points in a damaged region are subject to tension–compression in principal stress space, and at such a material point, damages neither initiate nor evolve in the direction of  $\mathbf{n}^-$  (see Eqs. (2.40)–(2.42));
2. the specimen is more vulnerable to tensile damages in the  $x_2$ -direction, due to the applied loads.

Similar findings can be found in Ref. [33].

## 2.5 Conclusions

In this chapter, a nonlocal continuum damage model for brittle fracture is developed. A nonlocal damage conjugate force tensor is obtained from the “local” one, using an integral-type regularization technique, and the thermodynamic equations are formulated in a nonlocally generalized standard manner. The nonlocal damage model is developed based on a recently developed “local” model so that it can rigorously handle damage anisotropy, tension–compression asymmetry, and damage deactivation. A fully explicit integration scheme for the present model is developed and then implemented in Abaqus/Explicit via VUMAT.

The following findings can be obtained from the results:

- The present model is found to be capable of handling various mechanical behavior, complex loading conditions, and complex loading paths.
- It is found to be capable of producing realistic fracture paths and capturing size effects in real materials.

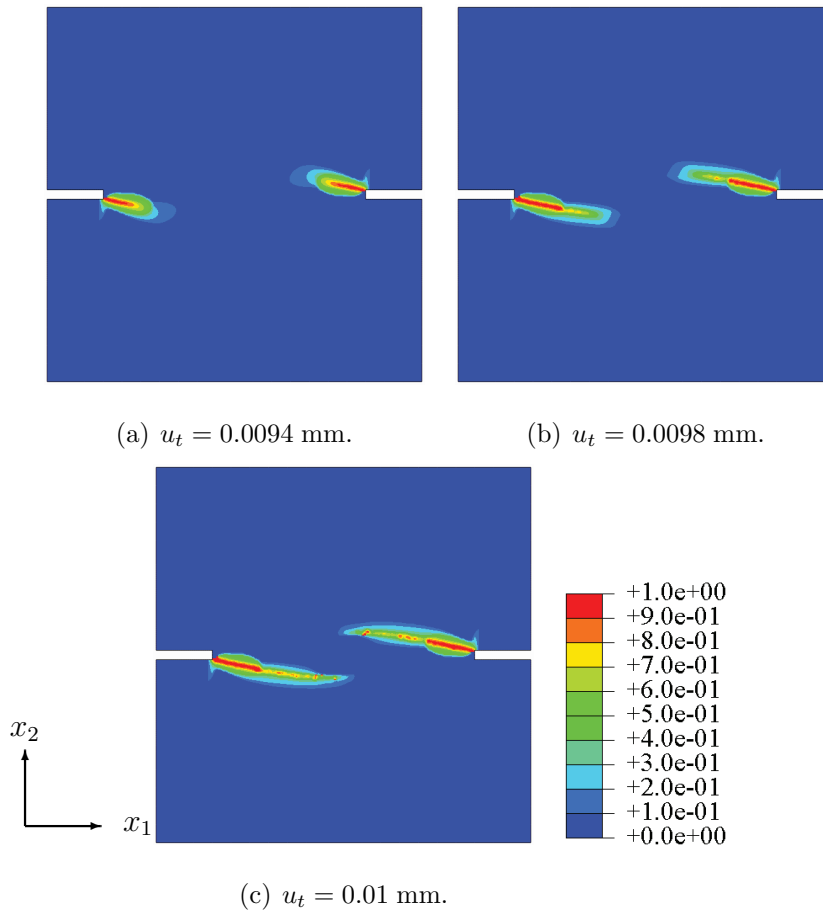


Fig. 2.12. Contour plots of  $d_{11}$  at different stages of deformation (height: 200 mm).

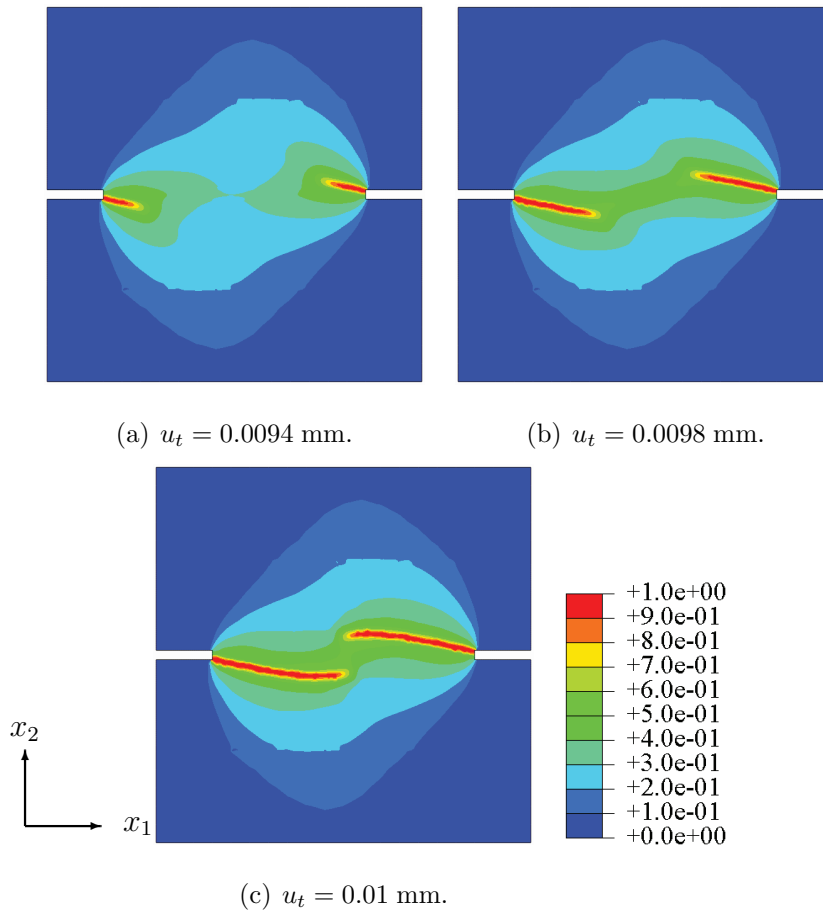


Fig. 2.13. Contour plots of  $d_{22}$  at different stages of deformation (height: 200 mm).

- The characteristic length of heterogeneity is found to significantly affect the predictions and should be calibrated via experiments.

### 3. FATIGUE CONTINUUM DAMAGE MODEL

#### 3.1 Thermodynamics and energy equivalence

This chapter uses the same notation system as that in Chapter 2, and different from those in Chapter 4 and 5. Recall the Helmholtz free energy and state variable definition from Eqs. (2.12) to (2.3). For isothermal deformation, the Clausius–Duhem inequality takes the same form as before:

$$\Phi = \mathbf{y} : \dot{\mathbf{d}} - B\dot{\beta} \geq 0, \quad (3.1)$$

where  $\Phi$  denotes the dissipation per unit volume, and the overdot denotes the time derivative of a quantity. Following Besson et al. [20], assume that there exist a viscodamage potential,  $\Omega$ , defining the evolution of  $\mathbf{d}$  and  $\beta$ , such that

$$\dot{\mathbf{d}} = \frac{\partial \Omega}{\partial \mathbf{y}} \quad \text{and} \quad \dot{\beta} = -\frac{\partial \Omega}{\partial B}. \quad (3.2)$$

Further assume that  $\Omega$  depends on  $\mathbf{y}$  and  $B$  via a damage function,  $f$ , such that

$$\Omega = \Omega(f) \quad \text{and} \quad \dot{v} = \frac{\partial \Omega}{\partial f}, \quad (3.3)$$

where  $\dot{v}$  is referred to as the viscosity function. To this end, choosing a viscodamage model is the equivalence of choosing  $f$  and  $\dot{v}$ . Substituting Eq. (3.3) into Eq. (3.2) gives the damage evolution laws as

$$\dot{\mathbf{d}} = \dot{v} \frac{\partial f}{\partial \mathbf{y}} \quad \text{and} \quad \dot{\beta} = -\dot{v} \frac{\partial f}{\partial B}. \quad (3.4)$$

According to Besson et al. [20],  $\Omega$  must be a convex function of  $\mathbf{y}$  and  $B$ . This, together with Eq. (3.4), implies that  $f$  must be a convex function of  $\mathbf{y}$  and  $B$ . With the effective space concept and the energy equivalence hypothesis, Eqs. (2.12) to (2.18) still stand.

### 3.2 Viscodamage model

Suppose that the material exhibits damage anisotropy, tension-compression asymmetry, and damage deactivation. The damage functions in tension and compression take the same form as in Eq. (2.19), which leads to the unified damage function

$$f(\mathbf{y}, B) = y_{eq} - k - B, \quad (3.5)$$

where  $\mathbf{y}$  and  $y_{eq}$  are used instead of their nonlocal counterparts  $\bar{\mathbf{y}}$  and  $\bar{y}_{eq}$  for the derivation of this viscodamage model. Substituting Eq. (3.5) into Eq. (3.4) gives

$$\dot{\mathbf{d}} = \dot{\nu} \mathbf{n} \quad \text{and} \quad \dot{\beta} = \dot{\nu}, \quad (3.6)$$

where  $\mathbf{n} = \partial f / \partial \mathbf{y} = \partial y_{eq} / \partial \mathbf{y}$  denotes the normal to the damage surface. Last let the viscosity function,  $\dot{\nu}$ , take a similar form to the Perzyna model in viscoplasticity [120], i.e.,

$$\dot{\nu} = \begin{cases} \gamma \left( \frac{f}{k+B} \right)^n & f \geq 0, \\ 0 & f < 0, \end{cases} \quad (3.7)$$

where  $\gamma$  denotes a viscosity parameter, and  $n$  denotes a rate-sensitivity parameter. Till now, all damage parameters have been specified. The time derivative of  $\dot{y}_{eq}$  can be obtained similarly as in the nonlocal damage model, which is expressed as

$$\dot{y}_{eq} = \left[ (1 - \chi) \frac{\mathcal{J} : \mathbf{y}}{\|\mathbf{y}\|_{\mathcal{J}}} + \chi \mathbf{j} \right] : \dot{\mathbf{y}}, \quad (3.8)$$

and leads to

$$\frac{dy_{eq}}{d\mathbf{y}} = \mathbf{n} = (1 - \chi) \frac{\mathcal{J} : \mathbf{y}}{\|\mathbf{y}\|_{\mathcal{J}}} + \chi \mathbf{j}. \quad (3.9)$$

### 3.3 Governing equation for damage evolution

Given all variables at an instant of time,  $t_n$ , the task is to find the correspondence principle between  $\Delta \mathbf{d}$  and its controlling factors (e.g.,  $\Delta \mathbf{y}$  and  $\Delta \tilde{\epsilon}$ ) at  $t_{n+1} = t_n + \Delta t$ , where  $\Delta(\cdot) = (\cdot)_{n+1} - (\cdot)_n$ . Hereafter omit the subscript  $n+1$  on each quantity at  $t_{n+1}$ .

Eq. (3.6) suggests that the unknowns can be chosen as  $\dot{\mathbf{d}}$  and  $\dot{\beta}$ . Eqs. (3.7) and (3.8), together with  $B = B(\beta)$ , further suggest that  $\dot{\mathbf{d}}$  and  $\dot{\beta}$  may both be functions of  $\mathbf{y}$ ,  $\tilde{\epsilon}$ , and  $\beta$ , i.e.,

$$\dot{\mathbf{d}}(t) = \dot{\mathbf{d}}(\mathbf{y}(t), \tilde{\epsilon}(t), \beta(t)) \quad \text{and} \quad \dot{\beta}(t) = \dot{\beta}(\mathbf{y}(t), \tilde{\epsilon}(t), \beta(t)). \quad (3.10)$$

$\Delta \mathbf{d}$ ,  $\Delta \mathbf{y}$ ,  $\Delta \tilde{\epsilon}$ , and  $\Delta \beta$  can be related to  $\dot{\mathbf{d}}$ ,  $\dot{\mathbf{y}}$ ,  $\dot{\tilde{\epsilon}}$ , and  $\dot{\beta}$  by

$$\Delta \mathbf{d} = \dot{\mathbf{d}} \Delta t, \quad \Delta \mathbf{y} = \dot{\mathbf{y}} \Delta t, \quad \Delta \tilde{\epsilon} = \dot{\tilde{\epsilon}} \Delta t, \quad \Delta \beta = \dot{\beta} \Delta t, \quad (3.11)$$

respectively. Here the backward Euler method is adopted because it is A-stable.  $\dot{\mathbf{d}}$  and  $\dot{\beta}$  can be related to  $\dot{\mathbf{d}}_n$  and  $\dot{\beta}_n$  using Taylor expansion at  $t_{n+1}$  by

$$\dot{\mathbf{d}} = \dot{\mathbf{d}}_n + \frac{\partial \dot{\mathbf{d}}}{\partial \mathbf{y}} : \Delta \mathbf{y} + \frac{\partial \dot{\mathbf{d}}}{\partial \tilde{\epsilon}} : \Delta \tilde{\epsilon} + \frac{\partial \dot{\mathbf{d}}}{\partial \beta} \Delta \beta, \quad (3.12)$$

$$\dot{\beta} = \dot{\beta}_n + \frac{\partial \dot{\beta}}{\partial \mathbf{y}} : \Delta \mathbf{y} + \frac{\partial \dot{\beta}}{\partial \tilde{\epsilon}} : \Delta \tilde{\epsilon} + \frac{\partial \dot{\beta}}{\partial \beta} \Delta \beta. \quad (3.12')$$

More details on the partial derivatives in Eq. (3.12) can be found later in Section 3.6.

Substituting  $\Delta \beta = \dot{\beta} \Delta t$  into the above expression for  $\dot{\beta}$  gives

$$\dot{\beta} = \dot{\beta}_n + \frac{\partial \dot{\beta}}{\partial \mathbf{y}} : \Delta \mathbf{y} + \frac{\partial \dot{\beta}}{\partial \tilde{\epsilon}} : \Delta \tilde{\epsilon} + \frac{\partial \dot{\beta}}{\partial \beta} \dot{\beta} \Delta t. \quad (3.13)$$

Rearranging Eq. (3.13) gives

$$\dot{\beta} = \frac{\dot{\beta}_n + \frac{\partial \dot{\beta}}{\partial \mathbf{y}} : \Delta \mathbf{y} + \frac{\partial \dot{\beta}}{\partial \tilde{\epsilon}} : \Delta \tilde{\epsilon}}{1 - \frac{\partial \dot{\beta}}{\partial \beta} \Delta t}. \quad (3.14)$$

Combining Eqs. (3.12) and (3.14) gives

$$\dot{\mathbf{d}} = \dot{\mathbf{d}}^* + \mathbf{S} : \Delta \mathbf{y} + \mathcal{R} : \Delta \tilde{\epsilon}, \quad (3.15)$$

where

$$\dot{\mathbf{d}}^* = \dot{\mathbf{d}}_n + \frac{\dot{\beta}_n \Delta t}{1 - \frac{\partial \dot{\beta}}{\partial \beta} \Delta t} \frac{\partial \dot{\mathbf{d}}}{\partial \beta}, \quad (3.16)$$

$$\mathbf{S} = \frac{\partial \dot{\mathbf{d}}}{\partial \mathbf{y}} + \frac{\frac{\partial \dot{\mathbf{d}}}{\partial \beta} \otimes \frac{\partial \dot{\beta}}{\partial \mathbf{y}}}{1 - \frac{\partial \dot{\beta}}{\partial \beta} \Delta t} \Delta t, \quad \mathcal{R} = \frac{\partial \dot{\mathbf{d}}}{\partial \tilde{\epsilon}} + \frac{\frac{\partial \dot{\mathbf{d}}}{\partial \beta} \otimes \frac{\partial \dot{\beta}}{\partial \tilde{\epsilon}}}{1 - \frac{\partial \dot{\beta}}{\partial \beta} \Delta t} \Delta t \quad (3.16')$$

with  $\dot{\mathbf{d}}^*$  being a viscous term. Rewriting Eq. (3.15) gives the governing equation for damage evolution as

$$\Delta \mathbf{d} = \Delta \mathbf{d}^* + (\mathcal{S} \Delta t) : \Delta \mathbf{y} + (\mathcal{R} \Delta t) : \Delta \tilde{\epsilon}. \quad (3.17)$$

### 3.4 Incremental constitutive relation

It is beneficial to relate  $\dot{\tilde{\epsilon}}$  to  $\dot{\epsilon}$ . The following can be obtained from Eqs. (2.15) and (2.17):

$$\dot{\mathcal{M}}^{-1} = -\dot{\mathcal{D}}, \quad (3.18)$$

$$\dot{\tilde{\epsilon}} = \dot{\mathcal{M}}^{-1} : \epsilon + \mathcal{M}^{-1} : \dot{\epsilon}. \quad (3.19)$$

$\dot{\mathcal{D}}$  can be obtained as

$$\dot{\mathcal{D}}_{ijmn} = \mathcal{I}_{ijklmn} \dot{d}_{kl} - (1 - \eta) \mathcal{I}_{ijpqmn} \mathcal{Q}_{pqklrs}^- d_{rs}^+ \dot{\tilde{\epsilon}}_{kl} \equiv \mathcal{I}_{ijklmn} \dot{d}_{kl} - \mathcal{R}_{ijklmn} \dot{\tilde{\epsilon}}_{kl}, \quad (3.20)$$

where

$$\mathcal{I} = \sum_{i=1}^3 \sum_{j=1}^3 \mathbf{e}_i \otimes \mathbf{e}_j \otimes \mathbf{e}_i \otimes \mathbf{e}_j \otimes \mathbf{e}_i \otimes \mathbf{e}_j \quad (3.21)$$

(see Zhang and Yu [36] for the derivation). Eqs. (3.18) and (3.20) indicate that  $\mathcal{D} = \mathcal{D}(\tilde{\epsilon}, \mathbf{d})$  and  $\mathcal{M}^{-1} = \mathcal{M}^{-1}(\tilde{\epsilon}, \mathbf{d})$ , or to say, that

$$\frac{\partial \mathcal{D}_{ijmn}}{\partial d_{kl}} = -\frac{\partial \mathcal{M}_{ijmn}^{-1}}{\partial d_{kl}} = \mathcal{I}_{ijklmn} \quad \text{and} \quad \frac{\partial \mathcal{D}_{ijmn}}{\partial \tilde{\epsilon}_{kl}} = -\frac{\partial \mathcal{M}_{ijmn}^{-1}}{\partial \tilde{\epsilon}_{kl}} = -\mathcal{R}_{ijklmn}. \quad (3.22)$$

$\dot{\mathcal{M}}^{-1} : \epsilon$  in Eq. (3.19) is then given by

$$\dot{\mathcal{M}}_{ijmn}^{-1} \epsilon_{mn} = -\mathcal{I}_{ijklmn} \epsilon_{mn} \dot{d}_{kl} + \mathcal{R}_{ijklmn} \epsilon_{mn} \dot{\tilde{\epsilon}}_{kl}. \quad (3.23)$$

Combining Eqs. (3.19) and (3.23) gives

$$(\mathcal{I} - \mathcal{R} : \epsilon) : \dot{\tilde{\epsilon}} = -(\mathcal{I} : \epsilon) : \dot{\mathbf{d}} + \mathcal{M}^{-1} : \dot{\epsilon}. \quad (3.24)$$

It is also beneficial to relate  $\dot{\mathbf{d}}$  to  $\dot{\tilde{\epsilon}}$ . Since  $\mathcal{M} : \mathcal{M}^{-1} = \mathcal{I}$ ,

$$\dot{\mathcal{M}} : \mathcal{M}^{-1} = -\mathcal{M} : \dot{\mathcal{M}}^{-1} \quad \text{or} \quad \dot{\mathcal{M}} = -\mathcal{M} : \dot{\mathcal{M}}^{-1} : \mathcal{M}. \quad (3.25)$$

Substituting Eq. (3.25) into Eq. (3.22) gives

$$\frac{\partial \mathcal{M}_{ijmn}}{\partial d_{kl}} = \mathcal{M}_{ijpq} \mathcal{I}_{pqklrs} \mathcal{M}_{rsmn} \quad \text{and} \quad \frac{\partial \mathcal{M}_{ijmn}}{\partial \tilde{\epsilon}_{kl}} = -\mathcal{M}_{ijpq} \mathcal{R}_{pqklrs} \mathcal{M}_{rsmn}. \quad (3.26)$$

Combing Eqs. (2.12) and (2.44) gives

$$\begin{aligned} \mathbf{y} &= -\rho \left( \frac{\partial \psi_e}{\partial \mathbf{d}^*} \right)_\epsilon = \frac{1}{2} \epsilon : \left( \mathcal{I} : \tilde{\mathcal{C}} : \mathcal{M}^{-1} + \mathcal{M}^{-1} : \tilde{\mathcal{C}} : \mathcal{I} \right) : \epsilon \\ &= \frac{1}{2} \tilde{\epsilon} : \mathcal{M} : \left( \mathcal{I} : \tilde{\mathcal{C}} : \mathcal{M}^{-1} + \mathcal{M}^{-1} : \tilde{\mathcal{C}} : \mathcal{I} \right) : \mathcal{M} : \tilde{\epsilon}. \end{aligned} \quad (3.27)$$

Eq. (3.27) indicates that  $\mathbf{y} = \mathbf{y}(\tilde{\epsilon}, \mathbf{d})$ , or to say, that

$$\dot{\mathbf{y}} = \frac{\partial \mathbf{y}}{\partial \tilde{\epsilon}} : \dot{\tilde{\epsilon}} + \frac{\partial \mathbf{y}}{\partial \mathbf{d}} : \dot{\mathbf{d}}. \quad (3.28)$$

Combining Eqs. (3.26)–(3.28) gives

$$\begin{aligned} \frac{\partial \mathbf{y}}{\partial \tilde{\epsilon}} &= \frac{1}{2} \left[ \mathcal{M} : \left( \mathcal{I} : \tilde{\mathcal{C}} : \mathcal{M}^{-1} + \mathcal{M}^{-1} : \tilde{\mathcal{C}} : \mathcal{I} \right) : \mathcal{M} : \tilde{\epsilon} \right. \\ &\quad \left. + \tilde{\epsilon} : \mathcal{M} : \left( \mathcal{I} : \tilde{\mathcal{C}} : \mathcal{M}^{-1} + \mathcal{M}^{-1} : \tilde{\mathcal{C}} : \mathcal{I} \right) : \mathcal{M} \right] \\ &\quad + \frac{1}{2} \tilde{\epsilon} : \left[ -\mathcal{M} : \mathcal{R} : \mathcal{M} : \left( \mathcal{I} : \tilde{\mathcal{C}} : \mathcal{M}^{-1} + \mathcal{M}^{-1} : \tilde{\mathcal{C}} : \mathcal{I} \right) : \mathcal{M} \right. \\ &\quad \left. + \mathcal{M} : \left( \mathcal{I} : \tilde{\mathcal{C}} : \mathcal{R} + \mathcal{R} : \tilde{\mathcal{C}} : \mathcal{I} \right) : \mathcal{M} \right. \\ &\quad \left. - \mathcal{M} : \left( \mathcal{I} : \tilde{\mathcal{C}} : \mathcal{M}^{-1} + \mathcal{M}^{-1} : \tilde{\mathcal{C}} : \mathcal{I} \right) : \mathcal{M} : \mathcal{R} : \mathcal{M} \right] : \tilde{\epsilon}, \\ \frac{\partial \mathbf{y}}{\partial \mathbf{d}} &= \frac{1}{2} \tilde{\epsilon} : \left[ \mathcal{M} : \mathcal{I} : \mathcal{M} : \left( \mathcal{I} : \tilde{\mathcal{C}} : \mathcal{M}^{-1} + \mathcal{M}^{-1} : \tilde{\mathcal{C}} : \mathcal{I} \right) : \mathcal{M} \right. \\ &\quad \left. - 2\mathcal{M} : \mathcal{I} : \tilde{\mathcal{C}} : \mathcal{I} : \mathcal{M} \right. \\ &\quad \left. + \mathcal{M} : \left( \mathcal{I} : \tilde{\mathcal{C}} : \mathcal{M}^{-1} + \mathcal{M}^{-1} : \tilde{\mathcal{C}} : \mathcal{I} \right) : \mathcal{M} : \mathcal{I} : \mathcal{M} \right] : \tilde{\epsilon}. \end{aligned} \quad (3.29)$$

Premultiplying both sides of Eq. (3.28) by  $\mathcal{S}\Delta t$  gives

$$(\mathcal{S}\Delta t) : \Delta \mathbf{y} = (\mathcal{S}\Delta t) : \frac{\partial \mathbf{y}}{\partial \tilde{\epsilon}} : \Delta \tilde{\epsilon} + (\mathcal{S}\Delta t) : \frac{\partial \mathbf{y}}{\partial \mathbf{d}} : \Delta \mathbf{d}. \quad (3.30)$$

Rearranging Eq. (3.17) gives

$$(\mathcal{S}\Delta t) : \Delta \mathbf{y} = \Delta \mathbf{d} - \Delta \mathbf{d}^* - (\mathcal{R}\Delta t) : \Delta \tilde{\epsilon}. \quad (3.31)$$

Solving Eqs. (3.30) and (3.31) for  $\Delta \mathbf{d}$  gives

$$\begin{aligned} \Delta \mathbf{d} &= \left[ \mathcal{I} - \frac{\partial \mathbf{y}}{\partial \mathbf{d}} : (\mathcal{S} \Delta t) \right]^{-1} : \Delta \mathbf{d}^* \\ &\quad + \left[ \mathcal{I} - \frac{\partial \mathbf{y}}{\partial \mathbf{d}} : (\mathcal{S} \Delta t) \right]^{-1} : \left[ (\mathcal{S} \Delta t) : \frac{\partial \mathbf{y}}{\partial \tilde{\boldsymbol{\epsilon}}} + (\mathcal{R} \Delta t) \right] : \Delta \tilde{\boldsymbol{\epsilon}} \\ &\equiv \mathcal{I}^* : \Delta \mathbf{d}^* + \mathcal{E} : \Delta \tilde{\boldsymbol{\epsilon}}. \end{aligned} \quad (3.32)$$

Substituting Eq. (3.32) into Eq. (3.24) gives

$$[\mathcal{I} - \mathcal{R} : \boldsymbol{\epsilon} + (\mathcal{J} : \boldsymbol{\epsilon}) : \mathcal{E}] : \Delta \tilde{\boldsymbol{\epsilon}} = -(\mathcal{J} : \boldsymbol{\epsilon}) : \mathcal{I}^* : \Delta \mathbf{d}^* + \mathcal{M}^{-1} : \Delta \boldsymbol{\epsilon}. \quad (3.33)$$

Let

$$\mathcal{I}^* = [\mathcal{I} - \mathcal{R} : \boldsymbol{\epsilon} + (\mathcal{J} : \boldsymbol{\epsilon}) : \mathcal{E}]^{-1}. \quad (3.34)$$

Premultiplying both sides of Eq. (3.33) by  $\mathcal{I}^*$  gives

$$\Delta \tilde{\boldsymbol{\epsilon}} = -\mathcal{I}^* : (\mathcal{J} : \boldsymbol{\epsilon}) : \mathcal{I}^* : \Delta \mathbf{d}^* + \mathcal{I}^* : \mathcal{M}^{-1} : \Delta \boldsymbol{\epsilon}. \quad (3.35)$$

The rate form of Eq. (2.16) can be obtained as

$$\dot{\boldsymbol{\sigma}} = \dot{\mathcal{C}} : \boldsymbol{\epsilon} + \mathcal{C} : \dot{\boldsymbol{\epsilon}}. \quad (3.36)$$

$\dot{\mathcal{C}} : \boldsymbol{\epsilon}$  in Eq. (3.36) can be expressed as

$$\begin{aligned} \dot{\mathcal{C}}_{ijrs} \epsilon_{rs} &= \left( \dot{\mathcal{M}}_{ijmn}^{-1} \tilde{\mathcal{C}}_{mnpq} \mathcal{M}_{pqrs}^{-1} + \mathcal{M}_{ijmn}^{-1} \tilde{\mathcal{C}}_{mnpq} \dot{\mathcal{M}}_{pqrs}^{-1} \right) \epsilon_{rs} \\ &= - \left[ \left( \mathcal{I}_{ijklmn} \dot{d}_{kl} - \mathcal{R}_{ijklmn} \dot{\epsilon}_{kl} \right) \tilde{\mathcal{C}}_{mnpq} \mathcal{M}_{pqrs}^{-1} \right. \\ &\quad \left. + \mathcal{M}_{ijmn}^{-1} \tilde{\mathcal{C}}_{mnpq} \left( \mathcal{I}_{pqklrs} \dot{d}_{kl} - \mathcal{R}_{pqklrs} \dot{\epsilon}_{kl} \right) \right] \epsilon_{rs} \\ &= - \left[ \left( \mathcal{I}_{ijklmn} \tilde{\mathcal{C}}_{mnpq} \mathcal{M}_{pqrs}^{-1} + \mathcal{M}_{ijmn}^{-1} \tilde{\mathcal{C}}_{mnpq} \mathcal{I}_{pqklrs} \right) \epsilon_{rs} \right] \dot{d}_{kl} \\ &\quad + \left[ \left( \mathcal{R}_{ijklmn} \tilde{\mathcal{C}}_{mnpq} \mathcal{M}_{pqrs}^{-1} + \mathcal{M}_{ijmn}^{-1} \tilde{\mathcal{C}}_{mnpq} \mathcal{R}_{pqklrs} \right) \epsilon_{rs} \right] \dot{\epsilon}_{kl} \\ &\equiv -(\mathcal{F}_{ijklrs} \epsilon_{rs}) \dot{d}_{kl} + (\mathcal{G}_{ijklrs} \epsilon_{rs}) \dot{\epsilon}_{kl}. \end{aligned} \quad (3.37)$$

Combining Eqs. (3.36) and (3.37) gives

$$\dot{\boldsymbol{\sigma}} = -(\mathcal{F} : \boldsymbol{\epsilon}) : \dot{\mathbf{d}} + (\mathcal{G} : \boldsymbol{\epsilon}) : \dot{\boldsymbol{\epsilon}} + \mathcal{C} : \dot{\boldsymbol{\epsilon}}. \quad (3.38)$$

Combining Eqs. (3.32) and (3.38) gives

$$\Delta\boldsymbol{\sigma} = -(\mathcal{F} : \boldsymbol{\epsilon}) : \mathcal{I}^* : \Delta\mathbf{d}^* + [\mathcal{G} : \boldsymbol{\epsilon} - (\mathcal{F} : \boldsymbol{\epsilon}) : \mathcal{E}] : \Delta\tilde{\boldsymbol{\epsilon}} + \mathcal{C} : \Delta\boldsymbol{\epsilon}. \quad (3.39)$$

Substituting Eq. (3.35) into Eq. (3.39) gives the incremental constitutive relation as

$$\Delta\boldsymbol{\sigma} = \mathcal{L} : \Delta\boldsymbol{\epsilon} - \Delta\boldsymbol{\sigma}^*, \quad (3.40)$$

where

$$\mathcal{L} = \mathcal{C} + [\mathcal{G} : \boldsymbol{\epsilon} - (\mathcal{F} : \boldsymbol{\epsilon}) : \mathcal{E}] : \mathcal{I}^* : \mathcal{M}^{-1} \quad (3.41)$$

is a fourth-order tangent operator, and

$$\Delta\boldsymbol{\sigma}^* = \{\mathcal{F} : \boldsymbol{\epsilon} + [\mathcal{G} : \boldsymbol{\epsilon} - (\mathcal{F} : \boldsymbol{\epsilon}) : \mathcal{E}] : \mathcal{I}^* : (\mathcal{J} : \boldsymbol{\epsilon})\} : \mathcal{I}^* : \Delta\mathbf{d}^* \quad (3.42)$$

is a viscous term.

Till now, a closed-form incremental constitutive relation has been derived. The present model can be conveniently implemented in an Euler–Trapezoidal predictor–corrector time integration scheme, for fatigue analysis.

### 3.5 Stress or strain decomposition

One question is whether stress or strain decomposition is valid when modeling tension–compression asymmetry. The problem can be solved in the regime of linear elastic fracture mechanics (LEFM). First consider a horizontal crack subject to in-plane biaxial tension (see Figure 3.1(a)). Set  $0 < \sigma_{22} \ll \sigma_{11}$  so as to make  $\epsilon_{22}$  negative due to the Poisson effect. According to LEFM:

- The positive  $\sigma_{22}$  can cause mode I crack propagation.
- $\sigma_{11}$  has no impact on crack propagation.
- A negative  $\epsilon_{22}$  does not necessarily correspond to crack closure.

Next reverse the signs of  $\sigma_{11}$  and  $\sigma_{22}$  (see Figure 3.1(b)). According to LEFM:

- The negative  $\sigma_{22}$  causes crack closure.
- $\sigma_{11}$  has no impact on crack closure.
- A positive  $\epsilon_{22}$  does not necessarily correspond to crack opening.

It is then clear that only stress decomposition is valid.

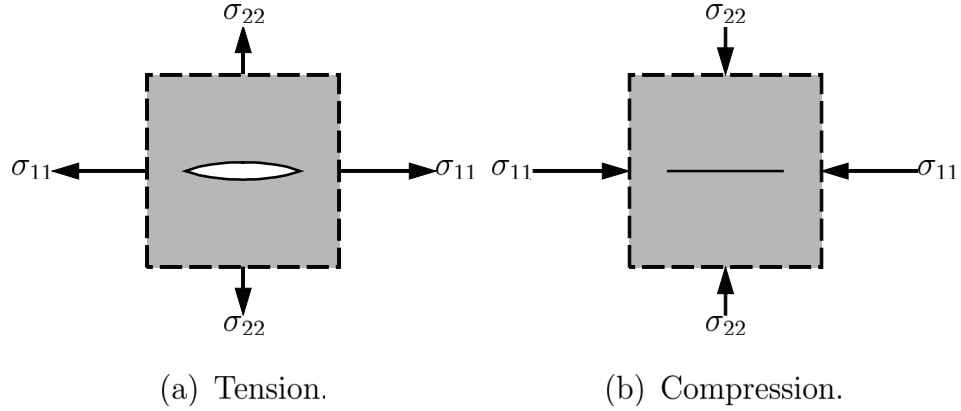


Fig. 3.1. A horizontal crack subject to in-plane biaxial loading.

### 3.6 Partial derivatives

In this section, the expressions for the following partial derivatives will be derived in turn:

$$\frac{\partial \dot{\beta}}{\partial \beta}, \quad \frac{\partial \dot{\mathbf{d}}}{\partial \beta}, \quad \frac{\partial \dot{\beta}}{\partial \mathbf{y}}, \quad \frac{\partial \dot{\mathbf{d}}}{\partial \mathbf{y}}, \quad \frac{\partial \dot{\beta}}{\partial \tilde{\epsilon}}, \quad \frac{\partial \dot{\mathbf{d}}}{\partial \tilde{\epsilon}}. \quad (3.43)$$

Note that  $\dot{\beta} = \dot{v}$ .  $\partial \dot{\beta} / \partial \beta$  can be obtained from Eq. (3.7) as

$$\begin{aligned} \frac{\partial \dot{\beta}}{\partial \beta} &= \frac{\partial \dot{v}}{\partial \beta} = n\gamma \left( \frac{y_{\text{eq}}}{k+B} - 1 \right)^{n-1} \frac{\partial}{\partial \beta} \left( \frac{y_{\text{eq}}}{k+B} - 1 \right) \\ &= - \frac{n\gamma y_{\text{eq}}}{(k+B)^2} \left( \frac{y_{\text{eq}}}{k+B} - 1 \right)^{n-1} \frac{dB}{d\beta}. \end{aligned} \quad (3.44)$$

$\partial \dot{\mathbf{d}} / \partial \beta$  can be obtained from Eq. (3.6) as

$$\frac{\partial \dot{\mathbf{d}}}{\partial \beta} = \frac{\partial}{\partial \beta} (\dot{v} \mathbf{n}) = \frac{\partial \dot{v}}{\partial \beta} \mathbf{n} = - \frac{n\gamma y_{\text{eq}}}{(k+B)^2} \left( \frac{y_{\text{eq}}}{k+B} - 1 \right)^{n-1} \frac{dB}{d\beta} \mathbf{n}. \quad (3.45)$$

$\partial\dot{\beta}/\partial\mathbf{y}$  can be obtained from Eq. (3.7) as

$$\begin{aligned}\frac{\partial\dot{\beta}}{\partial\mathbf{y}} &= \frac{\partial\dot{v}}{\partial\mathbf{y}} = n\gamma\left(\frac{y_{\text{eq}}}{k+B} - 1\right)^{n-1} \frac{\partial}{\partial\mathbf{y}} \left(\frac{y_{\text{eq}}}{k+B} - 1\right) \\ &= \frac{n\gamma}{k+B} \left(\frac{y_{\text{eq}}}{k+B} - 1\right)^{n-1} \mathbf{n}.\end{aligned}\quad (3.46)$$

$\partial\dot{\mathbf{d}}/\partial\mathbf{y}$  can be obtained from Eq. (3.6) as

$$\frac{\partial\dot{\mathbf{d}}}{\partial\mathbf{y}} = \frac{\partial}{\partial\mathbf{y}} (\dot{v}\mathbf{n}) = \mathbf{n} \otimes \frac{\partial\dot{v}}{\partial\mathbf{y}} + \dot{v} \frac{\partial\mathbf{n}}{\partial\mathbf{y}}, \quad (3.47)$$

and  $\partial\mathbf{n}/\partial\mathbf{y}$  can be obtained from Eq. (3.9) as

$$\begin{aligned}\frac{\partial\mathbf{n}}{\partial\mathbf{y}} &= \frac{\partial}{\partial\mathbf{y}} \left[ (1-\chi) \frac{\mathcal{J}:\mathbf{y}}{\|\mathbf{y}\|_{\mathcal{J}}} + \chi\mathbf{j} \right] \\ &= (1-\chi) \frac{\partial}{\partial\mathbf{y}} \left( \frac{1}{\|\mathbf{y}\|_{\mathcal{J}}} \right) \otimes (\mathcal{J}:\mathbf{y}) + \frac{1-\chi}{\|\mathbf{y}\|_{\mathcal{J}}} \frac{\partial}{\partial\mathbf{y}} (\mathcal{J}:\mathbf{y}) \\ &= (1-\chi) \left( -\frac{1}{\|\mathbf{y}\|_{\mathcal{J}}^2} \frac{\partial\|\mathbf{y}\|_{\mathcal{J}}}{\partial\mathbf{y}} \right) \otimes (\mathcal{J}:\mathbf{y}) + \frac{1-\chi}{\|\mathbf{y}\|_{\mathcal{J}}} \mathcal{J} \\ &= \frac{1-\chi}{\|\mathbf{y}\|_{\mathcal{J}}} \left[ \mathcal{J} - \frac{(\mathcal{J}:\mathbf{y}) \otimes (\mathcal{J}:\mathbf{y})}{\|\mathbf{y}\|_{\mathcal{J}}^2} \right].\end{aligned}\quad (3.48)$$

Combining Eqs. (3.46)–(3.48) gives

$$\begin{aligned}\frac{\partial\dot{\mathbf{d}}}{\partial\mathbf{y}} &= \frac{n\gamma}{k+B} \left(\frac{y_{\text{eq}}}{k+B} - 1\right)^{n-1} \mathbf{n} \otimes \mathbf{n} \\ &\quad + \frac{\gamma(1-\chi)}{\|\mathbf{y}\|_{\mathcal{J}}} \left(\frac{y_{\text{eq}}}{k+B} - 1\right)^n \left[ \mathcal{J} - \frac{(\mathcal{J}:\mathbf{y}) \otimes (\mathcal{J}:\mathbf{y})}{\|\mathbf{y}\|_{\mathcal{J}}^2} \right].\end{aligned}\quad (3.49)$$

$\partial\dot{\beta}/\partial\tilde{\boldsymbol{\epsilon}}$  can be obtained from Eq. (3.7) as

$$\begin{aligned}\frac{\partial\dot{\beta}}{\partial\tilde{\boldsymbol{\epsilon}}} &= \frac{\partial\dot{v}}{\partial\tilde{\boldsymbol{\epsilon}}} = n\gamma\left(\frac{y_{\text{eq}}}{k+B} - 1\right)^{n-1} \frac{\partial}{\partial\tilde{\boldsymbol{\epsilon}}} \left(\frac{y_{\text{eq}}}{k+B} - 1\right) \\ &= -\frac{n\gamma}{k+B} \left(\frac{y_{\text{eq}}}{k+B} - 1\right)^{n-1} \boldsymbol{\kappa},\end{aligned}\quad (3.50)$$

where the third equality holds due to Eq. (3.9).  $\partial\dot{\mathbf{d}}/\partial\tilde{\boldsymbol{\epsilon}}$  can be obtained from Eq. (3.6)

as

$$\frac{\partial\dot{\mathbf{d}}}{\partial\tilde{\boldsymbol{\epsilon}}} = \frac{\partial}{\partial\tilde{\boldsymbol{\epsilon}}} (\dot{v}\mathbf{n}) = \mathbf{n} \otimes \frac{\partial\dot{v}}{\partial\tilde{\boldsymbol{\epsilon}}} + \dot{v} \frac{\partial\mathbf{n}}{\partial\tilde{\boldsymbol{\epsilon}}}, \quad (3.51)$$

and  $\partial \mathbf{n} / \partial \tilde{\epsilon}$  can be obtained from Eq. (3.9) as

$$\begin{aligned} \frac{\partial \mathbf{n}}{\partial \tilde{\epsilon}} &= \frac{\partial}{\partial \tilde{\epsilon}} \left[ (1 - \chi) \frac{\mathcal{J} : \mathbf{y}}{\|\mathbf{y}\|_{\mathcal{J}}} + \chi \mathbf{j} \right] \\ &= (1 - \chi) \frac{\partial}{\partial \tilde{\epsilon}} \left( \frac{1}{\|\mathbf{y}\|_{\mathcal{J}}} \right) \otimes (\mathcal{J} : \mathbf{y}) + \frac{1 - \chi}{\|\mathbf{y}\|_{\mathcal{J}}} \frac{\partial}{\partial \tilde{\epsilon}} (\mathcal{J} : \mathbf{y}) + \chi \frac{\partial \mathbf{j}}{\partial \tilde{\epsilon}}. \end{aligned} \quad (3.52)$$

Note that

$$\frac{\partial}{\partial \tilde{\epsilon}_{ij}} \left( \frac{1}{\|\mathbf{y}\|_{\mathcal{J}}} \right) = -\frac{1}{\|\mathbf{y}\|_{\mathcal{J}}^2} \frac{\partial \|\mathbf{y}\|_{\mathcal{J}}}{\partial \tilde{\epsilon}_{ij}} = \frac{y_{kl} \mathcal{K}_{klijmn} y_{mn}}{2 \|\mathbf{y}\|_{\mathcal{J}}^3}, \quad (3.53)$$

$$\frac{\partial}{\partial \tilde{\epsilon}_{kl}} (\mathcal{J}_{ijmn} y_{mn}) = -\mathcal{K}_{ijklmn} y_{mn}. \quad (3.53')$$

Combining Eqs.(3.52) and (3.53) gives

$$\frac{\partial \mathbf{n}}{\partial \tilde{\epsilon}} = \frac{1 - \chi}{2 \|\mathbf{y}\|_{\mathcal{J}}^3} (\mathbf{y} : \mathcal{K} : \mathbf{y}) \otimes (\mathcal{J} : \mathbf{y}) - \frac{1 - \chi}{\|\mathbf{y}\|_{\mathcal{J}}} \mathcal{K} : \mathbf{y} - \chi \mathcal{K}. \quad (3.54)$$

Combining Eqs. (3.50), (3.51), and (3.54) gives

$$\begin{aligned} \frac{\partial \dot{\mathbf{d}}}{\partial \tilde{\epsilon}} &= -\frac{n\gamma}{k + B} \left( \frac{y_{\text{eq}}}{k + B} - 1 \right)^{n-1} \mathbf{n} \otimes \boldsymbol{\kappa} \\ &+ \gamma \left( \frac{y_{\text{eq}}}{k + B} - 1 \right)^n \left[ \frac{1 - \chi}{2 \|\mathbf{y}\|_{\mathcal{J}}^3} (\mathbf{y} : \mathcal{K} : \mathbf{y}) \otimes (\mathcal{J} : \mathbf{y}) - \frac{1 - \chi}{\|\mathbf{y}\|_{\mathcal{J}}} \mathcal{K} : \mathbf{y} - \chi \mathcal{K} \right]. \end{aligned} \quad (3.55)$$

### 3.7 Numerical examples

In this section, the present model will be validated through model calibration via:

- cyclic compression tests on a concrete;
- cyclic tensile tests on another concrete;
- cyclic tensile tests on a unidirectional IM7/8552 fiber-reinforced composite in its longitudinal and transverse directions, respectively.

Different calibration methods will be proposed. The feasibility of calibrating a continuum damage model from S–N and modulus degradation/maximum strain–cycle curves will be evaluated.

### 3.7.1 Concrete in compression

Gao and Hsu [49] conducted cyclic compression tests on a concrete, measured its modulus degradation–cycle relationship during one test, and obtained its S–N relationship from all tests. The task is to determine all its material parameters.

Set the loading direction to be the  $x_1$ -direction. Assume that the elastically isotropic concrete exhibits damage anisotropy with  $\chi = 0.5$  and  $j_{ij}^- = 1$ . Figure 3.2 shows the experimental S–N and modulus degradation–cycle relationships, where  $N$  denotes the number of cycles, and  $N_f$  its value at the onset of failure. Table 3.1 lists the following predetermined parameters:

- $\tilde{E}$ —initial Young’s modulus reported in Ref. [49];
- $\tilde{\nu}$ —initial Poisson’s ratio taking a value common for concrete;
- $f_c$ —the static compressive strength of the concrete, reported in Ref. [49];
- $k^-$ —calibrated from the fatigue limit ( $0.7f_c$  in Figure 3.2(a)).

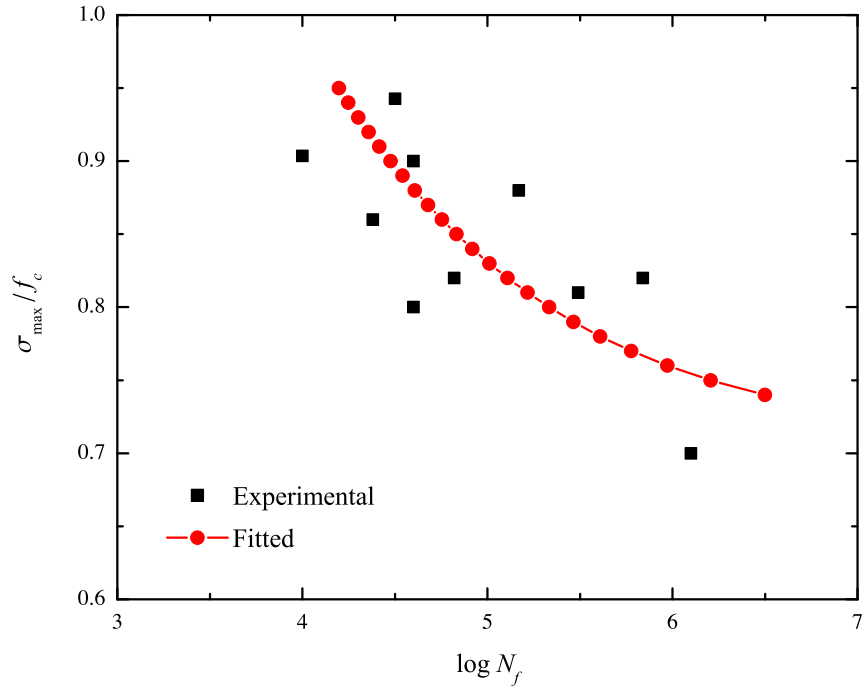
Following Ref. [49], apply a sinusoidal compressive stress ranging from 0 MPa to a maximum stress, say  $\sigma_{\max}$ , with a frequency of 4 Hz, when simulating each test. Numerical experiments indicate that  $B^-(\beta)$  can take the form of

$$B^- = Q^- [\exp(b\beta) - 1], \quad (3.56)$$

where  $Q^-$  and  $b$  not only affect the rate of damage evolution but also determine the maximum value of  $B^-$ , say  $B_{\max}^-$ . According to numerical experiments, the maximum value of  $\beta$  is close to unity, and  $B_{\max}^-$  is close to  $Q^- (e^b - 1)$ .  $Q^-$ ,  $b$ ,  $\gamma$ , and  $n$  are then the fitted parameters.

In this work:

1. Monte Carlo experiments are used to create the guessed values of the fitted parameters, which are close to the solution.



(a) S-N curves.

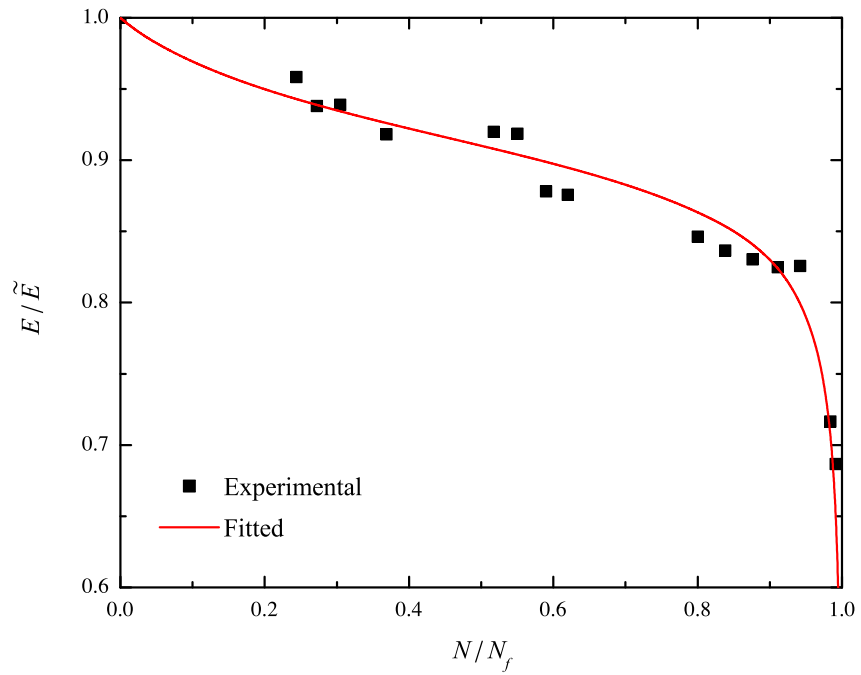
(b) Modulus degradation-cycle curves for  $\sigma_{\max} = 0.6f_c$ .

Fig. 3.2. (a) S-N and (b) modulus degradation-cycle curves of a concrete in compression.

2. When starting close to the solution, the method of nonlinear least squares has a good chance to converge to the global optimum [121] and is therefore used for curve fitting.

Numerical experiments indicate the following:

- A predicted modulus degradation–cycle curve is sensitive to  $Q^-$  and  $b$  but insensitive to  $\gamma$  or  $n$ .
- A predicted S–N curve is sensitive to  $Q^-$ ,  $b$ ,  $\gamma$ , and  $n$ .

The fitted parameters can then be calibrated as follows:

1. Roughly estimate  $\gamma$  and  $n$  through numerical experiments.
2. Hold  $\gamma$  and  $n$  fixed, and iteratively adjust  $Q^-$  and  $b$  till their values make the predicted modulus degradation–cycle curve the curve of best fit.
3. Hold  $Q^-$  and  $b$  fixed, and iteratively adjust  $\gamma$  and  $n$  till their values make the predicted S–N curve the curve of best fit.

Table 3.1.  
Predetermined parameters of a concrete.

$\tilde{E}$ (GPa)	$\tilde{\nu}$	$f_c$ (MPa)	$k^-$ (MPa)
35.45	0.2	−34.6	0.0167

Table 3.2.  
Fitted parameters of a concrete.

$Q^-$ (MPa)	$b$	$\gamma$ (s <sup>−1</sup> )	$n$
0.0153	3.50	$3.48 \times 10^{-4}$	2.39

Table 3.2 lists the fitted parameters, and Figure 3.2 compares the fitted curves with the experimental data. In Figure 3.2(b), the predicted curve can be divided into the following segments:

1. a gradually decreasing one due to stable microcrack propagation and new microcrack initiation;
2. a rapidly decreasing one due to microcrack coalescence and unstable macrocrack propagation.

This agrees well with experimental observations. In Figure 3.2(a):

- The predicted curve is the curve of best fit for the sparsely distributed experimental data points.
- It is  $C^1$  continuous and exhibits an asymptotic trend near the fatigue limit.
- Unlike the predictions by some other models, its extrapolated value at  $\log N_f = 0$  does not equal  $f_c$ .

First, the predicted curve trend is realistic and complete for high numbers of cycles. Figure 3.3 depicts a typical empirical S–N curve. Unlike the predicted curve, the empirical curve is piecewise linear and seems ad hoc and oversimplified. Meanwhile, the curves predicted by other continuum damage models seldom exhibit prominent asymptotic trends near fatigue limits. Clearly, the present model can handle high-cycle compressive fatigue. Second, the third point does no harm to the present model's validity due to the following reasons:

- The present model is designed to handle high-cycle fatigue, and modeling low-cycle fatigue accompanied by plastic deformation is beyond the scope of this work.
- Cyclic loading with a frequency varying from 4 Hz to 6 Hz is more of dynamic loading, and the dynamic strength of a material is usually higher than the static strength.

On the one hand, the high-cycle segment of an S–N curve often exhibits a different trend from the low-cycle segment, making its extrapolated value at  $\log N_f = 0$  higher than the static strength (see Figure 3.3 for example). On the other hand, if there is experimental evidence indicating that the extrapolated value equals the static strength, this restriction can be imposed to the model calibration using a penalty method.

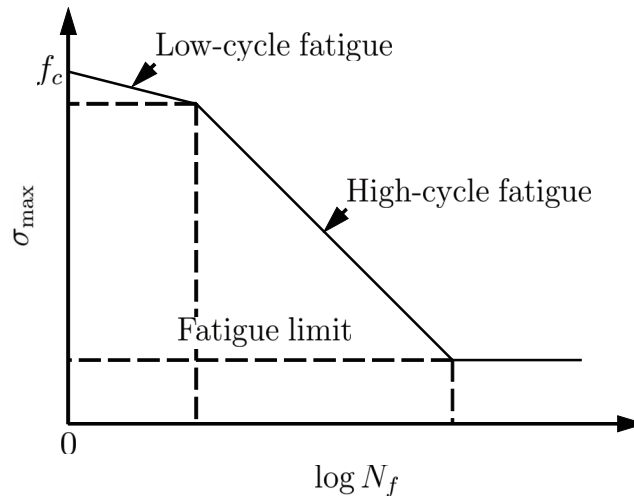


Fig. 3.3. Empirical S–N curve.

### 3.7.2 Concrete in tension

Cornelissen and Reinhardt [122] conducted cyclic tensile tests on another concrete, measured its maximum strain–cycle curve during one test, and obtained its S–N curve from all tests. The task is to determine all its material parameters.

Table 3.3.  
Predetermined parameters of another concrete.

$\tilde{E}$ (GPa)	$\tilde{\nu}$	$f_t$ (MPa)	$k^+$ (MPa)
36.14	0.2	2.46	$7.4 \times 10^{-5}$

Table 3.4.  
Fitted parameters of another concrete.

$Q^+$ (MPa)	$b$	$\gamma$ (s <sup>-1</sup> )	$n$
0.0350	0.0110	0.0115	2.11

Set the loading direction to be the  $x_1$ -direction. Assume that the elastically isotropic concrete exhibits damage anisotropy with  $\chi = 0.5$  and  $j_{ij}^+ = 1$ . Figure 3.4 shows the experimental S–N and maximum strain–cycle curves, where  $\epsilon_{\max}$  denotes the maximum strain in each cycle. Table 3.3 lists the following predetermined parameters:

- $\tilde{E}$ —reported in Ref. [122];
- $\tilde{\nu}$ —taking a value common for concrete;
- $f_t$ —the static tensile strength of the concrete, reported in Ref. [122];
- $k^+$ —calibrated from the fatigue limit ( $0.65f_t$  in Figure 3.4(a)).

Following Ref. [122], apply a sinusoidal tensile stress ranging from  $0.2f_t$  to  $\sigma_{\max}$ , with a frequency of 6 Hz, when simulating each test. Numerical experiments indicate that  $B^+(\beta)$  can take the form of

$$B^+ = Q^+ [\exp(b\beta) - 1]. \quad (3.57)$$

$Q^+$ ,  $b$ ,  $\gamma$ , and  $n$  are then the fitted parameters.

Here the fitted parameters are calibrated as follows:

1. Roughly estimate  $\gamma$  and  $n$  through numerical experiments.
2. Hold  $\gamma$  and  $n$  fixed, and iteratively adjust  $Q^+$  and  $b$  till their values make the predicted maximum strain–cycle curve the curve of best fit.
3. Hold  $Q^+$  and  $b$  fixed, and iteratively adjust  $\gamma$  and  $n$  till their values make the predicted S–N curve the curve of best fit.

Table 3.4 lists the fitted parameters, and Figure 3.4 compares the fitted curves with the experimental data. Cornelissen and Reinhardt [122] assumed a linear relationship between  $\log N_f$  and  $\sigma_{\max}/f_t$  and replaced the original experimental data with a straight line shown in Figure 3.4(a). Although the straight line is ad hoc and

oversimplified, the predicted curve can only be its curve of best fit while including the fatigue limit. Since the predicted curve trend here is similar to that in Figure 3.2(a), the corresponding discussion for Figure 3.2(a) holds here. In Figure 3.4(b), the predicted curve can be divided into the following segments:

1. a rapidly increasing one due to unstable preexisting microcrack propagation until a stable state is reached
2. a gradually increasing one due to stable microcrack propagation and new microcrack initiation
3. a rapidly increasing one due to microcrack coalescence and unstable macrocrack propagation

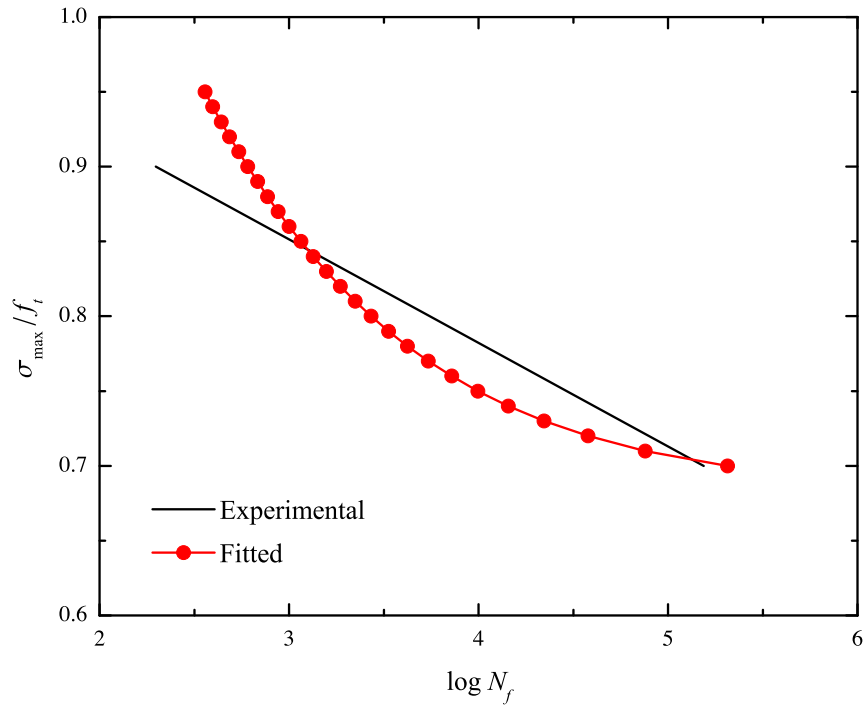
These segments correspond to the well-known three stages of fatigue failure [46]. It is worth noting that the first stage is not prominent in Figure 3.4(b). This is possibly because preexisting microcrack propagation becomes stable in compression. In conclusion, the above discussion indicates that the present model can handle high-cycle tensile fatigue.

### 3.7.3 Fiber-reinforced composite in tension

Cole et al. [123] conducted cyclic tensile tests on a unidirectional IM7/8552 fiber-reinforced composite in its longitudinal and transverse directions, respectively, measured its maximum strain-cycle curves during some of the tests, and obtained its longitudinal and transverse S–N relationships from all tests. The task is to determine all its material parameters. Here focus is placed on modeling high-cycle anisotropic fatigue in the framework of continuum mechanics. The problem can be solved more rigorously using micromechanics models [38, 124].

Set the longitudinal direction of the composite to be the  $x_1$ -direction. Due to insufficient experimental data, assume the following:

- The composite exhibits transversely isotropy in the  $x_2x_3$  plane.



(a) S-N curves.

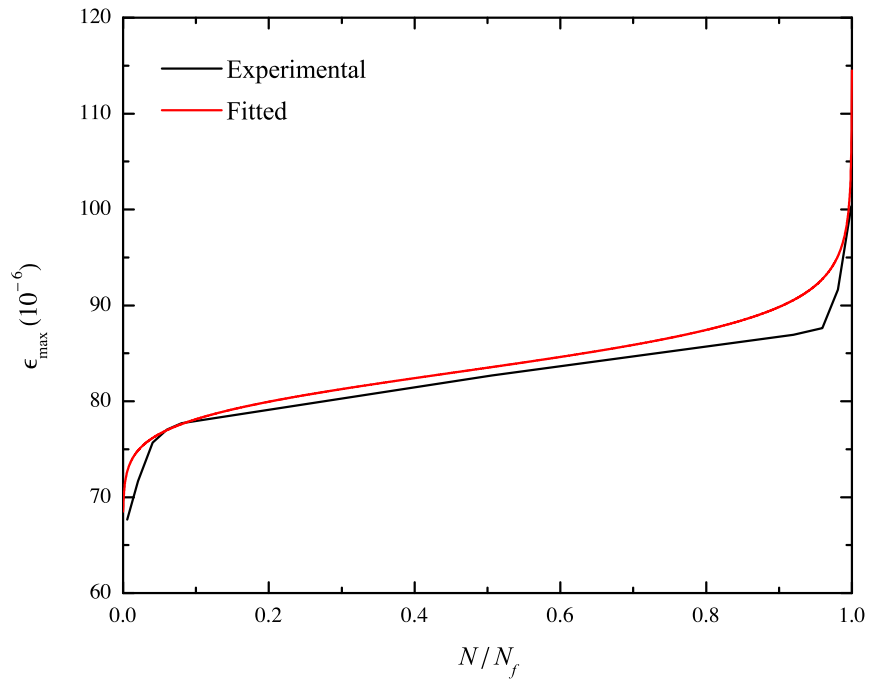
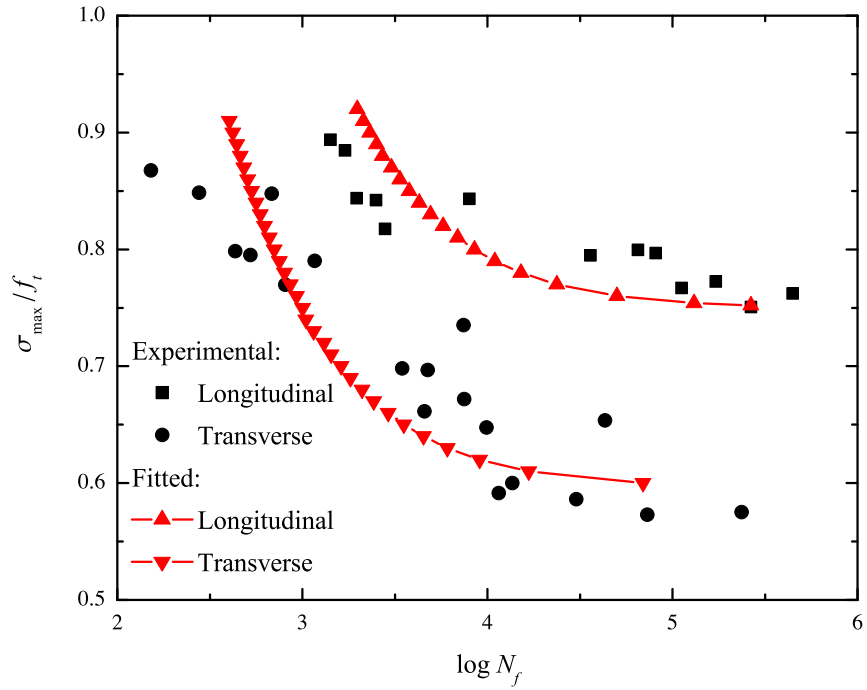
(b) Maximum strain-cycle curves for  $\sigma_{\max} = 0.7f_t$ .

Fig. 3.4. (a) S-N and (b) maximum strain-cycle curves of a concrete in tension.



(a) S-N curves.

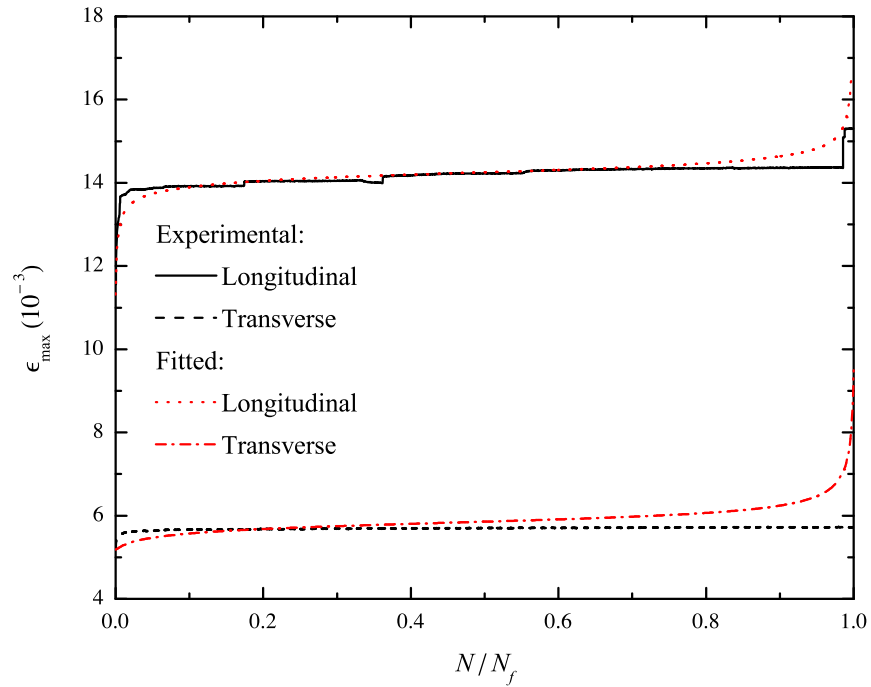
(b) Maximum strain-cycle curves for the lowest  $\sigma_{\max}$ 's.

Fig. 3.5. (a) S-N and (b) maximum strain-cycle curves of a fiber-reinforced composite in tension.

- $\chi = 0.5$  and  $j_{22}^+ = j_{33}^+ = j_{ij}^+$  ( $i \neq j$ ).

Let  $(\cdot)_{\parallel}$  denote a quantity in the longitudinal direction, and  $(\cdot)_{\perp}$  in the transverse direction. Figure 3.5 shows the experimental S–N and maximum strain–cycle curves, where  $\sigma_{\max}/f_t$  stands for either  $\sigma_{\max}/f_{t\parallel}$  in the longitudinal direction or  $\sigma_{\max}/f_{t\perp}$  in the transverse direction and so on. Especially, Figure 3.5(b) is reported for the first time. Table 3.1 lists the material parameters either experimentally measured or properly chosen for a fiber-reinforced composite. Following Ref. [123], apply a sinusoidal tensile stress ranging from 0 MPa to  $\sigma_{\max}$ , with a frequency of 5 Hz, when simulating each test. For one thing, here  $k^+$  and  $j_{22}^+ = j_{33}^+$  must be calibrated from the experimental data in both directions simultaneously. For another, Eq. (3.57) is found to serve the purpose well.  $k^+$ ,  $j_{22}^+ = j_{33}^+$ ,  $Q^+$ ,  $b$ ,  $\gamma$ , and  $n$  are then the fitted parameters.

Table 3.5.  
Predetermined parameters of a fiber-reinforced composite.

(a) Measured.			
$\tilde{E}_1$ (GPa)	$\tilde{E}_2 = \tilde{E}_3$ (GPa)	$f_{t\parallel}$ (MPa)	$f_{t\perp}$ (MPa)
150.1	8.3	2191.0	76.8

(b) Chosen.		
$\tilde{G}_{12} = \tilde{G}_{13}$ (GPa)	$\tilde{\nu}_{12} = \tilde{\nu}_{13}$	$\tilde{\nu}_{23}$
5.0	0.2	0.3

Table 3.6.  
Fitted parameters of a fiber-reinforced composite.

$k^+$ (MPa)	$j_{22}^+ = j_{33}^+$	$Q^+$ (MPa)	$b$	$\gamma$ (s <sup>-1</sup> )	$n$
15.0	49.8	76.7	1.0	$1.03 \times 10^{-3}$	1.0

Here the fitted parameters are calibrated as follows:

1. Calibrate  $k^+$  from the fatigue limit in the longitudinal direction, and set  $j_{22}^+ = j_{33}^+ = 1$ .
2. Roughly estimate  $\gamma$  and  $n$  through numerical experiments.
3. Hold  $k^+$ ,  $j_{22}^+ = j_{33}^+$ ,  $\gamma$ , and  $n$  fixed, and iteratively adjust  $Q^+$  and  $b$  till their values make the predicted maximum strain–cycle curve in the longitudinal direction the curve of best fit.
4. Hold  $Q^+$ ,  $b$ ,  $\gamma$ , and  $n$  fixed, and iteratively adjust  $k^+$  and  $j_{22}^+ = j_{33}^+$  till their values make the predicted maximum strain–cycle curves in both directions the best fits to the experimental ones.
5. Hold  $k^+$ ,  $j_{22}^+ = j_{33}^+$ ,  $Q^+$ , and  $b$  fixed, and iteratively adjust  $\gamma$  and  $n$  till their values make the predicted S–N curves in both directions the best fits to the experimental ones.

Table 3.6 lists the fitted parameters, and Figure 3.5 compares the fitted curves with the experimental data. In Figure 3.5(b), the curves in the longitudinal direction lie prominently above those in the transverse direction. This simply indicates that the ratio of the longitudinal fatigue limit to  $\tilde{E}_1$  is much greater than the ratio of the transverse fatigue limit to  $\tilde{E}_2$ . Although not very clearly shown, each curve here can be divided into three segments similarly to those in Figure 3.4(b), corresponding to three stages of fatigue failure. Especially, it also possesses the following features:

- The first segment accounts for less than 2% of the curve domain, and so does the third segment.
- $\epsilon_{\max}$  negligibly increases over the second segment.

Numerical experiments indicate that a predicted maximum strain–cycle curve possesses these features only when  $\sigma_{\max}$  is very close to the fatigue limit. Accordingly, in Figure 3.5(a), each predicted curve exhibits an asymptotic trend over a larger domain than those in Figures 3.2(a) and 3.4(a). This indicates that the experimental data

in Figure 3.5(a) are more complete for high numbers of cycles. Since  $f_{t\parallel} \gg f_{t\perp}$ , Figure 3.5(a) also indicates that the composite is much more resistant to fatigue damage in its longitudinal direction. However, even though the predicted curves plot normalized maximum stresses versus  $\log N_f$ , the curve in the longitudinal direction still lies prominently above that in the transverse direction. This most likely attributes to different failure mechanisms on the microscale, which are beyond the scope of this work. Besides, since here the predicted curve trends are similar to that in Figure 3.4(a), the corresponding discussion for Figure 3.4(a) still holds. In conclusion, the above discussion indicates that the present model can handle high-cycle anisotropic fatigue.

### 3.8 Conclusions

In this chapter, an anisotropic continuum damage model for high-cycle fatigue is developed. A viscodamage model, which can handle frequently observed brittle damage phenomena, is developed to produce stress-dependent fatigue damage evolution. The governing equation for damage evolution is derived using an incremental method. A closed-form incremental constitutive relation is derived at last.

The following findings can be obtained from the results:

- The present model is found to handle high-cycle anisotropic, tension-compression asymmetric fatigue well.
- Its closed-form incremental constitutive relation is found to facilitate the model calibration.
- It is found feasible to calibrate a continuum damage model from S–N and modulus degradation/maximum strain–cycle curves.

## 4. COHESIVE ZONE MODEL FOR QUASI-STATIC DELAMINATION

### 4.1 Basic ideas and thermodynamics

This chapter uses the same notation system as that in Chapter 5, and different from those in Chapter 2 and 3. It is beneficial to start the modeling with seeking a suitable idealization of the cohesive zone ahead of a crack tip. With the help of transmission electron microscopy, Kramer and Berger [98, 99] observed that the delamination of a polymer interface was often accompanied with the crazing ahead of the crack tip (see Figure 4.1). Specifically, a crazing process consists of the following stages:

1. as the interface is separated to a certain extent, it is incapable of sustaining the traction imposed by the adherends and becomes crazed;
2. as the deformation continues, more and more crazes nucleate, grow, coalesce with each other, causing a number of main fibrils (mostly parallel to the direction of separation) and cross-tie fibrils to form;
3. at last, main fibrils fail cohesively, and delamination occurs.

Inspired by these observations, this work hereafter idealize the cohesive zone as a fibrillated region such that each cohesive element represents a fibril (or a fibril bundle), and idealize each fibril as a deformable string that:

1. can only sustain uniaxial tension in the direction of separation [125];
2. exhibits path dependent damage behavior due to the existence of cross-tie fibrils and some other micromechanisms.

The first point implies that each cohesive element has a diagonal, constant initial elasticity tensor, say

$$\tilde{\mathbf{K}} = \tilde{K} \mathbf{I}, \quad (4.1)$$

where  $\tilde{K}$  denotes the initial elastic stiffness, and  $\mathbf{I}$  denotes the second-order identity tensor. On one hand, Hui et al. [126] pointed out that a main fibrils actually could sustain small lateral loads due to the existence of cross-tie fibrils, implying that  $\tilde{\mathbf{K}}$  might have small off-diagonal terms and even be path dependent. On the other hand, according to numerical experiments, cohesive elements (or fibrils) must be sufficiently stiff to hold the adherends together in the elastic region [69], indicating that  $\tilde{K}$  must be sufficiently large, but once this requirement is met, fine tuning  $\tilde{\mathbf{K}}$  negligibly affects numerical results. This indicates that Eq. (4.1) can serve the purpose.

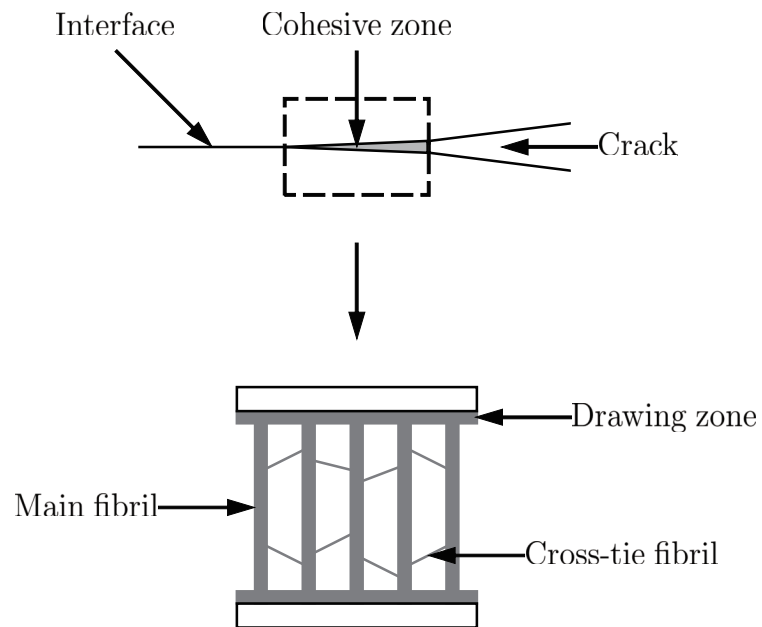


Fig. 4.1. Crazing ahead of a crack tip (adapted from Ref. [127]).

The finite element implementation of a CZM has been extensively studied (see Ref. [128], [81], and [84] for examples). Nowadays a CZM can be implemented in commercial finite element code Abaqus/Explicit via user subroutine VUMAT, for structural analysis, where:

1. Abaqus/Explicit can be used to perform quasi-static analyses with complicated contact conditions;
2. VUMAT is used to define the traction–separation relation for a cohesive element, which may undergo finite deformation [108].

Consider a cohesive element on an interface. In VUMAT, a CZM must be defined in a local corotational coordinate system, say  $\mathbf{x} = (x_1, x_2, x_3)$ , where the  $x_1$ -, the  $x_2$ -, and the  $x_3$ -directions rotate with the element. Specifically, choose the element midplane as the  $x_2x_3$  plane, the normal to the midplane as the  $x_1$ -direction, and the crack line direction as the  $x_3$ -direction (so that the delamination direction is the  $x_2$ -direction in a 2D problem, see Figure 4.2). In fact, the  $x_1$ -, the  $x_2$ -, and the  $x_3$ -directions are chosen so that they are associated with mode I, mode II, and mode III fracture, respectively. The string assumption implies that a scalar-valued damage factor, say  $d$ , can fully measure the degradation of the element. Let  $\Psi$  denote the Helmholtz free energy per unit area of the element. It can be treated as a function of a suitable set of independent state variables describing the elasticity and damage of the element, e.g.,

$$\Psi = \Psi(\boldsymbol{\gamma}, d, \alpha), \quad (4.2)$$

where  $\boldsymbol{\gamma}$  denotes the separation vector, and  $\alpha$  is a scalar describing damage accumulation. Note that a negative  $\gamma_1$  (the first component of  $\boldsymbol{\gamma}$ ) is inadmissible because it: 1. physically means that two neighboring crack faces penetrate each other; 2. should not promote damage or delamination. Hereafter set

$$\boldsymbol{\gamma} = \left[ \langle \gamma_1 \rangle \quad \gamma_2 \quad \gamma_3 \right]^T, \quad (4.3)$$

where  $\langle \cdot \rangle$  denotes the Macaulay bracket, i.e.,

$$\langle x \rangle = \begin{cases} 0 & x < 0, \\ x & x \geq 0. \end{cases} \quad (4.4)$$

Assume that  $\Psi$  can be decomposed into its elastic and damage accumulation parts as

$$\Psi(\boldsymbol{\gamma}, d, \alpha) = \Psi_e(\boldsymbol{\gamma}, d) + \Psi_d(\alpha). \quad (4.5)$$

The thermodynamic forces conjugate to the state variables are defined as

$$\boldsymbol{\tau} = \frac{\partial \Psi}{\partial \boldsymbol{\gamma}} = \frac{\partial \Psi_e}{\partial \boldsymbol{\gamma}}, \quad y = -\frac{\partial \Psi}{\partial d} = -\frac{\partial \Psi_e}{\partial d}, \quad A = \frac{\partial \Psi}{\partial \alpha} = \frac{d\Psi_d}{d\alpha}, \quad (4.6)$$

where  $\boldsymbol{\tau}$  denotes the traction vector,  $y$  denotes the damage conjugate force, and  $A$  is related to the current damage threshold.

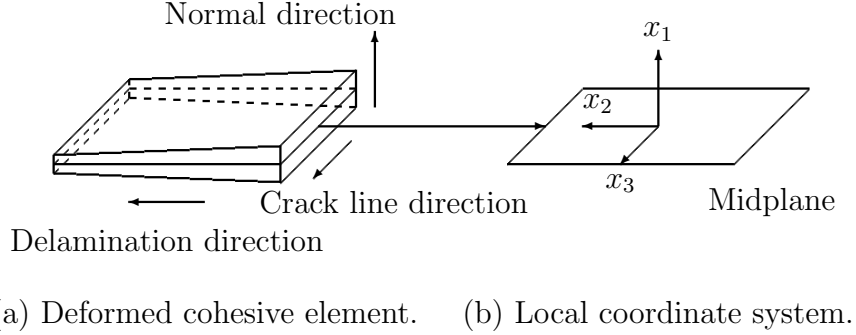


Fig. 4.2. Schematic of a deformed cohesive element.

For isothermal delamination, the Clausius–Duhem inequality can be written as

$$\Phi = \boldsymbol{\tau} \cdot \dot{\boldsymbol{\gamma}} - \dot{\Psi} \geq 0, \quad (4.7)$$

where  $\Phi$  denotes the dissipation per unit area, and the overdot denotes the time derivative of a quantity. Combining Eqs. (4.5)–(4.7) gives

$$\Phi = y\dot{d} - A\dot{\alpha} \geq 0. \quad (4.8)$$

Let  $f$  denote the damage function. Following Ref. [7], assume that the following principle of maximum dissipation applies throughout this paper: for fixed but otherwise arbitrary  $\dot{d}$  and  $\dot{\alpha}$ , the actual  $y$  and  $A$  should maximize  $\Phi$  subject to constraint  $f \leq 0$ , or mathematically speaking, should make Lagrange functional

$$L(y, A, \lambda; \dot{d}, \dot{\alpha}) = y\dot{d} - A\dot{\alpha} - \lambda f \quad (4.9)$$

attain its extremum, where  $\lambda$  is a positive Lagrange multiplier. This is the equivalent of solving associated damage evolution laws

$$\dot{d} = \lambda \frac{\partial f}{\partial y} \quad \text{and} \quad \dot{\alpha} = -\lambda \frac{\partial f}{\partial A} \quad (4.10)$$

subject to Kuhn–Tucker conditions, or loading/unloading conditions,

$$f \leq 0, \quad \dot{\lambda} \geq 0, \quad \dot{\lambda} f = 0, \quad (4.11)$$

which physically mean that damage evolution is irreversible. Last but not least, Eq. (4.10) implies that  $f$  must be a function of  $y$  and  $A$ .

In continuum damage mechanics, researchers introduced the concepts of effective space and energy equivalence to facilitate the derivation of constitutive relations. The effective space is where a fictitious, undamaged cohesive element is obtained from a real, damaged one by removing all damages so that a set of so-called effective quantities can be defined [129]. The energy equivalence hypothesis specifies the correspondence between effective quantities and quantities measurable in the real space, namely apparent quantities. Following Ref. [130], let the hypothesis follow the definition of the effective traction vector: the effective traction vector should be applied to an undamaged element such that it produces the same elastic Helmholtz free energy as those observed on a damaged element subject to the apparent traction vector, i.e.,

$$\Psi_e = \frac{1}{2} K \boldsymbol{\gamma} \cdot \boldsymbol{\gamma} = \frac{1}{2} \tilde{K} \tilde{\boldsymbol{\gamma}} \cdot \tilde{\boldsymbol{\gamma}}, \quad (4.12)$$

where  $K$  denotes the apparent elastic stiffness, and the overtilde denotes an effective quantity (e.g.,  $\tilde{K}$  denotes the effective or the initial elastic stiffness, which remains constant throughout separation). Assume that this hypothesis applies throughout this paper. Following Ref. [105], let  $\tilde{\boldsymbol{\tau}}$  be related to  $\boldsymbol{\tau}$  by

$$\tilde{\boldsymbol{\tau}} = \frac{\boldsymbol{\tau}}{1-d} \quad \text{or} \quad \boldsymbol{\tau} = (1-d) \tilde{\boldsymbol{\tau}}. \quad (4.13)$$

Hooke's law can be written as

$$\boldsymbol{\tau} = K \boldsymbol{\gamma} \quad \text{and} \quad \tilde{\boldsymbol{\tau}} = \tilde{K} \tilde{\boldsymbol{\gamma}} \quad (4.14)$$

in the apparent and the effective spaces, respectively. Combining Eqs. (4.12), (4.13), and (4.14) gives

$$\tilde{\boldsymbol{\gamma}} = (1-d) \boldsymbol{\gamma} \quad \text{or} \quad \boldsymbol{\gamma} = \frac{\tilde{\boldsymbol{\gamma}}}{1-d}. \quad (4.15)$$

Substituting Eq. (4.15) into Eq. (4.12) gives

$$K = (1-d)^2 \tilde{K}. \quad (4.16)$$

## 4.2 Damage model

Without loss of generality, suppose that a series of flexural tests, which include but are not limited to standard double cantilever beam (DCB), end-notched flexure (ENF), and MMB tests, or to say, which can produce mixed-mode I/II/III delamination, have been performed. The task is to develop a damage model:

1. whose damage parameters can be calibrated via these tests;
2. whose associated cohesive elements behave reliably and consistently when deformed along complex separation paths and can exhibit designated, possibly sophisticated mixed-mode behavior.

It is beneficial to first specify all damage parameters to be calibrated. Assume that the cohesive element obeys damage criterion

$$f = J(\hat{\gamma})y - k - A(\alpha) \leq 0, \quad (4.17)$$

where  $J$  is a scalar-valued function describing the path dependence of damage behavior,

$$\hat{\gamma} = \frac{\gamma}{\sqrt{\gamma \cdot \gamma}} \equiv \frac{\gamma}{\gamma} \quad (4.18)$$

denotes the unit vector in the direction of  $\gamma$  with  $\gamma$  denoting the magnitude of  $\gamma$ , and  $k$  denotes the initial damage threshold. A separation path is said to be nonproportional if its  $\hat{\gamma}$  varies, and it is said to involve unloading if its  $\gamma$  decreases (see Figure 4.3 for the schematics of a simple and a complex separation paths). The principle of maximum dissipation requires the damage surface to be convex (see Ref. [7] for more details). This imposes no restrictions on  $J(\hat{\gamma})$ . Recall that

$$\Psi_e = \frac{1}{2}K\gamma \cdot \gamma = \frac{1}{2}(1-d)^2\tilde{K}\gamma \cdot \gamma. \quad (4.19)$$

Substituting Eq. (4.19) into the second equation of Eq. (4.6) gives

$$y = -\frac{\partial\Psi_e}{\partial d} = (1-d)\tilde{K}\gamma \cdot \gamma. \quad (4.20)$$

Let  $y_0$  denote the value of  $y$  at damage initiation. Inspired by Ref. [131], set  $J(\mathbf{e}_1) = 1$ .

It can then be verified from Eq. (4.17) that:

1. for a test producing mode I delamination,  $k = y_0|_{\hat{\gamma}=e_1}$ ;
2. for a test during which  $\hat{\gamma} = \hat{\gamma}_i$  (where  $(\cdot)_i$  denotes the value of a quantity for the  $i$ th test),  $J(\hat{\gamma}_i) = k / \left( y_0|_{\hat{\gamma}=\hat{\gamma}_i} \right)$ .

Eqs. (4.5) and (4.6) imply that  $A$  is a function of  $\alpha$ , i.e.,  $A = A(\alpha)$ , which is referred to as the damage accumulation law.  $A(\alpha)$  must be an increasing function, indicating that additional work must be done to cause further delamination. Assume that

$$A = Q [\exp(b\alpha) - 1], \quad (4.21)$$

where  $Q$  and  $b$  are two positive damage accumulation parameters to be calibrated. Till now, all damage parameters to be calibrated have been specified.

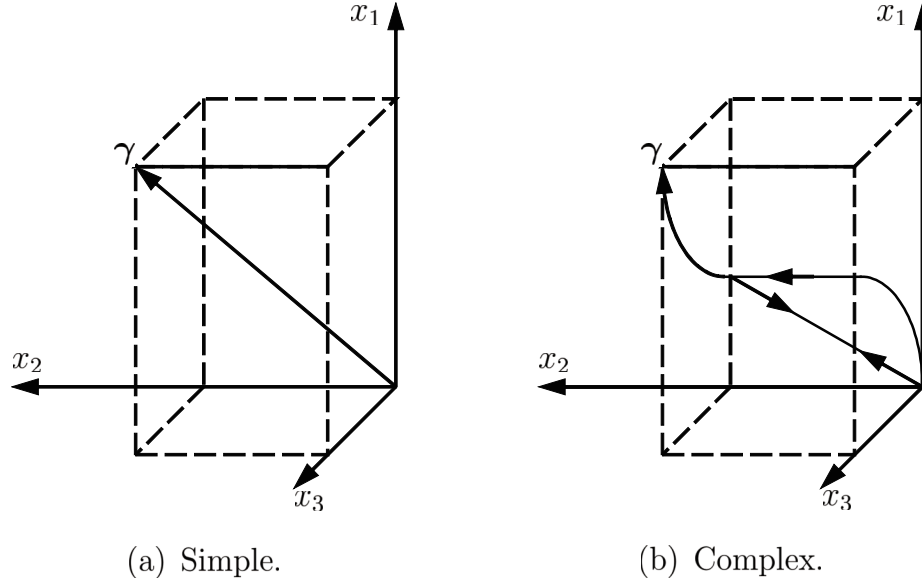


Fig. 4.3. Schematics of (a) a simple (proportional, monotonic) and (b) a complex (nonproportional, unloading–reloading) separation paths.

Substituting Eq. (4.17) into Eq. (4.10) gives

$$\dot{d} = \dot{\lambda} J \quad \text{and} \quad \dot{\alpha} = \dot{\lambda}. \quad (4.22)$$

Taking time derivatives on both sides of Eq. (4.17) gives the consistency condition as

$$\dot{f} = J\dot{y} + y \frac{\partial J}{\partial \hat{\gamma}} \cdot \dot{\hat{\gamma}} - A'(\alpha) \dot{\alpha} = 0. \quad (4.23)$$

It is beneficial to find the relationship between  $\dot{\hat{\gamma}}$  and  $\dot{\gamma}$ . Taking time derivatives on both sides of Eq. (4.18) gives

$$\dot{\hat{\gamma}} = \frac{\dot{\gamma}}{\gamma} - \frac{\dot{\gamma}}{\gamma^2} \gamma. \quad (4.24)$$

Following Ref. [131], express  $\dot{\gamma} = \partial\gamma/\partial t$  as

$$\dot{\gamma} = \frac{1}{2\gamma} \frac{\partial\gamma^2}{\partial t} = \frac{1}{2\gamma} \frac{\partial}{\partial t} (\gamma \cdot \gamma) = \frac{\gamma \cdot \dot{\gamma}}{\gamma}. \quad (4.25)$$

Substituting Eq. (4.25) into Eq. (4.24) gives

$$\dot{\hat{\gamma}} = \frac{\dot{\gamma}}{\gamma} - \frac{\gamma \cdot \dot{\gamma}}{\gamma^3} \gamma = \frac{(\gamma \cdot \gamma) \mathbf{I} - \gamma \otimes \gamma}{\gamma^3} \cdot \dot{\gamma} \equiv \mathbf{A} \cdot \dot{\gamma}. \quad (4.26)$$

Substituting Eq. (4.26) into Eq. (4.23) and rearranging the equation give

$$\dot{\alpha} = \dot{\lambda} = \frac{J\dot{y} + y \frac{\partial J}{\partial \hat{\gamma}} \cdot \mathbf{A} \cdot \dot{\gamma}}{A'(\alpha)}. \quad (4.27)$$

Substituting Eq. (4.27) into the first equation of Eq. (4.22) gives

$$\dot{d} = \frac{J^2}{A'(\alpha)} \dot{y} + \frac{Jy \frac{\partial J}{\partial \hat{\gamma}} \cdot \mathbf{A}}{A'(\alpha)} \cdot \dot{\gamma} \equiv \frac{J^2}{A'(\alpha)} \dot{y} + \mathbf{R} \cdot \dot{\gamma}, \quad (4.28)$$

which is the governing equation of damage evolution.

### 4.3 Cohesive law

It is beneficial to find the relationship between  $\dot{d}$  and  $\dot{\gamma}$ . Eq. (4.20) implies that  $y$  is a function of  $\gamma$  and  $d$ .  $\dot{y}$  can then be expressed using the chain rule as

$$\dot{y} = \frac{\partial y}{\partial \gamma} \cdot \dot{\gamma} + \frac{\partial y}{\partial d} \dot{d} = 2(1-d) \tilde{K} \gamma \cdot \dot{\gamma} - \tilde{K} \gamma \cdot \gamma \dot{d}. \quad (4.29)$$

Substituting Eq. (4.29) into Eq. (4.28) and rearranging the equation give

$$\dot{d} = \frac{\frac{2J^2(1-d)\tilde{K}}{A'(\alpha)} \gamma + \mathbf{R}}{1 + \frac{J^2 \tilde{K} \gamma \cdot \gamma}{A'(\alpha)}} \cdot \dot{\gamma} \equiv \mathbf{B} \cdot \dot{\gamma}. \quad (4.30)$$

Recall that

$$\boldsymbol{\tau} = K\boldsymbol{\gamma} \quad (4.31)$$

$$\text{and } K = (1 - d)^2 \tilde{K}. \quad (4.32)$$

Taking time derivatives on both sides of Eq. (4.31) gives

$$\dot{\boldsymbol{\tau}} = \dot{K}\boldsymbol{\gamma} + K\dot{\boldsymbol{\gamma}}. \quad (4.33)$$

The first term on the right side of Eq. (4.33) can be further expressed as

$$\dot{K} = -2(1 - d)\tilde{K}\dot{d} = -2(1 - d)\tilde{K}\mathbf{B} \cdot \dot{\boldsymbol{\gamma}}. \quad (4.34)$$

Combining Eqs. (4.33) and (4.34) gives the rate form of the cohesive law as

$$\dot{\boldsymbol{\tau}} = \dot{K}\boldsymbol{\gamma} + K\dot{\boldsymbol{\gamma}} = \left[ -2(1 - d)\tilde{K}\boldsymbol{\gamma} \otimes \mathbf{B} + K\mathbf{I} \right] \cdot \dot{\boldsymbol{\gamma}} \equiv \mathbf{L} \cdot \dot{\boldsymbol{\gamma}}. \quad (4.35)$$

where  $\mathbf{L}$  denotes the second-order continuum tangent operator.

#### 4.4 Path dependence function

$J(\hat{\boldsymbol{\gamma}})$  still awaits determination. A feasible strategy of determining  $J(\hat{\boldsymbol{\gamma}})$  involves:

1. calibrating the values of  $J(\hat{\boldsymbol{\gamma}})$  for certain values of  $\hat{\boldsymbol{\gamma}}$  from a series of flexural tests;
2. expressing  $J(\hat{\boldsymbol{\gamma}})$  in terms of these calibrated values.

Considering energy balance, the total energy release rate should equal the total work minus the elastic potential energy stored in the cohesive element [80], i.e.,

$$G = \int_0^t \boldsymbol{\tau} \cdot \dot{\boldsymbol{\gamma}} dt - \Psi_e = \int_0^t \boldsymbol{\tau} \cdot \dot{\boldsymbol{\gamma}} dt - \frac{1}{2} \boldsymbol{\tau} \cdot \boldsymbol{\gamma}, \quad (4.36)$$

where  $t$  denotes the current instant of time (see Figure 4.4 for more details on Eq. (4.36)). Recall that the  $x_1$ -, the  $x_2$ -, and the  $x_3$ -directions are chosen such that they are associated with mode I, mode II, and mode III fracture, respectively. For

notational convenience, define a column matrix  $\mathbf{G}$  containing the energy release rate in different modes,

$$\mathbf{G} = \begin{bmatrix} G_1 & G_2 & G_3 \end{bmatrix}^T = \begin{bmatrix} G_{\text{I}} & G_{\text{II}} & G_{\text{III}} \end{bmatrix}^T. \quad (4.37)$$

$G$  can be related to  $\mathbf{G}$  by

$$G = G_{\text{I}} + G_{\text{II}} + G_{\text{III}} = G_1 + G_2 + G_3. \quad (4.38)$$

Combining Eqs. (4.37) and (4.38) gives

$$\mathbf{G} = \int_0^t \boldsymbol{\tau} \cdot \boldsymbol{\mathcal{I}} \cdot \dot{\boldsymbol{\gamma}} dt - \frac{1}{2} \boldsymbol{\tau} \cdot \boldsymbol{\mathcal{I}} \cdot \boldsymbol{\gamma} \quad \text{or} \quad G_i = \int_0^t \tau_i \dot{\gamma}_i dt - \frac{1}{2} \tau_i \gamma_i \quad (\text{no summation over } i), \quad (4.39)$$

where

$$\boldsymbol{\mathcal{I}} = \sum_{i=1}^3 \mathbf{e}_i \otimes \mathbf{e}_i \otimes \mathbf{e}_i. \quad (4.40)$$

with  $\mathbf{e}_i$  denoting the  $i$ th local unit vector.

Define mode mixture array

$$\boldsymbol{\beta} = \frac{\mathbf{G}}{G}. \quad (4.41)$$

As mentioned above, Turon and his coworkers [72, 73] observed that, even in a finite element model of an MMB specimen, cohesive elements were often deformed along nonproportional separation paths, indicating that their  $\boldsymbol{\beta}$ 's might vary during a standard flexural test. Despite this fact, people often assume  $\boldsymbol{\beta}$  to be constant everywhere during a standard flexural test (or to say, assume all separation paths to be proportional) and calibrate some interface parameters (e.g.,  $J(\hat{\boldsymbol{\gamma}})$  here) from some others measured during a test (e.g.,  $G_c$ ), using a customized computer code. This is because it is difficult (partially due to high computational complexity and possible loss of convergence) to directly calibrate all interface parameters using finite element analysis, without making simplifying assumptions. The above assumption is equivalent to  $\dot{\boldsymbol{\beta}} = \mathbf{0}$ . It is beneficial to investigate how this condition restricts the deformation of an element. It is difficult to find a necessary and sufficient condition

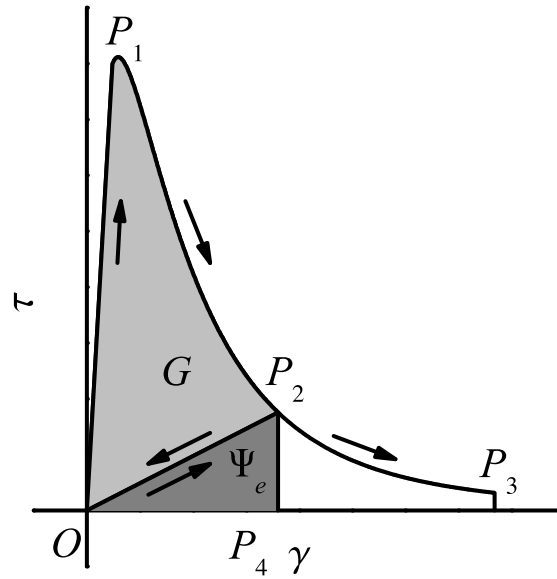


Fig. 4.4. Traction–separation curve of a cohesive element deformed along a proportional, unloading–reloading separation path. The element has been deformed along  $OP_1P_2$  till  $t$ . It can either be unloaded and reloaded along  $P_2OP_2$  or be further loaded along  $P_2P_3$ , where  $P_3$  is the failure point at time  $t_c$ . Let  $A_{(\cdot)}$  denote the area enclosed by a curve in the figure. At  $t$ ,  $G = A_{OP_1P_2O}$  and  $\Psi_e = A_{OP_2P_4O}$ ; at  $t_c$ ,  $G_c = A_{OP_1P_2P_3O}$  and  $(\Psi_e)_c \rightarrow 0$  (see Eq. (4.45)).

of  $\dot{\boldsymbol{\beta}} = \mathbf{0}$ , but it is possible to find a sufficient condition. Specifically, set  $\dot{\hat{\boldsymbol{\gamma}}} = \mathbf{0}$  everywhere. Substituting Eq. (4.14) into Eq. (4.39) and noting that  $\dot{\hat{\boldsymbol{\gamma}}} = \mathbf{0}$  give

$$G = \int_0^t K\gamma\dot{\gamma}dt - \frac{1}{2}K\gamma^2. \quad (4.42)$$

Similarly,

$$\begin{aligned} \mathbf{G} &= \int_0^t K\boldsymbol{\gamma} \cdot \boldsymbol{\mathcal{I}} \cdot \dot{\boldsymbol{\gamma}}dt - \frac{1}{2}K\boldsymbol{\gamma} \cdot \boldsymbol{\mathcal{I}} \cdot \boldsymbol{\gamma} \\ &= \left( \int_0^t K\gamma\dot{\gamma}dt - \frac{1}{2}K\gamma^2 \right) \hat{\boldsymbol{\gamma}} \cdot \boldsymbol{\mathcal{I}} \cdot \hat{\boldsymbol{\gamma}} = G \left( \sum_{i=1}^3 \hat{\gamma}_i^2 \mathbf{e}_i \right). \end{aligned} \quad (4.43)$$

Substituting Eqs. (4.42) and (4.43) into Eq. (4.41) gives

$$\boldsymbol{\beta} = \sum_{i=1}^3 \hat{\gamma}_i^2 \mathbf{e}_i \quad \text{or} \quad \dot{\boldsymbol{\beta}} = \mathbf{0}, \quad (4.44)$$

which indicates that  $\dot{\hat{\boldsymbol{\gamma}}} = \mathbf{0}$  is a sufficient condition of  $\dot{\boldsymbol{\beta}} = \mathbf{0}$ . It is more convenient to set  $\dot{\hat{\boldsymbol{\gamma}}} = \mathbf{0}$  instead of  $\dot{\boldsymbol{\beta}} = \mathbf{0}$  because:

1. setting  $\dot{\hat{\boldsymbol{\gamma}}} = \mathbf{0}$  allows one to calibrate the values of  $J(\hat{\boldsymbol{\gamma}})$  regardless the values of  $\partial J / \partial \hat{\boldsymbol{\gamma}}$  (see Eq. (4.23), where the term  $\frac{\partial J}{\partial \hat{\boldsymbol{\gamma}}} \cdot \dot{\hat{\boldsymbol{\gamma}}}$  vanishes when  $\dot{\hat{\boldsymbol{\gamma}}} = \mathbf{0}$ );
2. although  $\dot{\hat{\boldsymbol{\gamma}}} = \mathbf{0}$  is a sufficient condition of  $\dot{\boldsymbol{\beta}} = \mathbf{0}$ ,  $\dot{\boldsymbol{\beta}} = \mathbf{0}$  itself is merely a simplifying assumption.

Therefore, when calibrating the value of  $J(\hat{\boldsymbol{\gamma}})$  for a certain value of  $\hat{\boldsymbol{\gamma}}$ , assume that  $\dot{\hat{\boldsymbol{\gamma}}} = \mathbf{0}$  everywhere.

A CZM often has a delamination criterion. It is common to assume that delamination occurs when a scalar-valued damage factor, which is  $d$  here, reaches unity. Unfortunately, numerical experiments indicate that stretching a cohesive element associated with a generalized standard CZM to infinity makes its  $d$  only approach but never reach unity. For this reason, here modify the delamination criterion as: delamination occurs when  $d$  reaches a critical value close to unity, or to say, when  $d = d_c$ , where  $(\cdot)_c$  denotes the value of a quantity at the onset of delamination. With this criterion, one can uniquely determine the instant of time at the onset of delamination,

$t_c$ , and then obtain the critical total energy release rate and the critical energy release rate vector as

$$G_c = \int_0^{t_c} \boldsymbol{\tau} \cdot \dot{\boldsymbol{\gamma}} dt - (\Psi_e)_c = \int_0^{t_c} \boldsymbol{\tau} \cdot \dot{\boldsymbol{\gamma}} dt \quad \text{and} \quad \mathbf{G}_c = \int_0^{t_c} \boldsymbol{\tau} \cdot \boldsymbol{\mathcal{I}} \cdot \dot{\boldsymbol{\gamma}} dt, \quad (4.45)$$

respectively, where assuming that  $(\Psi_e)_c \rightarrow 0$  leads to the second equality in the first equation and the equality in the second equation. To this end, the real value of  $J(\hat{\boldsymbol{\gamma}})$  for a certain value of  $\hat{\boldsymbol{\gamma}}$  should make the value of  $G_c$  predicted by the present CZM have the best fit to that calibrated via a standard flexural test.

Suppose that a series of flexural tests, to which the assumption that  $\dot{\boldsymbol{\gamma}} = \mathbf{0}$  everywhere is applicable, have been performed. Also suppose that a set of  $n$  data points  $(\hat{\boldsymbol{\gamma}}_i, J_i)$  (where  $(\cdot)_i$  here denotes the  $i$ th data point) have been calibrated via these tests. The task is to construct  $J(\hat{\boldsymbol{\gamma}})$  from these data points. In the remaining of this section, abandon the Einstein summation convention unless otherwise specified—all sums are indicated by summation signs. Luo [132] proposed a class of multivariate Lagrange polynomials for multivariate interpolation. This leads one to set  $J(\hat{\boldsymbol{\gamma}})$  to be a multivariate Lagrange polynomial. For notational convenience, let  $(\cdot)^{\circ 2}$  denote the Hadamard power of a vector, e.g.,

$$\hat{\boldsymbol{\gamma}}^{\circ 2} = \sum_{i=1}^3 \hat{\gamma}_i^2 \mathbf{e}_i. \quad (4.46)$$

Following Ref. [132], introduce Lagrange basis polynomials

$$l_i(\hat{\boldsymbol{\gamma}}^{\circ 2}) = \prod_{j=1; j \neq i}^n \frac{(\hat{\boldsymbol{\gamma}}^{\circ 2} - \hat{\boldsymbol{\gamma}}_j^{\circ 2}) \cdot (\hat{\boldsymbol{\gamma}}_i^{\circ 2} - \hat{\boldsymbol{\gamma}}_j^{\circ 2})}{(\hat{\boldsymbol{\gamma}}_i^{\circ 2} - \hat{\boldsymbol{\gamma}}_j^{\circ 2}) \cdot (\hat{\boldsymbol{\gamma}}_i^{\circ 2} - \hat{\boldsymbol{\gamma}}_j^{\circ 2})} \equiv \prod_{j=1; j \neq i}^n \frac{(\hat{\boldsymbol{\gamma}}^{\circ 2} - \hat{\boldsymbol{\gamma}}_j^{\circ 2}) \cdot (\hat{\boldsymbol{\gamma}}_i^{\circ 2} - \hat{\boldsymbol{\gamma}}_j^{\circ 2})}{\|\hat{\boldsymbol{\gamma}}_i^{\circ 2} - \hat{\boldsymbol{\gamma}}_j^{\circ 2}\|^2} \quad (4.47)$$

and normalized Lagrange basis polynomials

$$\hat{l}_i(\hat{\boldsymbol{\gamma}}^{\circ 2}) = \frac{l_i(\hat{\boldsymbol{\gamma}}^{\circ 2})}{\sum_{j=1}^n l_j(\hat{\boldsymbol{\gamma}}^{\circ 2})} \equiv \frac{l_i(\hat{\boldsymbol{\gamma}}^{\circ 2})}{l(\hat{\boldsymbol{\gamma}}^{\circ 2})}, \quad (4.48)$$

and let  $J(\hat{\boldsymbol{\gamma}})$  take the form of a linear combination of these normalized Lagrange basis polynomials, i.e.,

$$J(\hat{\boldsymbol{\gamma}}) = \sum_{i=1}^n \hat{l}_i(\hat{\boldsymbol{\gamma}}^{\circ 2}) J_i. \quad (4.49)$$

It can be verified that  $\hat{l}_i(\hat{\gamma}^{\circ 2})$ 's have the following properties of Lagrange basis polynomials:

1. reproduction property and consistency;
2. linear independence;
3. delta function properties, i.e.,  $\hat{l}_i(\hat{\gamma}_j^{\circ 2}) = \delta_{ij}$ , where  $\delta_{ij}$  denotes the Dirac delta function;
4. partitions of unity property, i.e.,  $\sum_{i=1}^n \hat{l}_i(\hat{\gamma}^{\circ 2}) = 1$ .

Luo [132] numerically demonstrated that  $\hat{l}_i(\hat{\gamma}_j^{\circ 2})$ 's also have the property of linear field reproduction, i.e.,  $\sum_{i=1}^n \hat{l}_i(\hat{\gamma}^{\circ 2}) \hat{\gamma}_i^{\circ 2} = \hat{\gamma}^{\circ 2}$ . More details on multivariate interpolation can be found in Ref. [132]. In fact,  $J(\hat{\gamma})$  is defined so that, when  $\dot{\hat{\gamma}} = \mathbf{0}$ ,  $J$  can be treated as a subjective (and possibly injective) function of  $\beta$  (see Eq. (4.44)).

$\partial J / \partial \hat{\gamma}$  also awaits determination. Differentiating both sides of Eq. (4.49) with respect to  $\hat{\gamma}$  gives

$$\frac{\partial J}{\partial \hat{\gamma}} = \sum_{i=1}^n \frac{\partial \hat{l}_i}{\partial \hat{\gamma}^{\circ 2}} \cdot \frac{\partial \hat{\gamma}^{\circ 2}}{\partial \hat{\gamma}} J_i, \quad (4.50)$$

where

$$\frac{\partial \hat{\gamma}^{\circ 2}}{\partial \hat{\gamma}} = \sum_{i=1}^3 2\hat{\gamma}_i \mathbf{e}_i \otimes \mathbf{e}_i, \quad (4.51)$$

$$\text{and } \frac{\partial \hat{l}_i}{\partial \hat{\gamma}^{\circ 2}} = \frac{1}{l} \frac{\partial l_i}{\partial \hat{\gamma}^{\circ 2}} - \frac{l_i}{l^2} \frac{\partial l}{\partial \hat{\gamma}^{\circ 2}} \quad (4.52)$$

with

$$\frac{\partial \hat{l}_i}{\partial \hat{\gamma}^{\circ 2}} = \sum_{j=1; j \neq i}^n \left[ \prod_{k=1; k \neq i, j}^n \frac{(\hat{\gamma}^{\circ 2} - \hat{\gamma}_k^{\circ 2}) \cdot (\hat{\gamma}_i^{\circ 2} - \hat{\gamma}_k^{\circ 2})}{\|\hat{\gamma}_i^{\circ 2} - \hat{\gamma}_k^{\circ 2}\|^2} \right] \frac{\hat{\gamma}_i^{\circ 2} - \hat{\gamma}_j^{\circ 2}}{\|\hat{\gamma}_i^{\circ 2} - \hat{\gamma}_j^{\circ 2}\|^2} \quad (4.53)$$

$$\text{and } \frac{\partial l}{\partial \hat{\gamma}^{\circ 2}} = \sum_{i=1}^n \frac{\partial l_i}{\partial \hat{\gamma}^{\circ 2}}. \quad (4.54)$$

It is common to assume that a cohesive element exhibits a kind of transverse isotropy within the  $x_2x_3$  plane. Here the term ‘‘transverse isotropy’’ refers to the phenomenon that the element properties are the same in all directions within a plane.

In this case,  $J$  is a function of  $\hat{\gamma}_1$  only. It is then more convenient to set  $J$  to be a univariate Lagrange polynomial. Introduce Lagrange basis polynomials

$$l_i(\hat{\gamma}_1^2) = \prod_{j=1; j \neq i}^n \frac{\hat{\gamma}_1^2 - (\hat{\gamma}_1)_j^2}{(\hat{\gamma}_1)_i^2 - (\hat{\gamma}_1)_j^2}, \quad (4.55)$$

and let  $J(\hat{\gamma}_1)$  take the form of a linear combination of these Lagrange basis polynomials, i.e.,

$$J(\hat{\gamma}_1) = \sum_{i=1}^n l_i(\hat{\gamma}_1^2) J_i. \quad (4.56)$$

It can be verified that here  $l_i(\hat{\gamma}_1^2)$ 's also have the aforementioned properties of Lagrange basis polynomials.  $\partial J / \partial \hat{\gamma}$  can then be expressed as

$$\frac{\partial J}{\partial \hat{\gamma}} = \frac{\partial J}{\partial \hat{\gamma}_1} \mathbf{e}_1 = \left( \sum_{i=1}^n 2\hat{\gamma}_1 \frac{\partial l_i}{\partial \hat{\gamma}_1^2} J_i \right) \mathbf{e}_1, \quad (4.57)$$

where

$$\frac{\partial l_i}{\partial \hat{\gamma}_1^2} = \sum_{j=1; j \neq i}^n \left[ \prod_{k=1; k \neq i, j}^n \frac{\hat{\gamma}_1^2 - (\hat{\gamma}_1)_k^2}{(\hat{\gamma}_1)_i^2 - (\hat{\gamma}_1)_k^2} \right] \frac{1}{(\hat{\gamma}_1)_i^2 - (\hat{\gamma}_1)_j^2}. \quad (4.58)$$

## 4.5 Numerical examples

Reeder and Crews [75] performed a series of DCB, ENF, and MMB tests on a type of unidirectional APC-2 PEEK composite beams, measured the applied load–load point displacement curve during each test, and obtained a critical energy release rate–mode mixture ratio relationship from these curves. In this section, the interface parameters associated with the present CZM will be calibrated from these experimental data. The present CZM will then be validated through simulating these tests using Abaqus/Explicit. The effect of the interfacial strength on a load–displacement curve will also be evaluated.

### 4.5.1 Calibration of interface parameters

Assuming that a cohesive element possesses some basic features can facilitate the calibration of interface parameters. It is beneficial to start this with taking a look at

some well-established CZMs, e.g., the bilinear CZM developed by Camanho and his coworkers [69, 72, 81–83]. Specifically, a cohesive element in Ref. [69] possesses the following features:

1. the element obeys a bilinear traction–separation law;
2.  $\tilde{K}$  takes the form of Eq. (4.1) so that the element is string-like, where  $\tilde{K}$  is treated as a penalty parameter taking a very high value;
3. it exhibits transverse isotropy in the  $x_2x_3$  plane;
4. it obeys the B–K delamination criterion [133] (see Eq. (4.59) for more details) so that it can approximately exhibit designated, possibly sophisticated mixed-mode behavior.

Inspired by Ref. [69], set a present cohesive element to possess the following features:

1. the element exhibits softening right after damage initiation;
2.  $\tilde{K}$  takes a reasonable value (see Ref. [84] for example) rather than a very high value so that the element does not undergo a sudden increase in  $d$  right after damage initiation;
3. it exhibits transverse isotropy in the  $x_2x_3$  plane so that  $J(\hat{\gamma})$  takes the form of Eq. (4.56);
4. it obeys the simple delamination criterion in Section 4.4 because the specially defined  $J(\hat{\gamma})$  enables a present element to exhibit designated, possibly sophisticated mixed-mode behavior.

To endow the element with the first feature, further assume that the mode I interfacial strength,  $\tau_{I\max}$ , is 1.5% higher than the traction at mode I damage initiation,  $\tau_{I0}$ . This is because a value of 1.5% is found to balance the instant of time at the onset of softening and the “ductility” of the element well. The reason for assuming the second feature is that, unlike in Ref. [69], here  $\tilde{K}$  is a thermodynamic quantity

affecting damage evolution. Numerical experiments indicate that, if  $\tilde{K}$  takes a very high value, an element possessing the first feature may undergo a sudden increase in  $d$  (from zero to almost unity) right after damage initiation. This is neither physically realistic nor computationally favorable [134]. Table 4.1(a) lists some predetermined interface parameters, where  $\tau_{10}$  was recommended by Ref. [75],  $\tilde{K}$  and  $d_c$  are properly chosen, and  $k$  and  $\tau_{1\max}$  are thereafter calculated. Table 4.1(b) lists different combinations of  $\beta_2$  and  $G_c$  recommended by Ref. [75]. Numerical experiments indicate that damage accumulation law Eq. (4.21) serves the purpose well. The fitted parameters are therefore  $Q$ ,  $b$ , and the values of  $J$  for the values of  $\beta_2$  listed in Table 4.1(b).

Table 4.1.  
Predetermined interface parameters.

(a) Measured and assumed parameters.					
$\tilde{K}$ (N/mm <sup>3</sup> )	$\tau_{10}$ (MPa)	$k$ (J/m <sup>2</sup> )	$\tau_{1\max}$ (MPa)	$d_c$	
$3.30237 \times 10^4$	80.0	193.8	81.2	0.95	
(b) Different combinations of $\beta_2$ and $G_c$					
	DCB	20% MMB	50% MMB	80% MMB	ENF
$\beta_2$	0.0	0.2	0.5	0.8	1.0
$G_c$ (J/m <sup>2</sup> )	969	1103	1131	1376	1719

In this work, a Euler–Trapezoidal predictor–corrector method is used for time integration, and the method of nonlinear least squares is used for curve fitting (see Ref. [121] for more details). The latter method, however, is not guaranteed to converge to the global optimum and often gets “lost” if started far from the solution. Fortunately, setting the starting values close to the solution greatly improves the convergence, and such starting values can be obtained through a series of Monte Carlo experiments. The specially defined  $f$  and  $J$  allow one to calibrate the fitted parameters as follows:

1. for the DCB test, find the values of  $Q$  and  $b$  making the predicted values of  $G_{Ic}$  and  $\tau_{I\max}$  have the best fit to the predetermined ones;
2. for each of the others, hold  $Q$  and  $b$  fixed, and find the value of  $J$  making the predicted value of  $G_c$  have the best fit to that listed in Table 4.1(b).

Table 4.2 lists the fitted interface parameters. Consider two cohesive elements: one obeys the present cohesive law, and the other the bilinear cohesive law in Ref. [72]. Let the interface parameters of the latter element take the values listed in Table 4.3, where  $\tau_{II0}$  denotes the traction at mode II damage initiation, the value of  $\tilde{K}$  is set to equal that listed in Table 4.1(a) for comparison purposes, and the other values are duplicated from Ref. [69]. Also let the latter element obey the B–K criterion, i.e.,

$$G_c = G_{Ic} + (G_{IIc} - G_{Ic}) \beta_2^{2.284}, \quad (4.59)$$

where the exponent 2.284 was calibrated by Camanho and Dávila [69]. It is beneficial to investigate how these two elements behave when deformed along proportional separation paths. Figure 4.6 shows the traction–separation curves (or  $\tau$ – $\gamma$  curves) of the two elements. As expected, both elements possess their respective features. For each element:

1. all curves exhibit similar trends;
2. as the mode of delamination shifts from mode I to mode II, the curve shift upward due to an increase in  $G_c$ .

Despite similarities, two distinctions between these two sets of curves are worth noting. First, the curves predicted by the present CZM terminate at higher values of  $\gamma$ , indicating that the present element is more “ductile”. As mentioned above, stretching a cohesive element associated with a generalized standard CZM to infinity makes its  $d$  only approach but never reach unity. This kind of asymptotic behavior is actually common in continuum damage mechanics. Second, the DCB and the 20% MMB curves predicted by the bilinear CZM are very close to each other, but those predicted by the present CZM are not. This is actually because the two CZMs predict

different values of  $G_c$  for the 20% MMB test. This can be understood by looking into Figure 4.5. Last but not least, the trends of the traction–separation curves predicted by the present CZM are actually similar to those obtained using integrated digital image correlation, by Ref. [135]. This indicates that the present CZM is not only thermodynamically rigorous but also physically realistic.

Table 4.2.  
Fitted interface parameters.

(a) Fitted values of $Q$ and $b$ .					
<u><math>Q</math> (J/m<sup>2</sup>)</u>		<u><math>b</math></u>			
330.25		2.16095			
(b) Fitted values of $J$					
	DCB	20% MMB	50% MMB	80% MMB	ENF
$J$	1.0	0.951929	0.943059	0.878154	0.813075

Table 4.3.  
Interface parameters for a bilinear cohesive law.

$\tilde{K}$ (N/mm <sup>3</sup> )	$\tau_{I0}$ (MPa)	$\tau_{II0}$ (MPa)	$G_{Ic}$ (J/m <sup>2</sup> )	$G_{IIc}$ (J/m <sup>2</sup> )
$3.30237 \times 10^4$	80.0	100.0	969	1719

Figure 4.5 shows critical energy release rate–mode mixture ratio curves (or  $G_c$ – $\beta_2$  curves) predicted by different CZMs, where the curve predicted by the bilinear CZM is obtained from Eq. (4.59). Recall that Camanho and Dávila [69] calibrated the exponent in Eq. (4.59) from the experimental data points in Figure 4.5, using the method of linear least squares. The term “least squares” means that the fitted parameter should minimize the sum of the squares of the errors made in the modeling of data, which is often referred to as a merit function. A merit function provides a measure of the agreement between the fitted curve and the experimental data.

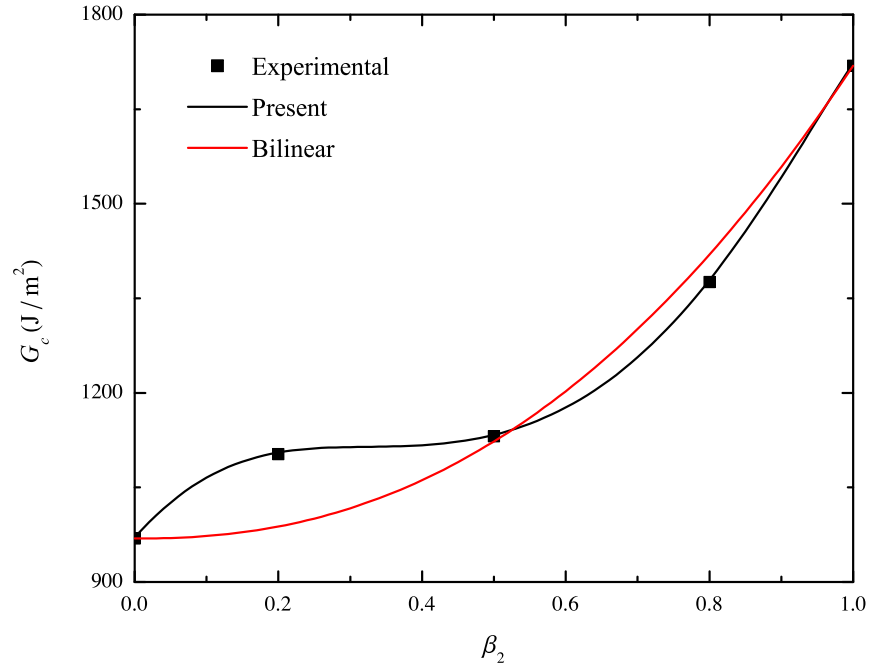


Fig. 4.5. Critical energy release rate–mode mixture ratio curves predicted by different CZMs.

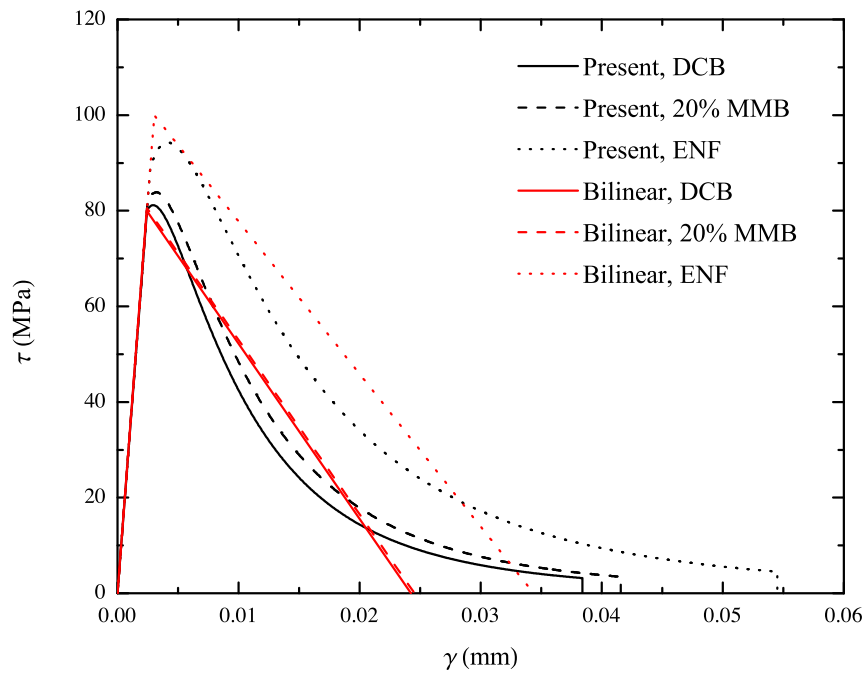


Fig. 4.6. Traction–separation curves predicted by different CZMs.

The smaller its value the better fitting. Numerical experiments indicate that  $J(\hat{\gamma})$  directly leads to the curve predicted by the present CZM. On one hand, the curve due to  $J(\hat{\gamma})$  goes through all experimental data points and therefore produces a zero merit function. It can be expected that, if more data points were incorporated, the same observation would be made due to the characteristics of Lagrange polynomial  $J(\hat{\gamma})$ . Note that a greater number of data points lead to higher accuracy. All these imply that here  $J(\hat{\gamma})$  makes the accuracy increase with increasing number of data points. On the other hand, the curve due to Eq. (4.59) produces a merit function of 0.121. Especially, at  $\beta_2 = 0.2$ , this curve noticeably deviates from the experimental data. It can also be expected that, if more data points were incorporated, this value would more or less increase because the chosen form of  $G_c$  in Eq. (4.59) imposes strong restrictions on the trend of a predicted  $G_c-\beta_2$  curve. All these at least imply that here Eq. (4.59) does not necessarily make the accuracy increase with increasing number of data points. In summary, the specially defined  $J(\hat{\gamma})$  endows the present CZM with the following advantageous features:

1. the present CZM can produce a good estimate of the critical energy release rate–mode mixture ratio relationship based on available experimental data;
2. its accuracy increases with increasing number of data points;
3. a user no longer needs to carefully choose the expression for  $G_c$  in a delamination criterion when encountering a set of irregularly distributed data points;
4. the values of  $J(\hat{\gamma})$  and  $\partial J/\partial \hat{\gamma}$  can be conveniently computed.

#### 4.5.2 Validation examples

In this section, the present CZM will be validated through simulating the series of flexural tests performed by Reeder and Crews [75]. Figure 4.7 depicts the experimental settings of the DCB, the ENF, and the MMB tests. Each laminate had a span length ( $L$ ) of 102 mm, a width ( $b$ ) of 25.4 mm, and a thickness ( $h$ ) of 1.56 mm.

Table 4.4 lists the elastic constants of each laminate, the initial delamination length ( $a_0$ ), and the lever length ( $c$ ) during each test. More details on experimental settings can be found in Ref. [75].

Table 4.4.  
Experimental parameters.

(a) Elastic constants of each laminate.					
$E_1$ (GPa)	$E_2 = E_3$ (GPa)	$G_{12} = G_{13}$ (GPa)	$G_{23}$ (GPa)	$\nu_{12} = \nu_{13}$	$\nu_{23}$
122.7	10.1	5.5	3.7	0.25	0.45
(b) Initial delamination lengths and lever lengths.					
	DCB	20% MMB	50% MMB	80% MMB	ENF
$a_0$ (mm)	32.9	33.7	34.1	31.4	39.3
$c$ (mm)	–	97.4	42.2	27.6	–

Several authors [70,81,83,136–138] used 3D finite element models of the specimens in their simulations but obtained some oscillatory load–displacement curves. This is because a very complex finite element model often leads to a low convergence rate and low accuracy. Several authors attempted to simplify such 3D finite element models. Noting that the laminate thickness was much smaller than the span length, several authors [69, 134, 139] idealized each laminate as a plate. Despite success, a plate theory tends to oversimplify the stress distribution over the thickness direction of each laminate. This is because, even though the laminate thickness is small, it is still non-negligible with respect to the cohesive elements. Noting that each laminate was unconstrained in its width direction on the interval of interest, several authors [72, 138, 140] idealized each laminate as a beam with a negligible width and assumed that plane stress conditions prevailed over each planar beam. Numerical results indicate that this model can well capture the stress perturbations around the interface crack tip. For these reasons, hereafter idealize each laminate as a 2D beam under plane stress conditions.

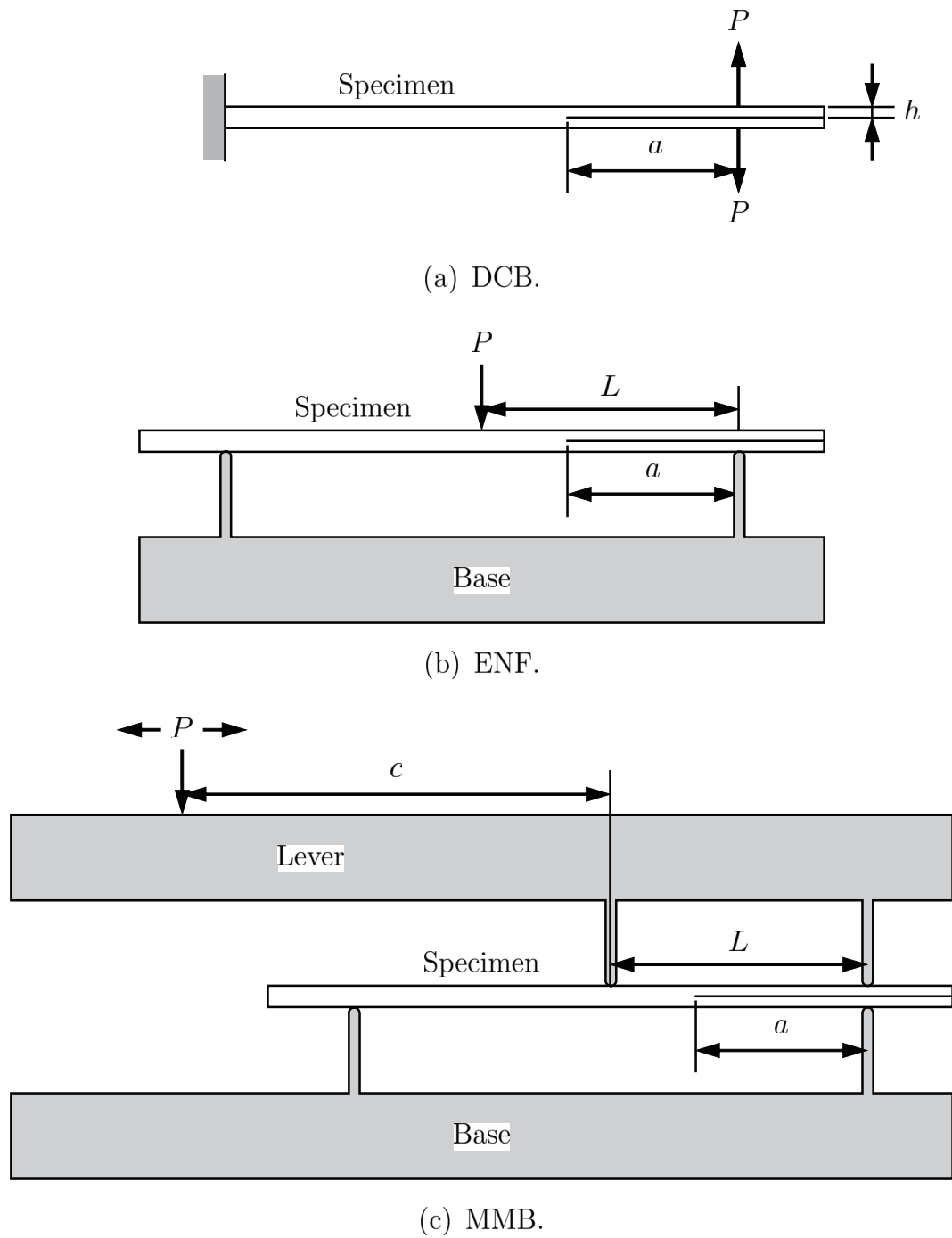


Fig. 4.7. Experimental settings.

Here Abaqus/Explicit is used to simulate the tests, and the present CZM is implemented in Abaqus/Explicit via VUMAT. Figure 4.8 shows a sample finite element model of an MMB specimen (see Ref. [139] for finite element models with similar loading levers). Each 2D finite element model consists of two planar beam sections and an interface bonding these two sections. Both beam sections are meshed with 4-node quadrilateral elements having 2 degrees of freedom (DOFs) at each node (CPS4), and each meshed beam section consists of  $510 \times 6$  elements (each element measures  $0.2 \text{ mm} \times 0.26 \text{ mm}$ ). The interface is meshed with one layer of 510 4-node quadrilateral elements having 2 integration points (COH2D4) (each element is  $0.2 \text{ mm}$  long), and each element is set to obey the present cohesive law. When using an explicit time integration scheme, one must properly choose some controlling parameters (e.g., the mass scaling factor, the load rate, and the viscosity parameters) to achieve a balance between accuracy and efficiency. More details on how these controlling parameters were chosen can be found in Ref. [138]. All cohesive zones are found to be well resolved, and all finite element models are found to be capable of producing converged results.

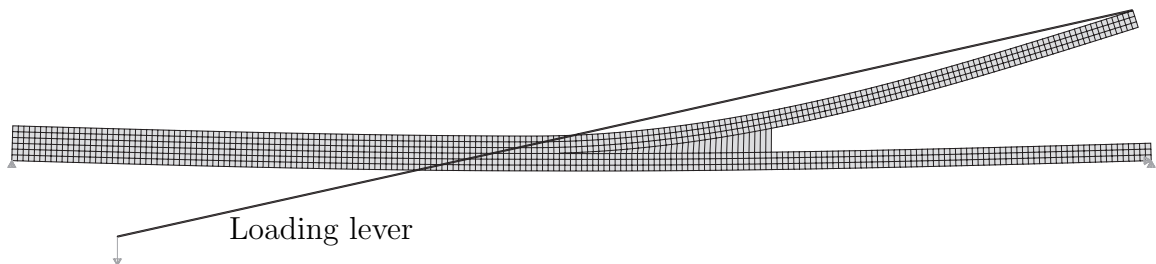


Fig. 4.8. Sample finite element model of an MMB specimen.

Figure 4.9 shows the load–displacement curves predicted by different CZMs. A Savitzky–Golay filter is used to eliminate the noise on the ENF curve predicted by the present CZM (see Ref. [121] for more details). It can be seen that both sets of predicted curves agree well with the experimental curves in the linear region but more or less deviate from the experimental curves in the nonlinear region. For the DCB test, the two predicted curves are in good agreement but both lie below the experimental

curve in the nonlinear region. One possible reason for this is that the value of  $G_{Ic}$  listed in Table 4.1(b) is underestimated. For the 20% and the 80% MMB tests, the curves predicted by the present CZM agree well with the experimental curves, while the curves predicted by the bilinear CZM suggest underestimated maximum applied loads. One possible reason for the underestimation of the 20% MMB maximum applied load predicted by the bilinear CZM is that the bilinear CZM underestimates  $G_c$  at  $\beta_2 = 0.2$  (see Figure 4.5). For the 50% MMB test, the curve predicted by the present CZM suggests an overestimated maximum applied load. The reason for this will be investigated in detail later this section. For the ENF test, both of the predicted curves slightly deviate from the experimental curve in the nonlinear region. The curve predicted by the present CZM also suggests that the ENF test can be unstable. This actually agrees with experimental observations [141,142]. In summary, the predictions by the present CZM are at least as accurate as (sometimes more accurate than) those by the bilinear CZM except for the 50% MMB test. There is a need for taking a look at more results regarding the 50% MMB test.

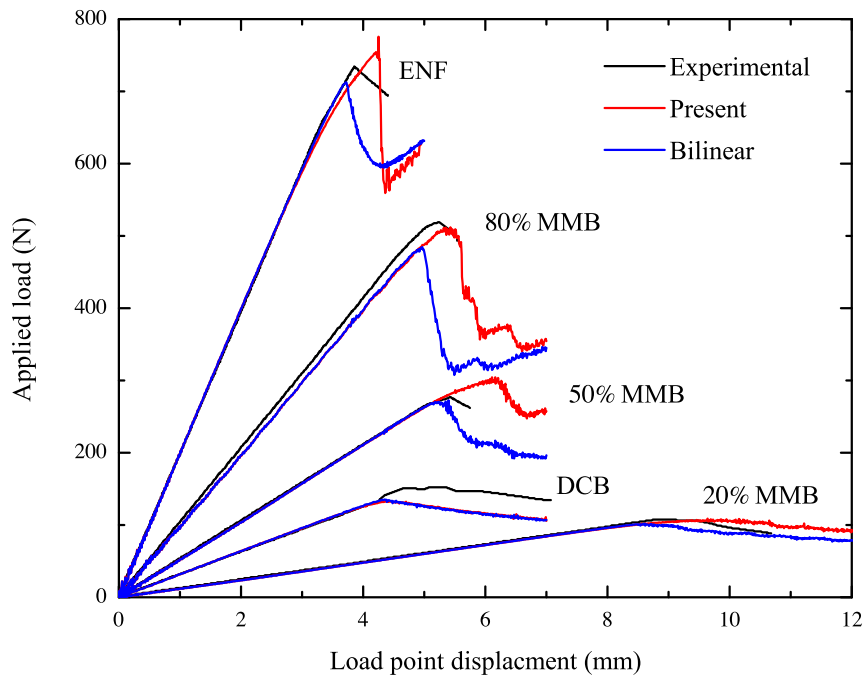


Fig. 4.9. Applied load–load point displacement curves predicted by different CZMs.

As mentioned above, Turon and his coworkers [72, 73] observed that, even in a finite element model of an MMB specimen, cohesive elements were often deformed along nonproportional separation paths. This leads one to look into the deformation processes of some cohesive elements during each test. Numerical experiments indicate that the deformation process of the rightmost cohesive element during each test is very representative. Let  $\theta = \tan^{-1}(\gamma_2/\gamma_1)$  denote the angle of inclination of a cohesive element (or specifically, the angle between the current direction of the element and the  $x_1$ -direction). In a 2D problem, a separation path is said to be proportional if its  $\theta$  always remains constant. Figure 4.10 shows the variation in the orientation of the rightmost cohesive element during each test, and Table 4.5 listed the corresponding value of  $G_c$  from each test. In Figure 4.10, neglecting the oscillations due to the use of an explicit time integration scheme, each predicted curve for an MMB test lies above its corresponding recommended curve in the linear region and exhibits a decreasing trend in the nonlinear region, indicating that the separation path is nonproportional. Accordingly, in Table 4.5, the value of  $G_c$  from each test more or less deviates its corresponding recommended value. All these again verify the observation made by Turon and his coworkers [72, 73].

Table 4.5.  
 $G_c$  (J/m<sup>2</sup>) of the rightmost cohesive element from each test.

	DCB	20% MMB	50% MMB	80% MMB	ENF
Table 4.1(b)	969	1103	1131	1376	1719
Present	958.228	964.996	1132.08	1271.87	1875.53
Bilinear	968.623	989.460	1048.76	1256.37	1804.62

It is beneficial to take a look at more results regarding the 50% MMB test. Consider the rightmost five cohesive elements in the finite element model of the 50% MMB specimen, and number them in ascending order from right to left (so that the rightmost element is Element 1). Figure 4.11 shows the variations in the orientations of the

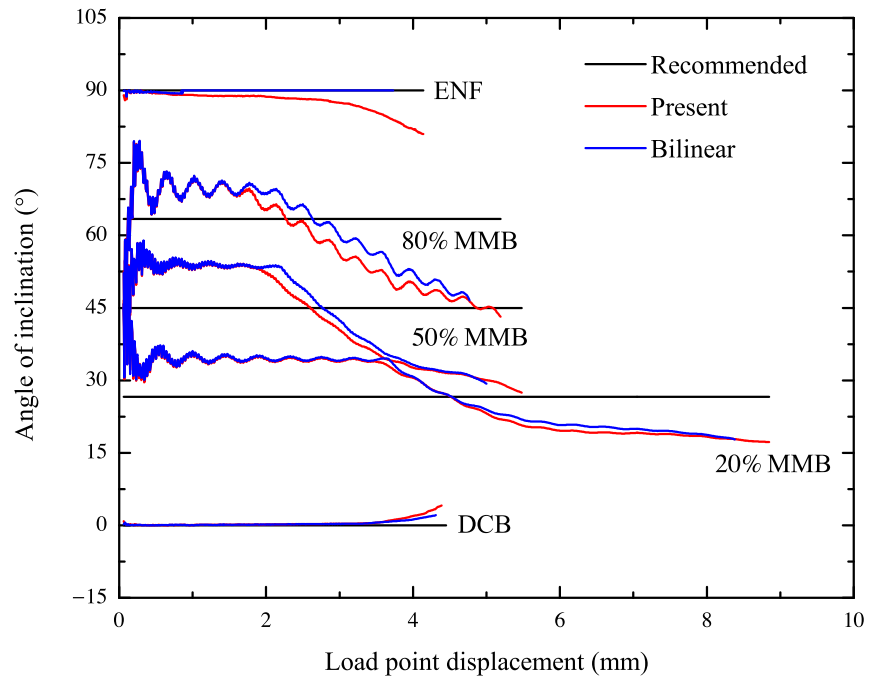


Fig. 4.10. Variation in the orientation of the rightmost cohesive element during each test.

rightmost five cohesive elements during the 50% MMB test, and Table 4.6 listed the corresponding values of  $G_c$  from this test. Similarly to Figure 4.10, here each predicted curve lies above the recommended curve in the linear region and exhibits a decreasing trend in the nonlinear region. Moreover, as the element number increases, the predicted curve shifts upward. All these indicate that  $G_c$  can be location-dependent during a single test. This can be understood by looking into the local fields (e.g., stress and strain fields) around the interface crack tip. Specifically, as the interface crack propagates leftward:

1. the delamination length ( $a$  in Figure 4.7) keeps increasing, while the span length ( $L$ ) and the lever length ( $c$ ) remain unchanged;
2. the deformation of each cohesive element is continuously affected by that of its neighboring elements.

The first point causes the local fields location-dependent even at the structural level, and the second point causes the local fields more complex on the microscopic scale. Accordingly, in Table 4.6, for each CZM, the value of  $G_c$  increases with increasing element number. Despite this similarity, the two CZMs actually produce very different values of  $G_c$ . In Figure 4.11, the separation path of Element 1 is closest to the recommended one. In Table 4.6, Element 1 obeying the present cohesive law has a  $G_c$  0.0955% higher than the recommended one, while Element 1 obeying the bilinear cohesive law has a  $G_c$  7.27% lower than the recommended one. Recall that, in Figure 4.9, the curve predicted by the present CZM suggests an overestimated maximum applied load. To this end, it turns out that:

1. the recommended value of  $G_c$  for  $\beta_2 = 0.5$  may be overestimated;
2. given the recommended values of  $G_c$ , the bilinear CZM may underestimate  $G_c$  when a cohesive element is deformed along a nonproportional separation path around  $\beta_2 = 0.5$ .

There are two possible reasons for the second point. First, the bilinear CZM may underestimate  $G_c$  on the interval of  $0 < \beta_2 < 0.5$  (see Figure 4.5). Second, a non-generalized standard CZM may insufficiently regularize damage evolution along non-proportional separation path, overestimate/underestimate the rate of damage evolution, and therefore underestimate/overestimate  $G_c$ . In summary, all the results in this section indicate that the present CZM can produce reliable simulation results.

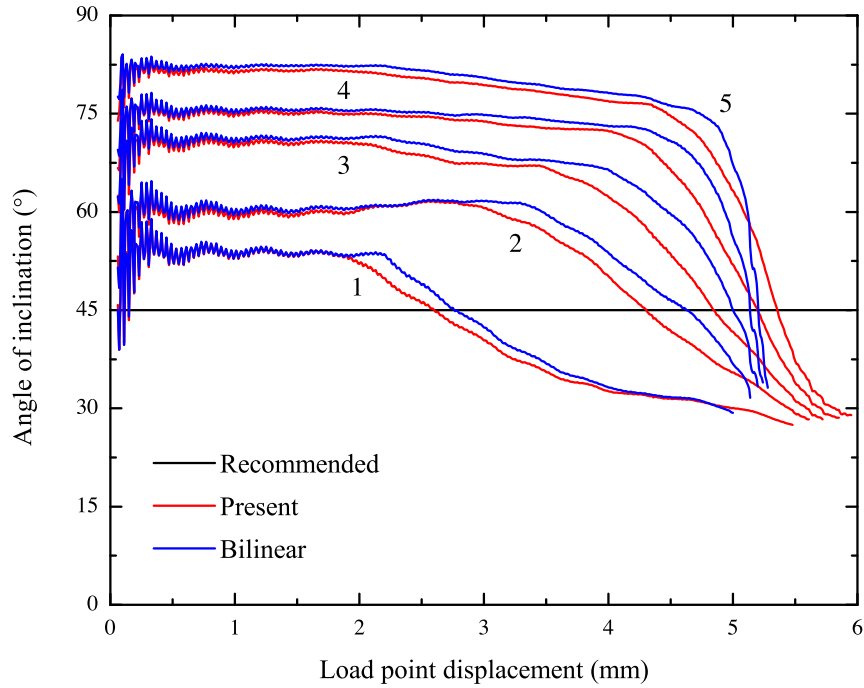


Fig. 4.11. Variations in the orientations of the rightmost five cohesive elements during the 50% MMB test.

Table 4.6.

$G_c$ 's ( $\text{J/m}^2$ ) of the rightmost five cohesive elements from the 50% MMB test.

	1	2	3	4	5
Table 4.1(b)	1131	1131	1131	1131	1131
Present	1132.08	1171.71	1216.52	1281.81	1319.13
Bilinear	1048.76	1111.14	1120.33	1135.64	1154.48

### 4.5.3 Parametric study

It is well known that  $G_c$  affects the load–displacement curves from the DCB, the ENF, and the MMB tests. Several authors [72, 73, 140] found that, once a CZM was introduced, the interfacial strength also affected these curves. In this section, the effect of the interfacial strength on a load–displacement curve will be evaluated.

Consider three cohesive elements with different mode I interfacial strengths ( $\tau_{I\max}$ 's, see Table 4.7(a)). For each element, set  $\tilde{K}$ ,  $k$ , and  $d_c$  to take the values listed in Table 4.7(a), and set  $G_c$  to take the values listed in Table 4.1(b). The fitted parameters,  $Q$ ,  $b$ , and the values of  $J$  during all tests, can then be calibrated similarly to Section 4.5.1. Tables 4.7(b) and 4.7(c) list the fitted values. In fact, the predetermined parameters are set so that the fitted parameters of the three elements are close.

Figure 4.12 shows the mode I  $\tau$ – $\gamma$  curves for different values of  $\tau_{I\max}$ . As expected, all curves exhibit similar trends, but as  $\tau_{I\max}$  increases, the element becomes stronger but less “ductile”. Figure 4.13 shows the  $G_c$ – $\beta_2$  curves for different values of  $\tau_{I\max}$ . It can be seen that all three curves coincide. All these indicate that the present CZM allows a user to customize the interfacial strength and the critical energy release rate–mode mixture ratio relationship separately.

Figure 4.14 shows the load–displacement curves for different values of  $\tau_{I\max}$ . A Savitzky–Golay filter is used to eliminate the noise on the predicted ENF curves. On one hand, a lower interfacial strength leads to a flatter traction-separation curve and a larger cohesive zone; on the other hand, it makes a cohesive element more vulnerable to traction and capable of sustaining a lower maximum traction. These two mechanisms compete with each other during progressive delamination. For each test in Figure 4.14, as  $\tau_{I\max}$  decreases, the predicted curve becomes nonlinear earlier and suggests a lower maximum applied load. This indicates that, for the present experimental settings, the latter mechanism overwhelms the former one during each test. The cohesive elements therefore behave like a thin layer of dampers smoothing the load-displacement curves (e.g., preventing a sudden load drop). The lower

Table 4.7.  
Interface parameters in three cases.

(a) Predetermined parameters.					
	$\tilde{K}$ (N/mm <sup>3</sup> )	$\tau_{I0}$ (MPa)	$k$ (J/m <sup>2</sup> )	$\tau_{I\max}$ (MPa)	$d_c$
1	$1.65119 \times 10^4$	56.5685	193.8	57.4171	0.95
2	$3.30237 \times 10^4$	80.0	193.8	81.2	0.95
3	$6.60475 \times 10^4$	113.137	193.8	114.834	0.95

(b) Fitted values of $Q$ and $b$ .		
	$Q$ (J/m <sup>2</sup> )	$b$
1	332.899	2.15215
2	330.25	2.16095
3	332.899	2.15215

(c) Fitted values of $J$					
	DCB	20% MMB	50% MMB	80% MMB	ENF
1	1.0	0.951837	0.942953	0.877948	0.812458
2	1.0	0.951929	0.943059	0.878154	0.813075
3	1.0	0.951835	0.942951	0.877944	0.812762

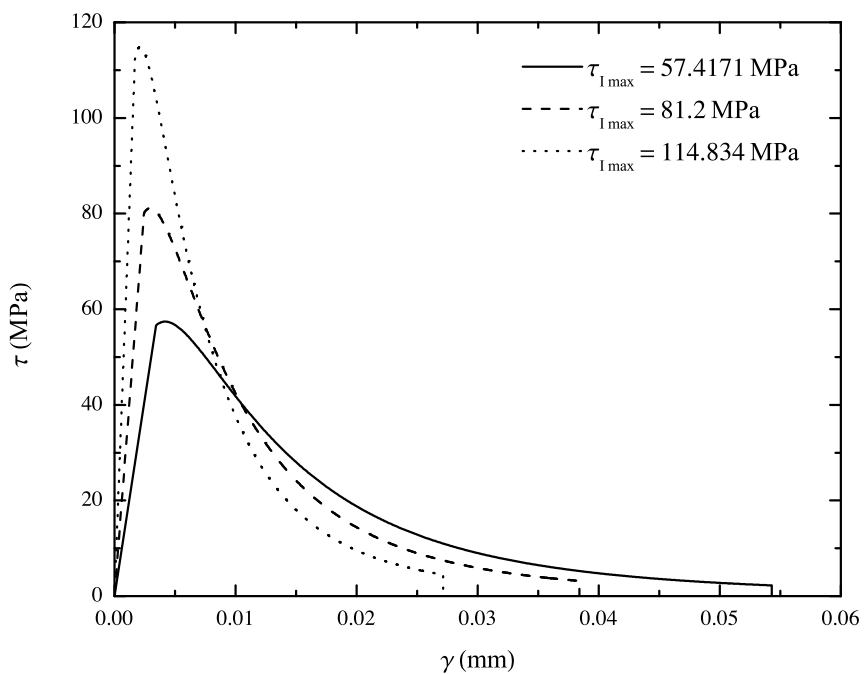


Fig. 4.12. Mode I traction–separation curves for different interfacial strengths.

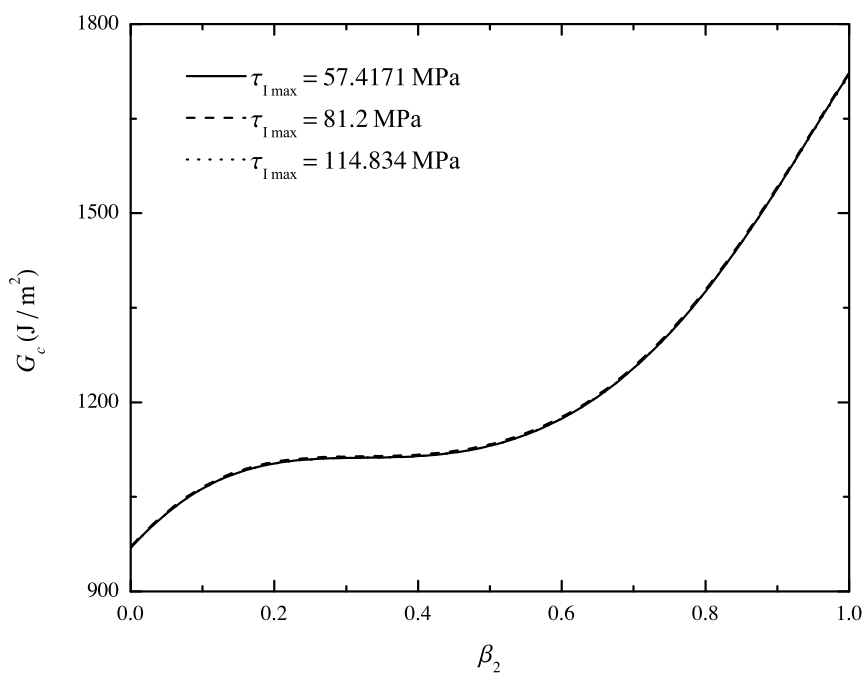
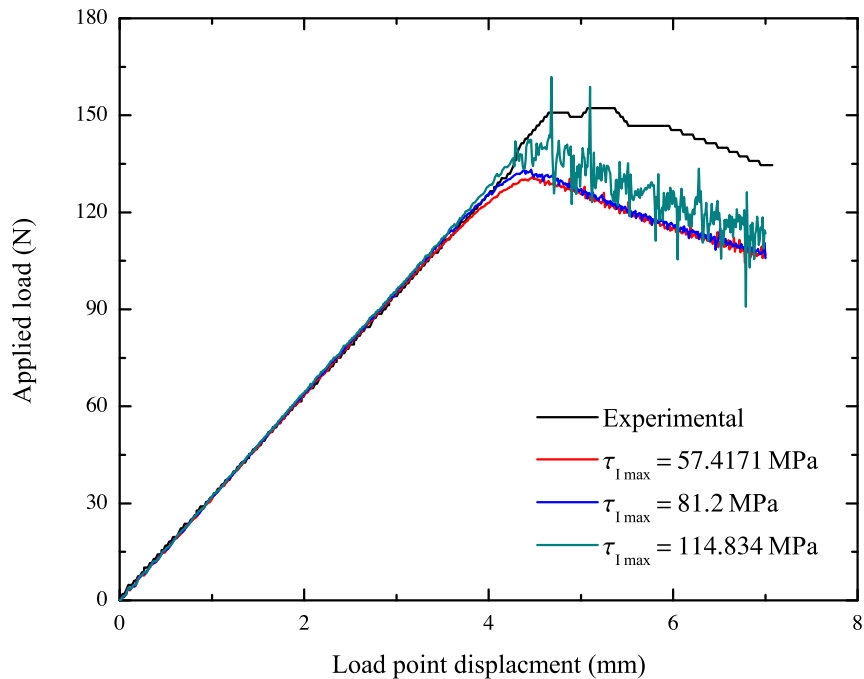


Fig. 4.13. Critical energy release rate–mixed-mode ratio curves for different interfacial strengths.

interfacial strength the more flexible dampers. All these agree with the findings in Refs. [140], [72], and [73]. Meanwhile, the curves for  $\tau_{I\max} = 114.834\text{MPa}$  more or less oscillate in the nonlinear region. This implies that an artificially high interfacial strength can reduce the stability of the numerical analysis, leading one to adjust some chosen controlling parameters in Abaqus/Explicit. However, for comparison purposes, all controlling parameters are held fixed throughout this section. In fact, similar oscillations can be found in Refs. [136], [140], [70], [137], [83], and [138].

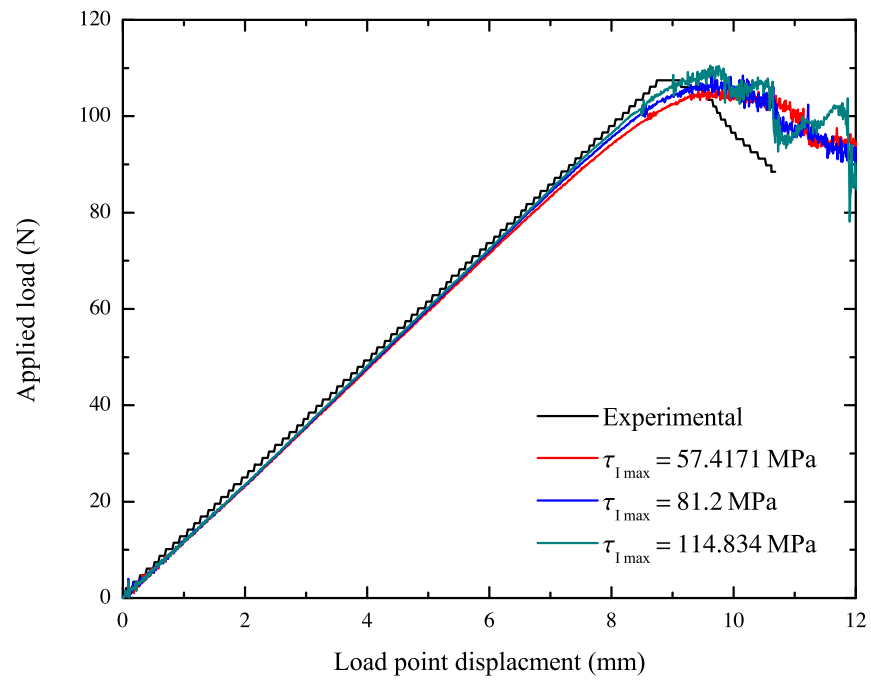


(a) DCB.

Fig. 4.14. Applied load–load point displacement curves for different interfacial strengths.

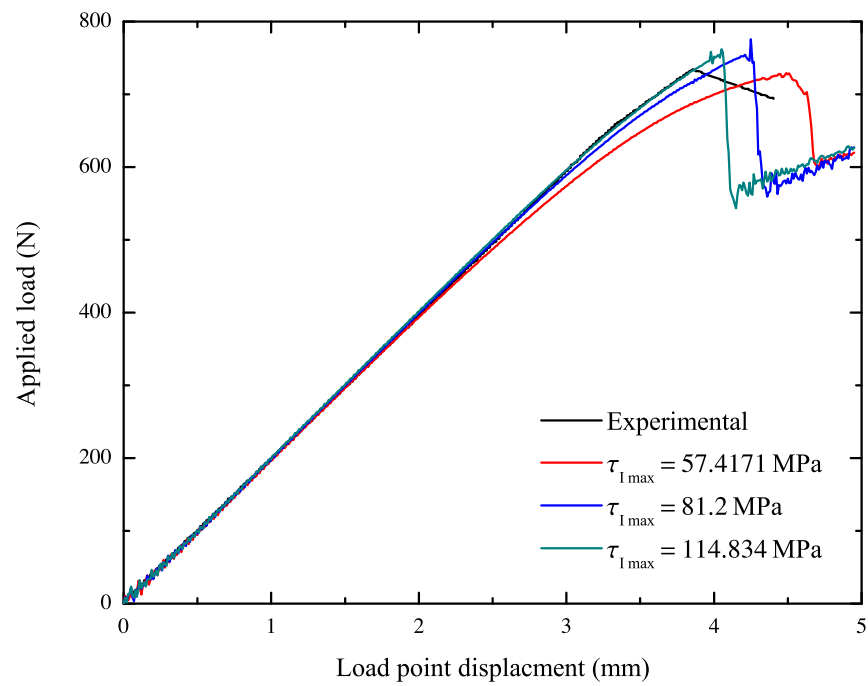
#### 4.5.4 Conclusions

In this chapter, a string-based CZM for interlaminar delamination is developed such that its associated cohesive elements (1) behave reliably and consistently when deformed along complex separation paths and (2) can display experimental critical



(b) 20% MMB.

Fig. 4.14. Applied load–load point displacement curves for different interfacial strengths (continued).



(c) ENF.

Fig. 4.14. Applied load–load point displacement curves for different interfacial strengths (continued).

energy release rate–mode mixture ratio relationships. To endow the present CZM with the first feature, the thermodynamic equations are formulated in a generalized standard manner. To resolve a dilemma encountered when developing generalized standard CZMs, each cohesive element is idealized as a deformable string exhibiting path-dependent damage behavior. To endow the present CZM with the second feature, a damage model having a path dependence function is developed, and the path dependence function is constructed such that each cohesive element can exhibit designated, possibly sophisticated mixed-mode behavior. The rate form of the cohesive law is subsequently derived.

The following findings can be obtained from the results:

- The present CZM is found to be capable of producing physically realistic traction–separation curves and good estimates of the critical energy release rate–mode mixture ratio relationships.
- It is found to be capable of producing reliable simulation results.
- It is found to allow a user to customize the interfacial strength and the critical energy release rate–mode mixture ratio relationship separately.

## 5. COHESIVE ZONE MODEL FOR FATIGUE DELAMINATION

### 5.1 String-based CZM

This chapter uses the same notation system as that in Chapter 4, and different from those in Chapter 2 and 3. Recall the Helmholtz free energy and state variable definition from Eqs. (4.2) to (4.6). For isothermal deformation, the Clausius–Duhem inequality takes the same form as before:

$$\Phi = y\dot{d} - A\dot{\alpha} \geq 0. \quad (5.1)$$

where  $\Phi$  denotes the dissipation per unit area, and the overdot denotes the time derivative of a quantity. say  $\Omega$ , governing the evolution of  $d$  and  $\alpha$ , such that [20]

$$\dot{d} = \frac{\partial \Omega}{\partial y} \quad \text{and} \quad \dot{\alpha} = -\frac{\partial \Omega}{\partial A}. \quad (5.2)$$

Further assume that  $\Omega$  depends on  $y$  and  $A$  via a damage function,  $f$ , such that

$$\Omega = \Omega(f) \quad \text{and} \quad \dot{v} = \frac{\partial \Omega}{\partial f}, \quad (5.3)$$

where  $\dot{v}$  is referred to as the viscosity function. Choosing a viscodamage model is then the equivalence of choosing  $f$  and  $\dot{v}$ . Combining Eqs. (5.2) and (5.3) gives the damage evolution laws as

$$\dot{d} = \dot{v} \frac{\partial f}{\partial y} \quad \text{and} \quad \dot{\alpha} = -\dot{v} \frac{\partial f}{\partial A}. \quad (5.4)$$

According to Ref. [20],  $\Omega$  has to be a convex function of  $y$  and  $A$ , and so does  $f$ . With the effective space concept and the energy equivalence hypothesis, Eqs. (4.12) to (4.16) still stand.

The damage model characterizes the mixed-mode behavior of the element. Its associated parameters ought to be calibrated via a series of flexural tests. Let the

damage function follows the same form as in Eq. (4.17), and the damage accumulation law follows the same form as in Eq. (4.21). Combing Eqs. (5.4) and (4.17) gives

$$\dot{d} = \dot{\nu}J \quad \text{and} \quad \dot{\alpha} = \dot{\nu}. \quad (5.5)$$

Similarly to a continuum damage model, the present CZM leads its associated cohesive elements to exhibit asymptotic behavior when stretched infinitely (i.e., their  $d$ 's approach but never attain unity). The following delamination criterion is therefore necessary: a cohesive element is considered failed once its  $d$  attains  $d_c$ , a value close to unity. Last let the viscosity function,  $\dot{\nu}$ , take a similar form to the Perzyna model in viscoplasticity [120], i.e.,

$$\dot{\nu} = \begin{cases} \frac{1}{\eta} \left( \frac{f}{k+A} \right)^n & f \geq 0, \\ 0 & f < 0. \end{cases} \quad (5.6)$$

where  $\eta$  and  $n$  are two parameters describing viscosity.

## 5.2 Implicit integration scheme

The present CZM can be implemented in implicit solver Abaqus/Standard via user subroutine UMAT, for structural analysis. UMAT (1) allows users to create customized cohesive laws and (2) can use and update any state variables, either passed in or stored elsewhere [108]. Consider time interval  $[t_n, t_{n+1}]$ . Let  $(\cdot)_n$  denote a quantity at  $t_n$ , and let  $\Delta(\cdot) = (\cdot)_{n+1} - (\cdot)_n$ . When calling UMAT at an integration point, Abaqus/Standard passes in  $\boldsymbol{\tau}_n$ ,  $\boldsymbol{\gamma}_n$  and  $\Delta\boldsymbol{\gamma}$  and gets back  $\boldsymbol{\tau}_{n+1}$  and the consistent Jacobian,  $\partial\Delta\boldsymbol{\tau}/\partial\Delta\boldsymbol{\gamma}$ . Given all variables at  $t_n$ , along with  $\Delta\boldsymbol{\gamma}$ , the implicit integration scheme should update the other variables and return the consistent Jacobian.

Hereafter omit the subscript  $n+1$  on each quantity at  $t_{n+1}$ . The integration scheme can be formulated as solving the following equation set for  $y$  and  $\Delta\alpha$ :

$$y = (1-d)\tilde{K}\boldsymbol{\gamma} \cdot \boldsymbol{\gamma}, \quad (5.7)$$

$$\Delta\alpha = \dot{\nu}\Delta t. \quad (5.7')$$

By definition,

$$d = d_n + \Delta d \quad \text{and} \quad \alpha = \alpha_n + \Delta\alpha. \quad (5.8)$$

Eq. (5.5) can be rewritten as

$$\Delta d = J(\hat{\gamma}) \Delta v = J(\hat{\gamma}) \Delta\alpha. \quad (5.9)$$

When updating the variables,  $\gamma$  is held fixed. Eqs. (5.8) and (5.9) indicate that  $d$  and  $\alpha$  are functions of  $\Delta\alpha$  here. The task can then be reformulated as solving the following equation set for  $y$  and  $\Delta\alpha$ :

$$\Psi(y, \Delta\alpha) = y - (1 - d) \tilde{K} \gamma \cdot \gamma = 0, \quad (5.10)$$

$$A(y, \Delta\alpha) = \Delta\alpha - \dot{v} \Delta t = 0. \quad (5.11)$$

Eqs. (5.10) and (5.11) can be solved using the Newton–Raphson method. Require

$$\Psi(y_{\text{old}} + dy, \Delta\alpha_{\text{old}} + d\Delta\alpha) = \Psi(y_{\text{old}}, \Delta\alpha_{\text{old}}) + \frac{\partial\Psi}{\partial y} dy + \frac{\partial\Psi}{\partial\Delta\alpha} d\Delta\alpha = 0, \quad (5.12)$$

$$A(y_{\text{old}} + dy, \Delta\alpha_{\text{old}} + d\Delta\alpha) = A(y_{\text{old}}, \Delta\alpha_{\text{old}}) + \frac{\partial A}{\partial y} dy + \frac{\partial A}{\partial\Delta\alpha} d\Delta\alpha = 0. \quad (5.12')$$

(see 5.3 for more details on the partial derivatives in Eqs. (5.12)). Eq. (5.12) can be written in matrix form as

$$\begin{Bmatrix} \Psi(y_{\text{old}}, \Delta\alpha_{\text{old}}) \\ \kappa A(y_{\text{old}}, \Delta\alpha_{\text{old}}) \end{Bmatrix} + J \begin{Bmatrix} dy \\ \kappa d\Delta\alpha \end{Bmatrix} = 0, \quad (5.13)$$

where  $\kappa$  is chosen so that  $J$  is well-conditioned, and

$$J = \begin{bmatrix} \frac{\partial\Psi}{\partial y} & \frac{1}{\kappa} \frac{\partial\Psi}{\partial\alpha} \\ \kappa \frac{\partial A}{\partial y} & \frac{\partial A}{\partial\alpha} \end{bmatrix} \quad (5.14)$$

is a  $2 \times 2$  Jacobian matrix. Rearranging Eq. (5.13) gives

$$\begin{Bmatrix} dy \\ \kappa d\Delta\alpha \end{Bmatrix} = -J^{-1} \begin{Bmatrix} \Psi(y_{\text{old}}, \Delta\alpha_{\text{old}}) \\ \kappa A(y_{\text{old}}, \Delta\alpha_{\text{old}}) \end{Bmatrix}. \quad (5.15)$$

The corrections,  $dy$  and  $d\Delta\alpha$ , can then be obtained and added to the solutions, i.e.,

$$y_{\text{new}} = y_{\text{old}} + dy \quad \text{and} \quad \Delta\alpha_{\text{new}} = \Delta\alpha_{\text{old}} + d\Delta\alpha. \quad (5.16)$$

This process is iterated to convergence. After this, the variables are updated as

$$\alpha = \alpha_n + \Delta\alpha, \quad d = d_n + J(\hat{\gamma}) \Delta\alpha, \quad \boldsymbol{\tau} = (1 - d)^2 \tilde{K} \boldsymbol{\gamma}. \quad (5.17)$$

When deriving the consistent Jacobian,  $\boldsymbol{\gamma}$  is no longer held fixed.  $\Psi$  and  $A$  in Eq. (5.10) then depends on not only  $y$  and  $\Delta\alpha$  but also  $\boldsymbol{\gamma}$ . It is beneficial to relate  $d\Delta\alpha$  to  $d\boldsymbol{\gamma}$ . Totally differentiating Eq. (5.10) and (5.11) gives

$$d\Psi = \frac{\partial\Psi}{\partial y} dy + \frac{\partial\Psi}{\partial\boldsymbol{\gamma}} \cdot d\boldsymbol{\gamma} + \frac{\partial\Psi}{\partial\Delta\alpha} d\Delta\alpha = 0, \quad (5.18)$$

$$dA = \frac{\partial A}{\partial y} dy + \frac{\partial A}{\partial\boldsymbol{\gamma}} \cdot d\boldsymbol{\gamma} + \frac{\partial A}{\partial\Delta\alpha} d\Delta\alpha = 0 \quad (5.19)$$

(see 5.3 for more details on the partial derivatives in Eqs. (5.18) and (5.19)). Solving Eq. (5.18) for  $dy$  gives

$$dy = -\left(\frac{\partial\Psi}{\partial y}\right)^{-1} \left(\frac{\partial\Psi}{\partial\boldsymbol{\gamma}} \cdot d\boldsymbol{\gamma} + \frac{\partial\Psi}{\partial\Delta\alpha} d\Delta\alpha\right). \quad (5.20)$$

Substituting Eq. (5.20) into Eq. (5.19) and solving for  $d\Delta\alpha$  gives

$$d\Delta\alpha = \frac{\frac{\partial A}{\partial y} \left(\frac{\partial\Psi}{\partial y}\right)^{-1} \frac{\partial\Psi}{\partial\boldsymbol{\gamma}} - \frac{\partial A}{\partial\boldsymbol{\gamma}}}{\frac{\partial A}{\partial\Delta\alpha} - \frac{\partial A}{\partial y} \left(\frac{\partial\Psi}{\partial y}\right)^{-1} \frac{\partial\Psi}{\partial\Delta\alpha}} \cdot d\boldsymbol{\gamma} \equiv \mathbf{B} \cdot d\boldsymbol{\gamma}. \quad (5.21)$$

The incremental form of Eq. (4.14) can be obtained as

$$d\boldsymbol{\tau} = dK \boldsymbol{\gamma} + K d\boldsymbol{\gamma}. \quad (5.22)$$

$dK$  can be obtained from Eq. (4.16) as

$$dK = -2(1 - d) \tilde{K} d\Delta d. \quad (5.23)$$

It is beneficial to relate  $d\Delta d$  to  $d\boldsymbol{\gamma}$ .  $d\Delta d$  can be obtained from Eq. (5.9) as

$$d\Delta d = J d\Delta\alpha + \Delta\alpha \frac{\partial J}{\partial\hat{\boldsymbol{\gamma}}} \cdot \mathbf{A} \cdot d\boldsymbol{\gamma} \quad (5.24)$$

(see 5.3 on more details on  $\mathbf{A}$ ). Combining Eqs. (5.21) and (5.24) gives

$$d\Delta d = \left( J \mathbf{B} + \Delta\alpha \frac{\partial J}{\partial\hat{\boldsymbol{\gamma}}} \cdot \mathbf{A} \right) \cdot d\boldsymbol{\gamma}. \quad (5.25)$$

Substituting Eqs. (5.23) and (5.25) into Eq. (5.22) gives

$$d\boldsymbol{\tau} = \left[ -2(1-d)\tilde{K}\boldsymbol{\gamma} \otimes \left( J\mathbf{B} + \Delta\alpha \frac{\partial J}{\partial \hat{\boldsymbol{\gamma}}} \cdot \mathbf{A} \right) + K\mathbf{I} \right] \cdot d\boldsymbol{\gamma} \equiv \mathbf{L} \cdot d\boldsymbol{\gamma}. \quad (5.26)$$

Last but not least, the definition of  $\boldsymbol{\gamma}$  (Eq. (4.3)) indicates that, when  $\gamma_1 < 0$ , the relationship between  $\tau_1$  and  $\gamma_1$  is unspecified. To prevent crack face penetration, set each cohesive element to have a small thickness so that a negative  $\gamma_1$  is admissible. Let  $\tilde{K}_c$  denote the penalty contact stiffness such that

$$\tau_1 = \tilde{K}_c \gamma_1 \quad \text{or} \quad d\tau_1 = \tilde{K}_c d\gamma_1 \quad (5.27)$$

when  $\gamma_1 < 0$ . Numerical experiments indicate that  $\tilde{K}_c = 1000\tilde{K}$  serves the purpose well. Let

$$\mathbf{I}^+ = \begin{bmatrix} H(\gamma_1) & 0 & 0 \\ 0 & 1 & 0 \\ 0 & 0 & 1 \end{bmatrix}, \quad (5.28)$$

where  $H(x)$  denotes the Heaviside step function, i.e.,

$$H(x) = \begin{cases} 0 & x < 0, \\ 1 & x \geq 0. \end{cases} \quad (5.29)$$

Combining Eqs. (5.26)–(5.28) gives

$$\begin{Bmatrix} d\tau_1 \\ d\tau_2 \\ d\tau_3 \end{Bmatrix} = \left[ \mathbf{I}^+ \cdot \mathbf{L} + \tilde{K}_c (\mathbf{I} - \mathbf{I}^+) \right] \begin{Bmatrix} d\gamma_1 \\ d\gamma_2 \\ d\gamma_3 \end{Bmatrix} \equiv \mathbf{L}^* \begin{Bmatrix} d\gamma_1 \\ d\gamma_2 \\ d\gamma_3 \end{Bmatrix}, \quad (5.30)$$

where  $\mathbf{L}^*$  turns out to be the consistent Jacobian. The following can be verified: (1) when  $\gamma_1 \geq 0$ ,  $\mathbf{L}^* = \mathbf{L}$ , and (2) otherwise, the relationship between  $d\tau_1$  and  $d\gamma_1$  obeys Eq. (5.27).

### 5.3 Partial derivatives

In this section, the expressions for the partial derivatives in Eqs. (5.12), (5.18), and (5.19) will be derived. Without loss of generality, assume that  $\Psi$  and  $\mathbf{A}$  are functions of  $y$ ,  $\boldsymbol{\gamma}$ , and  $\Delta\alpha$ . It is beneficial to relate  $d\hat{\boldsymbol{\gamma}}$  to  $d\boldsymbol{\gamma}$ .  $d\hat{\boldsymbol{\gamma}}$  can be expressed as

$$d\hat{\boldsymbol{\gamma}} = \frac{d\boldsymbol{\gamma}}{\gamma} - \frac{d\gamma}{\gamma^2}\boldsymbol{\gamma}, \quad (5.31)$$

and  $d\boldsymbol{\gamma}$  can further be expressed as [131]

$$d\boldsymbol{\gamma} = \frac{d\gamma^2}{2\gamma} = \frac{d(\boldsymbol{\gamma} \cdot \boldsymbol{\gamma})}{2\gamma} = \frac{\boldsymbol{\gamma} \cdot d\boldsymbol{\gamma}}{\gamma}. \quad (5.32)$$

Combining Eqs. (5.31) and (5.32) gives

$$d\hat{\boldsymbol{\gamma}} = \frac{d\boldsymbol{\gamma}}{\gamma} - \frac{\boldsymbol{\gamma} \cdot d\boldsymbol{\gamma}}{\gamma^3}\boldsymbol{\gamma} = \frac{(\boldsymbol{\gamma} \cdot \boldsymbol{\gamma})\mathbf{I} - \boldsymbol{\gamma} \otimes \boldsymbol{\gamma}}{\gamma^3} \cdot d\boldsymbol{\gamma} \equiv \mathbf{A} \cdot d\boldsymbol{\gamma}. \quad (5.33)$$

Recall that

$$d = d_n + \Delta d, \quad \alpha = \alpha_n + \Delta\alpha, \quad \Delta d = J(\hat{\boldsymbol{\gamma}}) \Delta\alpha. \quad (5.34)$$

The following can be obtained from Eq. (5.34):

$$\frac{\partial d}{\partial \Delta d} = \frac{\partial \alpha}{\partial \Delta \alpha} = 1, \quad \frac{\partial(\cdot)}{\partial \Delta \alpha} = \frac{\partial(\cdot)}{\partial \alpha} \frac{\partial \alpha}{\partial \Delta \alpha} = \frac{\partial(\cdot)}{\partial \alpha}, \quad (5.35)$$

$$\frac{\partial \Delta d}{\partial y} = 0, \quad \frac{\partial \Delta d}{\partial \boldsymbol{\gamma}} = \Delta \alpha \frac{\partial J}{\partial \hat{\boldsymbol{\gamma}}} \cdot \mathbf{A}, \quad \frac{\partial \Delta d}{\partial \Delta \alpha} = J. \quad (5.35')$$

Eq. (5.10) indicates that  $\Psi$  is an explicit functions of  $y$ ,  $\boldsymbol{\gamma}$ , and  $d$ , and Eq. (5.35) implies that  $d$  is a function of  $\boldsymbol{\gamma}$  and  $\Delta\alpha$ . Totally differentiating Eq. (5.10) gives

$$\frac{\partial \Psi}{\partial y} = 1, \quad (5.36)$$

$$\frac{\partial \Psi}{\partial \boldsymbol{\gamma}} = \left( \frac{\partial \Psi}{\partial \boldsymbol{\gamma}} \right)_{y,d} + \left( \frac{\partial \Psi}{\partial d} \right)_{y,\boldsymbol{\gamma}} \frac{\partial d}{\partial \Delta d} \frac{\partial \Delta d}{\partial \boldsymbol{\gamma}}, \quad (5.36')$$

$$\frac{\partial \Psi}{\partial \Delta \alpha} = \left( \frac{\partial \Psi}{\partial d} \right)_{y,\boldsymbol{\gamma}} \frac{\partial d}{\partial \Delta d} \frac{\partial \Delta d}{\partial \Delta \alpha}. \quad (5.36')$$

The partial derivatives in Eq. (5.36) can further be expressed as

$$\left( \frac{\partial \Psi}{\partial \boldsymbol{\gamma}} \right)_{y,d} = 2(1-d)\tilde{K}\boldsymbol{\gamma} \quad \text{and} \quad \left( \frac{\partial \Psi}{\partial d} \right)_{y,\boldsymbol{\gamma}} = -\tilde{K}\boldsymbol{\gamma} \cdot \boldsymbol{\gamma}. \quad (5.37)$$

Substituting Eqs. (5.35) and (5.37) into Eq. (5.36) gives

$$\frac{\partial \Psi}{\partial \boldsymbol{\gamma}} = 2(1-d)\tilde{K}\boldsymbol{\gamma} - \Delta\alpha \left( \tilde{K}\boldsymbol{\gamma} \cdot \boldsymbol{\gamma} \right) \frac{\partial J}{\partial \hat{\boldsymbol{\gamma}}} \cdot \mathbf{A}, \quad (5.38)$$

$$\frac{\partial \Psi}{\partial \Delta\alpha} = -J\tilde{K}\boldsymbol{\gamma} \cdot \boldsymbol{\gamma}. \quad (5.36')$$

Totally differentiating Eq. (5.11) gives

$$\frac{\partial A}{\partial y} = -\Delta t \frac{\partial \dot{v}}{\partial y}, \quad \frac{\partial A}{\partial \boldsymbol{\gamma}} = -\Delta t \frac{\partial \dot{v}}{\partial \boldsymbol{\gamma}}, \quad \frac{\partial A}{\partial \Delta\alpha} = 1 - \Delta t \frac{\partial \dot{v}}{\partial \alpha}. \quad (5.39)$$

Hereafter the expressions for  $\partial \dot{v}/\partial y$ ,  $\partial \dot{v}/\partial \boldsymbol{\gamma}$ , and  $\partial \dot{v}/\partial \alpha$  will be derived in turn.

Differentiating Eq. (5.6) with respect to  $y$  gives

$$\frac{\partial \dot{v}}{\partial y} = \frac{n}{\eta} \left( \frac{Jy}{\kappa + A} - 1 \right)^{n-1} \frac{\partial}{\partial y} \left( \frac{Jy}{\kappa + A} - 1 \right) = \frac{nJ}{\eta(\kappa + A)} \left( \frac{Jy}{\kappa + A} - 1 \right)^{n-1}. \quad (5.40)$$

Differentiating Eq. (5.6) with respect to  $\boldsymbol{\gamma}$  gives

$$\begin{aligned} \frac{\partial \dot{v}}{\partial \boldsymbol{\gamma}} &= \frac{n}{\eta} \left( \frac{Jy}{\kappa + A} - 1 \right)^{n-1} \frac{\partial}{\partial \boldsymbol{\gamma}} \left( \frac{Jy}{\kappa + A} - 1 \right) \\ &= \frac{ny}{\eta(\kappa + A)} \left( \frac{Jy}{\kappa + A} - 1 \right)^{n-1} \frac{\partial J}{\partial \hat{\boldsymbol{\gamma}}} \cdot \mathbf{A}. \end{aligned} \quad (5.41)$$

Differentiating Eq. (5.6) with respect to  $\alpha$  gives

$$\begin{aligned} \frac{\partial \dot{v}}{\partial \alpha} &= \frac{n}{\eta} \left( \frac{Jy}{\kappa + A} - 1 \right)^{n-1} \frac{\partial}{\partial \alpha} \left( \frac{Jy}{\kappa + A} - 1 \right) \\ &= -\frac{nJy}{\eta(\kappa + A)^2} \left( \frac{Jy}{\kappa + A} - 1 \right)^{n-1} A'(\alpha). \end{aligned} \quad (5.42)$$

It can be verified that, if  $\boldsymbol{\gamma}$  is held fixed, the above expressions for  $\partial \Psi/\partial y$ ,  $\partial \Psi/\partial \Delta\alpha$ ,  $\partial A/\partial y$ , and  $\partial A/\partial \Delta\alpha$  still hold.

#### 5.4 UMAT algorithm

Figure 5.1 depicts a flowchart of the UMAT algorithm. The algorithm can be described as follows:

1. Read  $\boldsymbol{\tau}_n$  and  $\Delta\boldsymbol{\gamma}$  passed in by Abaqus/Standard, while read  $\boldsymbol{\gamma}_n$ ,  $d_n$ , and  $\alpha_n$  saved for the present element.

2. Check if damage initiates or evolves ( $f \geq 0$ ).
3. If yes, (a) compute  $\Delta\alpha$ , (b) update  $\alpha$ ,  $d$ , and  $\boldsymbol{\tau}$ , and (c) compute  $\mathbf{L}^*$ .
4. Otherwise, (a) update  $\boldsymbol{\gamma}$ , (b) set  $\alpha = \alpha_n$  and  $d = d_n$ , and (c) compute  $\mathbf{L}^*$  (here  $\mathbf{L}^* = K\mathbf{I}^+ + \tilde{K}_c(\mathbf{I} - \mathbf{I}^+)$ ) and  $\boldsymbol{\tau}$ .
5. Save  $\boldsymbol{\gamma}$ ,  $d$ , and  $\alpha$  for the present element, while return  $\boldsymbol{\tau}$  and  $\mathbf{L}^*$  to Abaqus/Standard.

Once  $d = d_c$ , UMAT will set  $K = 0$  and mark the present element as failed hereafter. More details on Abaqus/Standard and UMAT can be found in Ref. [108].

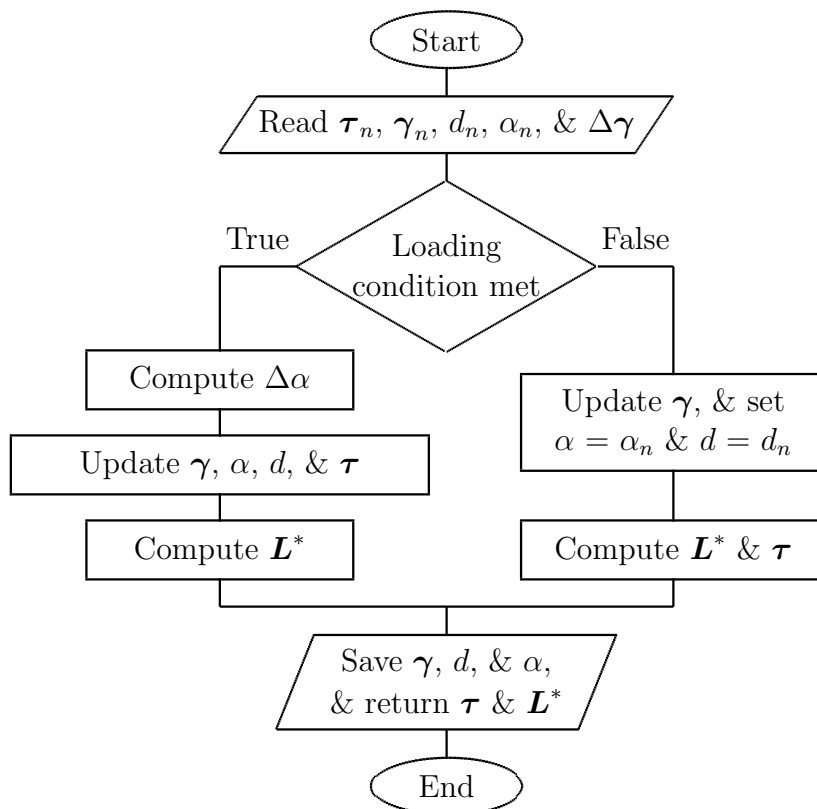


Fig. 5.1. UMAT algorithm.

## 5.5 Numerical examples

Al-Khudairi et al. [143] performed a series of constant amplitude DCB and ENF fatigue crack propagation tests on a type of unidirectional E-glass fiber/E722 composite beams, and recorded the number of cycles for the onset of delamination growth (G–N curves) and crack growth rate for different cyclic strain energy release rates. In this section, the material parameters associated with the present model will first be calibrated from these experimental data. The present model will then be validated by simulating these pure mode tests using Abaqus/Standard. The feasibility of calibrating the interface model from G–N and crack growth rate curves will be evaluated. At last, the model’s capability to handle mixed-mode fatigue delamination will be demonstrated by simulating MMB tests with the same material parameters.

### 5.5.1 Mode I fatigue delamination and calibration of interface parameters

Some of the interface parameters can be predetermined (listed in Table 5.1) based on basic assumptions and measurements from tests. First, the initial interfacial stiffness  $\tilde{K}$  describes the purely elastic response of the interface, thus conclusions from CZM for monotonic loading can be used here. Specifically,  $\tilde{K}$  takes a reasonable value instead of a large penalty value to avoid numerical instabilities at damage initiation. Second, the initial damage threshold  $k$  can be determined from the fatigue limit measured in mode I delamination tests. Fatigue limit in mode I delamination corresponds to the energy release rate  $G_{I,th}$  below which fatigue delamination will not happen. Assuming that every cohesive element in DCB tests exhibits experimental mode I fatigue limit and near elastic behavior under the fatigue limit,  $k$  can be estimated as

$$k = y_0|_{\hat{\gamma}=e_1} = \tilde{K} \gamma_0 \cdot \gamma_0 \Big|_{\hat{\gamma}=e_1} \approx 2G_{I,th}, \quad (5.43)$$

where  $G_{I,th}$  is measured as 114.6 J/m<sup>2</sup>. The mode I traction for fatigue damage initiation can in turn be calculated as  $\tau_{10} = \tilde{K} \gamma_0 \Big|_{\hat{\gamma}=e_1} = 87.0$  MPa. Next, maximum cyclic energy release rates are set as fixed ratios of experimentally determined critical

energy release rates ( $G_{Ic}$  and  $G_{IIc}$ ). Finally,  $\eta$  is regarded as a scaling factor in the viscosity function, and is selected as  $10^6$  for all cases. This assumption is used to alleviate the calibration burden for this example, which should be revoked with more experimental data available for calibration. Therefore, the parameters to be calibrated are  $Q$  and  $b$  in the damage accumulation law (Eq. (4.21)), and  $n$  in the viscosity function (Eq. (5.6)).

Table 5.1.  
Predetermined interface parameters

(a) Chosen.			
$\tilde{K}$ (N/mm <sup>3</sup> )	$d_c$	$\eta$	
$3.3 \times 10^4$	0.95	$10^6$	
(b) Measured and calculated.			
$k$ (J/m <sup>2</sup> )	$\tau_{10}$ (MPa)	$G_{Ic}$ (J/m <sup>2</sup> )	$G_{IIc}$ (J/m <sup>2</sup> )
229.2	87.0	764	1150

To calibrate these three parameters, the DCB cyclic energy release rate versus cycle (G–N) and crack growth rate results from Ref. [143] are used. For the crack growth rate results, only specimen 3’s data are used, to simplify the calibration process. The specimen has a span length ( $2L$ ) of 180 mm, a width ( $b$ ) of 20 mm, a thickness ( $2h$ ) of 8.5 mm, and a initial crack length ( $a_0$ ) of 50 mm. Table 5.2 lists the elastic constants of each laminate. Constant-amplitude cyclic load is applied at the pre-cracked end of the beam with tension-tension displacement control. The ratio of minimum to maximum displacement ( $R$ ) is 0.1, and the load frequency is 5 Hz. Different designated maximum cyclic energy release rate  $G_{I\max}$ ’s are achieved by adjusting the maximum cyclic displacement  $\delta_{I\max}$ , calculated as (ASTM standard D6115 [144])

$$\delta_{I\max} = \sqrt{\frac{2}{3}b(a_0 + |\Delta|) G_{I\max} C_I}, \quad (5.44)$$

where  $|\Delta| = 2.293$  mm is a correction constant measured in Ref. [143], and  $C_I = \delta_{I\max}/P_{I\max}$  is the initial compliance of the DCB specimen that can be obtained from

quasi-static monotonic loading. More details on the experiments can be found in Ref. [143].

Table 5.2.  
Elastic constants of each laminate

(a) Measured.			
$E_1$ (GPa)	$E_2 = E_3$ (GPa)	$G_{12} = G_{13}$ (GPa)	$\nu_{12} = \nu_{13}$
38.9	13.0	5.0	0.24
(b) Chosen.			
$G_{23}$ (GPa)		$\nu_{23}$	
3.7		0.45	

Following the previous CZM, each laminate is idealized as a 2D beam in FEA under plane stress assumptions. Figure 5.2 shows the corresponding finite element model. Zero thickness cohesive elements are inserted between two planar beam sections. The two beam sections are meshed with 4-node quadrilateral elements (CPS4) with 6 elements in the thickness direction (0.708 mm each) and 300 elements in the length direction (0.6 mm each). The cohesive zone consists of 216 4-node cohesive elements having 2 integration points (COH2D4) and a length of 0.6 mm. For DCB tests, the path dependence function  $J$  is set to 1 for all material points in the cohesive zone, assuming that only mode I deformation is present on the local level.

The efficient global optimization (EGO) method is adopted for curve fitting. EGO is a class of Bayesian optimization methods first developed by Jones et al. [145], suitable for expensive unknown function evaluations. In this work, parameters of the unknown function are  $Q$ ,  $b$ , and  $n$ , and each function evaluation consists of:

1. simulating DCB fatigue delamination with five different  $G_{I\max}$  levels (20%, 25%, 30%, 35%, and 40% of  $G_{Ic}$ );
2. extracting simulated crack growth rate and number of cycles to delamination onset for each case;



Fig. 5.2. Finite element model for the DCB specimen.

3. calculating the difference between simulated results and averaged experimental data at these five levels, which serves as the function value.

Specifically, to determine fatigue delamination onset, ASTM standard D6115 [144] recommends using the number of cycles until 1% or 5% of change in the structure's compliance as two quantifiable criteria. To determine crack growth rate in the simulations, the last material point to reach 5% change in stiffness is considered as the crack tip, and the movement speed of the crack tip serves as the crack growth rate. The goal is to find the set of parameters that minimize this function. First, sample points are taken in the design space of the three fitting parameters to perform the first set of evaluations. EGO then uses a surrogate model (e.g., polynomials) to create a response surface that includes the evaluated points, and also provides uncertainty estimation of the entire model. More function evaluations are carried out at most promising locations based on the uncertainty estimation. The surrogate model is thus iteratively updated until a stopping criterion is satisfied. Because the development of an optimization algorithm is beyond the scope of this work, an implementation of EGO by the Dakota toolkit [146] is adopted. Based on the previous CZM and some numerical tests, the initial range for  $Q$ ,  $b$ , and  $n$  are set as 0.01 to 5.

Table 5.3.  
Calibrated interface parameters

$Q$ (J/m <sup>2</sup> )	$b$	$n$
0.864	0.103	1.93

Table 5.3 lists the calibrated parameters. Figure 5.3 shows the fitted G–N and crack growth rate curves. Figure 5.4 compares a segment of the compliance evolution results between experiments and the present model. Within this segment, the rate of compliance increase gradually decreases due to stable crack propagation. Since the goal is to determine the onset of fatigue delamination, rapid failure and unsta-

ble propagation is not studied in both the referenced experiments and the present simulations.

The calibrated curves in Figure 5.3 represent the best fit for the two sets of sparsely distributed experimental data points. In Figure 5.3(a), the calibrated curves are  $C^1$  continuous and shows an asymptotic trend towards the fatigue limit. The curve for 1% compliance lies to the left of the one for 5% compliance change, showing a more conservative prediction for delamination onset. Unlike empirical models, the extrapolated  $G_{I_{\max}}$  value at  $N_f = 1$  does not equal  $G_{Ic}$ . This prediction doesn't harm the present model's validity because: 1) low-cycle fatigue with possible plastic deformation is beyond the scope of this work; 2) cyclic loading with a frequency of 5 Hz is dynamic loading, and the dynamic strength of a material is usually higher than the static strength. Overall, Figure 5.3(a) shows that the present model can create realistic delamination onset results for different loading levels.

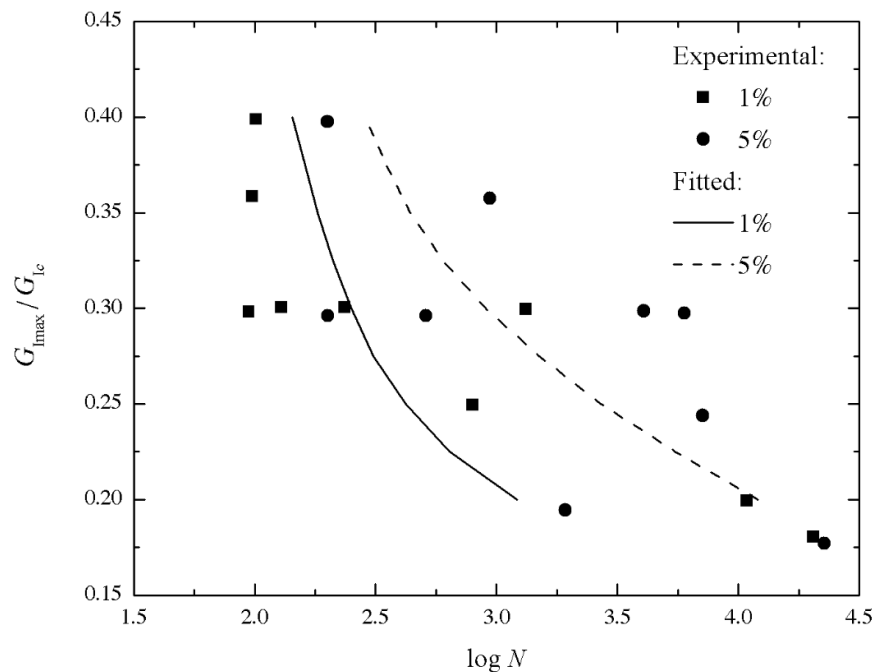
In Figure 5.3(b), the horizontal axis represents the ratio between the maximum cyclic energy release rate and the variation of the critical energy release rate ( $G_{Ir}$ ). Following Ref. [143],  $G_{Ir}$  is obtained as

$$G_{Ir} = G_{Ic} + 20.2(a - a_0)^{0.64}, \quad (5.45)$$

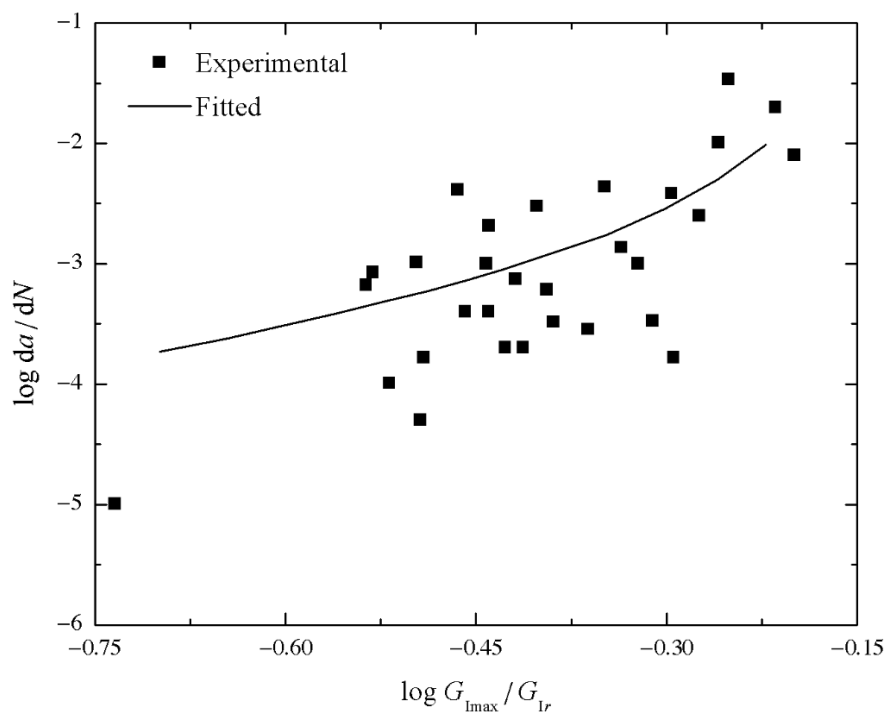
where  $a$  is the instant crack length at the time of measurement. The calibrated curve deviate from the leftmost experimental data point because it is not part of the calibration criteria. Despite the scatter of the experimental data, the calibrated curve can characterize their overall trend.

### 5.5.2 Mode II fatigue delamination

In this section, the parameters calibrated previously using experimental data from mode I fatigue delamination tests will be adopted to predict mode II fatigue delamination on the same material with ENF tests. Experimental crack growth rate results from Ref. [143] will be used for comparison.



(a) G-N curves.



(b) Crack growth rate curve.

Fig. 5.3. (a) G-N and (b) crack growth rate curves for DCB tests.

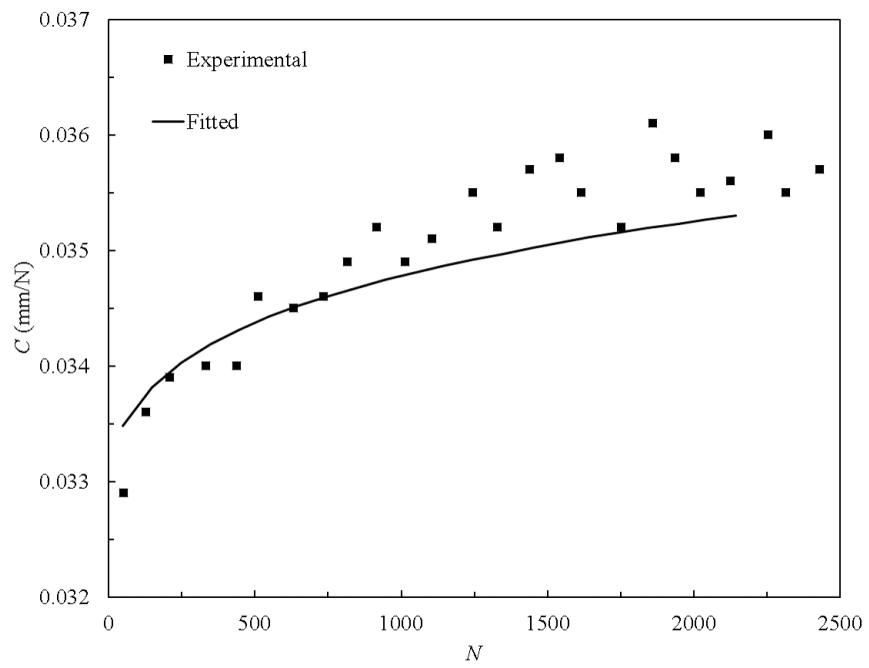


Fig. 5.4. Compliance evolution curve for  $G_{\text{Imax}} = 0.3G_{\text{Ic}}$ .

The specimen has a span length ( $2L$ ) of 100 mm, a width ( $b$ ) of 20 mm, a thickness ( $2h$ ) of 8.5 mm, and a initial crack length ( $a_0$ ) of 25 mm. Constant-amplitude cyclic load is applied on top of the specimen at the middle with displacement control. The ratio of minimum to maximum displacement ( $R$ ) is 0.1, and the load frequency is 5 Hz. Similar to DCB tests, different designated maximum cyclic energy release rate  $G_{\text{IImax}}$ 's are achieved by adjusting the maximum cyclic displacement  $\delta_{\text{IImax}}$ , calculated as

$$\delta_{\text{IImax}} = \sqrt{\frac{2}{9a_0^2} b (2L^3 + 3a_0^3) G_{\text{IImax}} C_{\text{II}}}, \quad (5.46)$$

where  $C_{\text{II}} = \delta_{\text{IImax}}/P_{\text{IImax}}$  is the initial compliance of the structure for ENF tests that can be obtained from quasi-static monotonic loading. The corresponding finite element model has the same element types and sizes as the DCB finite element model. Since  $G_{\text{II,th}}$  is not directly available from experiments, the value of path dependence function  $J$  for mode II can be estimated as the ratio between  $G_{\text{I,th}}$  and  $G_{\text{II,th}}$  at the lowest crack growth rate measured in the experiments,

$$J(e_2) \approx G_{\text{I,th}}/G_{\text{II,th}} \approx G_{\text{I,th}}/G_{\text{II,th}}|_{da/dN=5 \times 10^{-5} \text{mm/cycle}} = 3.05, \quad (5.47)$$

where  $5 \times 10^{-5} \text{mm/cycle}$  is the lowest crack growth rate measured from ENF tests. The path dependence function  $J$  is set to 3.05 for all material points in the cohesive zone, assuming only mode II deformation is present on the local level.

Figure 5.5 compares the predicted crack growth rate curve with the experimental data points. Only specimen 2's experimental data are presented for simplicity. The variation of the critical energy release rate in this example is calculated as  $G_{\text{IIr}} = 0.162a^{2.77}$  [143]. While the simulated curve captures the overall trend, most of the curve lies below the experimental data, signifying a slower crack growth. One possible reason is the path dependence function  $J$  is estimated at  $5 \times 10^{-5} \text{mm/cycle}$ , while  $10^{-7} \text{mm/cycle}$  is the fatigue crack growth threshold recommended by ASTM standard E647 [147]. Additionally, during fatigue delamination tests, phenomena like fiber bridging can also result in differences in fatigue limit measurements [148]. Note that while a higher critical energy release rate is measured for mode II fatigue de-

lamination, a lower fatigue limit is actually obtained based on the above discussion. Complete measurements for fatigue limits in different mode mixture ratios are desired to properly determine the path dependence function for the present model.

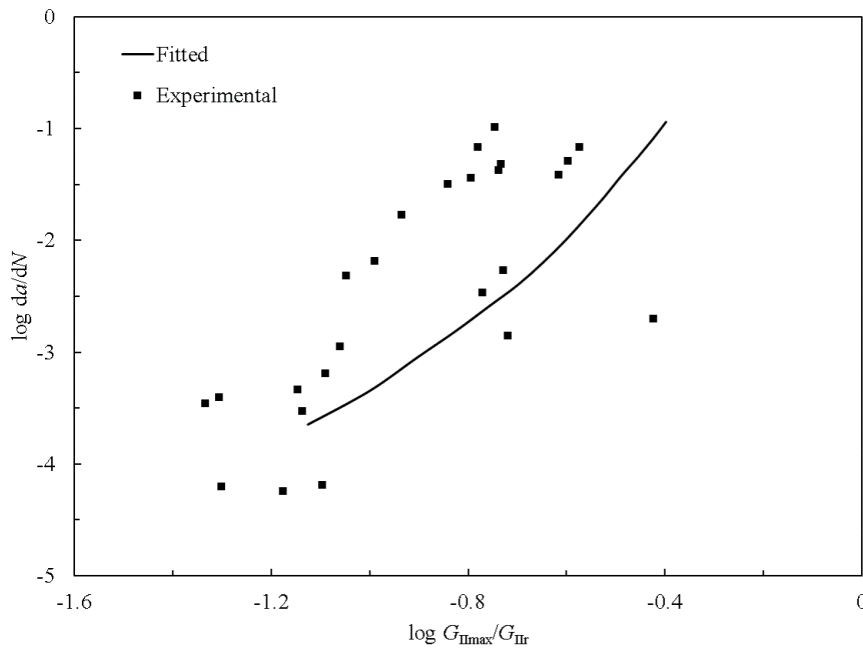


Fig. 5.5. Crack growth rate curve for ENF tests.

### 5.5.3 Mixed mode fatigue delamination

In this section, mixed mode delamination will be simulated with previously calibrated parameters. Let  $\beta_2$  denote the mode mixture ratio, such that  $\beta_2 = G_{II}/G = G_{II}/(G_I + G_{II})$ . The relation between mixed mode critical energy release rate  $G_c$  and  $\beta_2$  needs to be determined. According to Ref. [75], who performed a series of delamination tests with different mode mixture ratios, this relation is usually non-linear. With the lack of data for the above calibrated interface, and for the purpose of demonstration, the calibrated results from the previous CZM is adopted here by

setting the  $(G_c - G_{Ic})/(G_{IIc} - G_{Ic})-\beta_2$  relationship to be the same. Table 5.4 lists the assumed  $G_c-\beta_2$  relationship.

Table 5.4.  
Assumed  $G_c-\beta_2$  and  $J-\beta_2$  relationships.

	DCB	20%MMB	50%MMB	80%MMB	ENF
$\beta_2$	0.0	0.2	0.5	0.8	1.0
$G_c$ (J/m <sup>2</sup> )	764	833	847	974	1150

The MMB finite element model has the same size and mesh as the DCB finite element model. Figure 5.6 shows a sample finite element model of a MMB specimen where the load is applied on a rigid loading lever. The details on how to determine lever length for each mode mixture ratio can be found in ASTM standard D6671 [149].

Figure 5.7 compares the MMB test crack growth rates with the DCB test. ENF test results are not plotted in the same figure due to the differences in specimen sizes. The curves are  $C^1$  continuous and display an acceleration in crack growth rates as the maximum cyclic energy release rates increase. This shows their trends toward eventual failure. In this example, higher mode mixture ratio results in faster crack growth due to the assumptions made to the path dependence function. In reality, higher mode mixture ratio is experimentally tested to reduce crack growth rate. This can be easily implemented with the corresponding fatigue limit data for mixed-mode fatigue delamination. Effects of different fatigue limits can also be properly implemented with a suitable set of experimental data.

## 5.6 Conclusions

In this chapter, a string-based CZM for interlaminar fatigue is developed. A visco-damage model, capable of handling brittle damage behavior, is developed to produce realistic interlaminar crack propagation under high-cycle fatigue. An implicit inte-



Fig. 5.6. Sample finite element model for a MMB specimen.

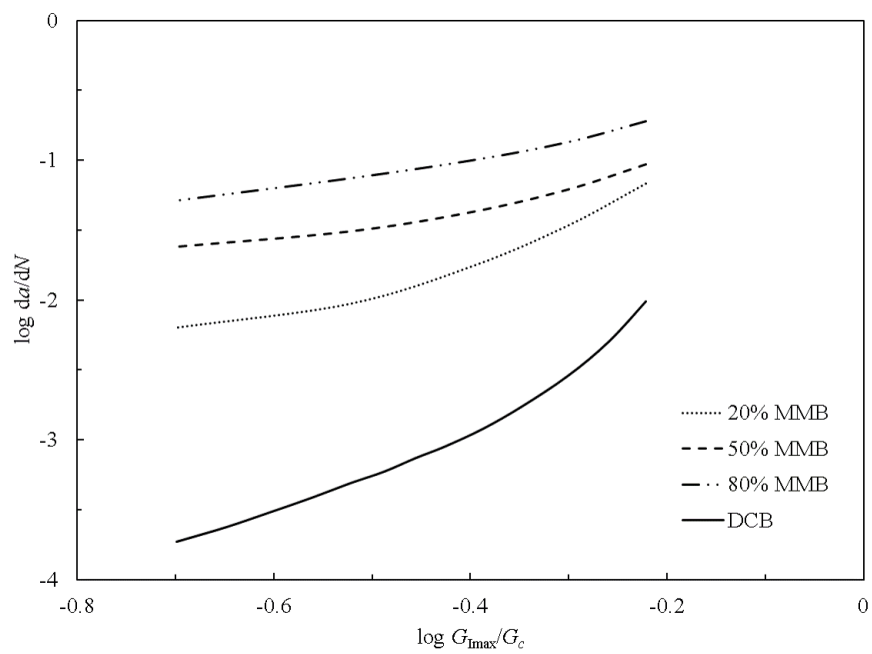


Fig. 5.7. Simulated crack growth rate curves for DCB and MMB tests.

gration scheme, which can handle complex separation paths and mixed-mode delamination, is developed and implemented in Abaqus/Standard via UMAT. A systemic method for choosing and calibrating the interfacial material parameters is presented. The following findings can be obtained from the results:

- The present model is found to handle high-cycle, mixed-mode interlaminar fatigue well.
- It is found to produce stable fatigue crack growth.
- It is found feasible to calibrate a viscodamage CZM through G–N and crack growth rate curves.

## 6. CONCLUSIONS AND RECOMMENDATIONS OF FUTURE WORK

### 6.1 Conclusions

A series of material models for failure prediction in composites have been developed in this work. All models follow the same thermodynamic framework of generalized standard materials. These models possess the following common features:

- They specify the relation between each pair of state variable and its conjugated thermodynamic driving force (e.g., the strain and the stress tensors, and the damage state variable and the damage conjugate force) and a damage function describing the proportionality limit.
- They obey the principle of maximum dissipation.

Using unified thermodynamic principles for different failure mechanisms leads to the following advantages:

- It eliminates the arbitrariness in the selection of damage evolution laws and the loading/unloading conditions for different material behavior.
- It regularizes damage evolution along nonproportional loading paths.
- It simplifies the numerical implementation and modification process by allowing modularization and sharing of material subroutines among different models.

This work also explored different calibration methods for choosing suitable model parameters. While it is not within the scope of this work, a unified calibration method and tool can be easily developed for present models due to their similarity in model formulation.

## 6.2 Recommendations of Future Work

The following topics are recommended for future work:

- Multiscale implementation of generalized standard models — The present models can be incorporated into a multiscale modeling approach (e.g., the mechanics of structure genome [150]) for composite damage and fracture prediction. They can be directly implemented either on the micro- or macro-scale, while requiring a homogenized damage parameter to bridge different scales.
- Global cycle jump scheme for multiscale fatigue simulation — Cycle jump methods (or similar numerical extrapolation methods) are required to efficiently compute structural fatigue. For multiscale fatigue analysis, such a method should also be multiscale, in the sense that microscale error estimations are used to adjust macroscale extrapolation stepsize.
- Machine learning aided material parameter calibration — Machine learning techniques have been applied to more and more aspects in engineering structural design. EGO method used in 5.5.1 is one of them. A more rigorous machine learning technique should include basic material formulation to further improve the accuracy of parameter calibration.

## REFERENCES

## REFERENCES

- [1] S. A. Silling, “Reformulation of elasticity theory for discontinuities and long-range forces,” *Journal of the Mechanics and Physics of Solids*, vol. 48, no. 1, pp. 175–209, 2000.
- [2] Z. P. Bažant and M. Jirásek, “Nonlocal integral formulations of plasticity and damage: survey of progress,” *Journal of Engineering Mechanics*, vol. 128, no. 11, pp. 1119–1149, 2002.
- [3] B. Halphen and Q. S. Nguyen, “Sur les matériaux standard généralisés,” *Journal de Mécanique*, vol. 14, pp. 39–63, 1975.
- [4] J. C. Simo and M. Ortiz, “A unified approach to finite deformation elastoplastic analysis based on the use of hyperelastic constitutive equations,” *Computer Methods in Applied Mechanics and Engineering*, vol. 49, no. 2, pp. 221–245, 1985.
- [5] J. C. Simo and J. W. Ju, “Strain-and stress-based continuum damage modelsii. computational aspects,” *International Journal of Solids and Structures*, vol. 23, no. 7, pp. 841–869, 1987.
- [6] K. Hackl, “Generalized standard media and variational principles in classical and finite strain elastoplasticity,” *Journal of the Mechanics and Physics of Solids*, vol. 45, no. 5, pp. 667–688, 1997.
- [7] J. C. Simo and T. J. R. Hughes, *Computational Inelasticity*. Springer, 1998, vol. 7.
- [8] K. Hackl and F. D. Fischer, “On the relation between the principle of maximum dissipation and inelastic evolution given by dissipation potentials,” in *Proceedings of the Royal Society of London A: Mathematical, Physical and Engineering Sciences*, vol. 464, no. 2089. The Royal Society, 2008, pp. 117–132.
- [9] J.-L. Chaboche, “Continuous damage mechanics—a tool to describe phenomena before crack initiation,” *Nuclear Engineering and Design*, vol. 64, no. 2, pp. 233–247, 1981.
- [10] D. Krajcinovic and G. U. Fonseka, “The continuous damage theory of brittle materials. Part I: General theory,” *Journal of Applied Mechanics*, vol. 48, no. 4, p. 809, 1981.
- [11] S. Murakami and N. Ohno, “A continuum theory of creep and creep damage,” in *Creep in Structures*. Springer, 1981, pp. 422–444.
- [12] P. Germain, Q. S. Nguyen, and P. Suquet, “Continuum thermodynamics,” *Journal of Applied Mechanics*, vol. 50, no. 4b, pp. 1010–1020, 1983.

- [13] D. Krajcinovic, "Continuous damage mechanics," *Applied Mechanics Reviews*, vol. 37, no. 1, pp. 1–6, 1984.
- [14] M. Ortiz, "A constitutive theory for the inelastic behavior of concrete," *Mechanics of Materials*, vol. 4, no. 1, pp. 67–93, 1985.
- [15] R. Talreja, "A continuum mechanics characterization of damage in composite materials," *Proceedings of the Royal Society of London A: Mathematical, Physical and Engineering Sciences*, vol. 399, no. 1817, pp. 195–216, 1985.
- [16] C. L. Chow and J. Wang, "An anisotropic theory of continuum damage mechanics for ductile fracture," *Engineering Fracture Mechanics*, vol. 27, no. 5, pp. 547–558, 1987.
- [17] J. W. Ju, "On energy-based coupled elastoplastic damage theories: constitutive modeling and computational aspects," *International Journal of Solids and Structures*, vol. 25, no. 7, pp. 803–833, 1989.
- [18] G. Z. Voyiadjis and P. I. Kattan, "Damage of fiber-reinforced composite materials with micromechanical characterization," *International Journal of Solids and Structures*, vol. 30, no. 20, pp. 2757–2778, 1993.
- [19] J. Lemaitre, *A Course on Damage Mechanics*. Springer Science & Business Media, 2012.
- [20] J. Besson, G. Cailletaud, J.-L. Chaboche, and S. Forest, *Non-linear Mechanics of Materials*, ser. Solid Mechanics and Its Applications. New York: Springer, 2009, vol. 167.
- [21] Z. P. Bažant and G. Pijaudier-Cabot, "Measurement of characteristic length of nonlocal continuum," *Journal of Engineering Mechanics*, vol. 115, no. 4, pp. 755–767, 1989.
- [22] Z. P. Bažant, "Instability, ductility, and size effect in strain-softening concrete," *Journal of the Engineering Mechanics Division*, vol. 102, no. 2, pp. 331–344, 1976.
- [23] G. Pijaudier-Cabot and Z. P. Bažant, "Nonlocal damage theory," *Journal of Engineering Mechanics*, vol. 113, no. 10, pp. 1512–1533, 1987.
- [24] G. Borino, P. Fuschi, and C. Polizzotto, "A thermodynamic approach to nonlocal plasticity and related variational principles," *Journal of Applied Mechanics*, vol. 66, pp. 952–963, 1999.
- [25] G. Borino, B. Failla, and F. Parrinello, "A symmetric nonlocal damage theory," *International Journal of Solids and Structures*, vol. 40, no. 13, pp. 3621–3645, 2003.
- [26] C. Comi and U. Perego, "Numerical aspects of nonlocal damage analyses," *Revue européenne des éléments finis*, vol. 10, no. 2-4, pp. 227–242, 2001.
- [27] E. Lorentz and S. Andrieux, "Analysis of non-local models through energetic formulations," *International Journal of Solids and Structures*, vol. 40, no. 12, pp. 2905–2936, 2003.

- [28] P. Grassl and M. Jirásek, “Plastic model with non-local damage applied to concrete,” *International Journal for Numerical and Analytical Methods in Geomechanics*, vol. 30, no. 1, pp. 71–90, 2006.
- [29] G. D. Nguyen and A. M. Korsunsky, “Development of an approach to constitutive modelling of concrete: isotropic damage coupled with plasticity,” *International Journal of Solids and Structures*, vol. 45, no. 20, pp. 5483–5501, 2008.
- [30] R. H. J. Peerlings, R. De Borst, W. A. M. Brekelmans, and J. H. P. De Vree, “Gradient enhanced damage for quasi-brittle materials,” *International Journal for Numerical Methods in Engineering*, vol. 39, pp. 3391–3403, 1996.
- [31] R. H. J. Peerlings, R. De Borst, W. A. M. Brekelmans, and M. G. D. Geers, “Gradient-enhanced damage modelling of concrete fracture,” *Mechanics of Cohesive-Frictional Materials*, vol. 3, no. 4, pp. 323–342, 1998.
- [32] M. G. D. Geers, R. De Borst, and R. H. J. Peerlings, “Damage and crack modeling in single-edge and double-edge notched concrete beams,” *Engineering Fracture Mechanics*, vol. 65, no. 2, pp. 247–261, 2000.
- [33] R. Desmorat, F. Gatuingt, and F. Ragueneau, “Nonlocal anisotropic damage model and related computational aspects for quasi-brittle materials,” *Engineering Fracture Mechanics*, vol. 74, no. 10, pp. 1539–1560, 2007.
- [34] R. K. Abu Al-Rub and G. Z. Voyiadjis, “Gradient-enhanced coupled plasticity-anisotropic damage model for concrete fracture: computational aspects and applications,” *International Journal of Damage Mechanics*, vol. 18, no. 2, pp. 115–154, 2009.
- [35] L. H. Poh and S. Swaddiwudhipong, “Over-nonlocal gradient enhanced plastic-damage model for concrete,” *International Journal of Solids and Structures*, vol. 46, no. 25, pp. 4369–4378, 2009.
- [36] L. Zhang and W. Yu, “Constitutive modeling of damageable brittle and quasi-brittle materials,” *International Journal of Solids and Structures*, vol. 117, pp. 80–90, 2017.
- [37] J. Fish, Q. Yu, and K. Shek, “Computational damage mechanics for composite materials based on mathematical homogenization,” *International Journal for Numerical Methods in Engineering*, vol. 45, no. 11, pp. 1657–1679, 1999.
- [38] J. Fish and Q. Yu, “Computational mechanics of fatigue and life predictions for composite materials and structures,” *Computer Methods in Applied Mechanics and Engineering*, vol. 191, no. 43, pp. 4827–4849, 2002.
- [39] J. J. Marigo, “Modelling of brittle and fatigue damage for elastic material by growth of microvoids,” *Engineering Fracture Mechanics*, vol. 21, no. 4, pp. 861–874, 1985.
- [40] M. H. J. W. Paas, P. J. G. Schreurs, and W. A. M. Brekelmans, “A continuum approach to brittle and fatigue damage: theory and numerical procedures,” *International Journal of Solids and Structures*, vol. 30, no. 4, pp. 579–599, 1993.

- [41] E. Papa, “A damage model for concrete subjected to fatigue loading,” *European Journal Mechanics A/Solids*, vol. 12, no. 3, pp. 429–440, 1993.
- [42] S. H. Mai, F. Le-Corre, G. Forêt, and B. Nedjar, “A continuum damage modeling of quasi-static fatigue strength of plain concrete,” *International Journal of Fatigue*, vol. 37, pp. 79–85, 2012.
- [43] A. Pandolfi and A. Taliercio, “Bounding surface models applied to fatigue of plain concrete,” *Journal of Engineering Mechanics*, vol. 124, no. 5, pp. 556–564, 1998.
- [44] W. Suaris, C. Ouyang, and V. M. Fernando, “Damage model for cyclic loading of concrete,” *Journal of Engineering Mechanics*, vol. 116, no. 5, pp. 1020–1035, 1990.
- [45] E. Papa and A. Taliercio, “Anisotropic damage model for the multiaxial static and fatigue behaviour of plain concrete,” *Engineering Fracture Mechanics*, vol. 55, no. 2, pp. 163–179, 1996.
- [46] A. Alliche, “Damage model for fatigue loading of concrete,” *International Journal of Fatigue*, vol. 26, no. 9, pp. 915–921, 2004.
- [47] J. Liang, X. Ren, and J. Li, “A competitive mechanism driven damage-plasticity model for fatigue behavior of concrete,” *International Journal of Damage Mechanics*, vol. 25, no. 3, pp. 377–399, 2016.
- [48] J.-K. Kim and Y.-Y. Kim, “Experimental study of the fatigue behavior of high strength concrete,” *Cement and Concrete Research*, vol. 26, no. 10, pp. 1513–1523, 1996.
- [49] L. Gao and C.-T. T. Hsu, “Fatigue of concrete under uniaxial compression cyclic loading,” *Materials Journal*, vol. 95, no. 5, pp. 575–581, 1998.
- [50] J. Chaboche and P. Lesne, “A non-linear continuous fatigue damage model,” *Fatigue & Fracture of Engineering Materials & Structures*, vol. 11, no. 1, pp. 1–17, 1988.
- [51] B. Bhattacharya and B. Ellingwood, “Continuum damage mechanics analysis of fatigue crack initiation,” *International Journal of Fatigue*, vol. 20, no. 9, pp. 631–639, 1998.
- [52] A. Baktheer and R. Chudoba, “Pressure-sensitive bond fatigue model with damage evolution driven by cumulative slip: Thermodynamic formulation and applications to steel-and frp-concrete bond,” *International Journal of Fatigue*, vol. 113, pp. 277–289, 2018.
- [53] R. Desmorat, L. Angrand, P. Gaborit, M. Kaminski, and C. Rakotoarisoa, “On the introduction of a mean stress in kinetic damage evolution laws for fatigue,” *International Journal of Fatigue*, vol. 77, pp. 141–153, 2015.
- [54] V. M. Kindrachuk, M. Thiele, and J. F. Unger, “Constitutive modeling of creep-fatigue interaction for normal strength concrete under compression,” *International Journal of Fatigue*, vol. 78, pp. 81–94, 2015.

- [55] M. Naderi and M. Khonsari, “A thermodynamic approach to fatigue damage accumulation under variable loading,” *Materials Science and Engineering: A*, vol. 527, no. 23, pp. 6133–6139, 2010.
- [56] Z. Ding and J. Li, “A physically motivated model for fatigue damage of concrete,” *International Journal of Damage Mechanics*, vol. 27, no. 8, pp. 1192–1212, 2018.
- [57] D. Halm and A. Dragon, “An anisotropic model of damage and frictional sliding for brittle materials,” *European Journal of Mechanics-A/Solids*, vol. 17, no. 3, pp. 439–460, 1998.
- [58] A. Dragon, D. Halm, and T. Désoyer, “Anisotropic damage in quasi-brittle solids: modelling, computational issues and applications,” *Computer Methods in Applied Mechanics and Engineering*, vol. 183, no. 3-4, pp. 331–352, 2000.
- [59] R. Faria, J. Oliver, and M. Cervera, “A strain-based plastic viscous-damage model for massive concrete structures,” *International Journal of Solids and Structures*, vol. 35, no. 14, pp. 1533–1558, 1998.
- [60] J. Y. Wu, J. Li, and R. Faria, “An energy release rate-based plastic-damage model for concrete,” *International Journal of Solids and Structures*, vol. 43, no. 3, pp. 583–612, 2006.
- [61] R. Masson and A. Zaoui, “Self-consistent estimates for the rate-dependent elastoplastic behaviour of polycrystalline materials,” *Journal of the Mechanics and Physics of Solids*, vol. 47, no. 7, pp. 1543–1568, 1999.
- [62] R. Masson, M. Bornert, P. Suquet, and A. Zaoui, “An affine formulation for the prediction of the effective properties of nonlinear composites and polycrystals,” *Journal of the Mechanics and Physics of Solids*, vol. 48, no. 6-7, pp. 1203–1227, 2000.
- [63] O. Pierard and I. Doghri, “An enhanced affine formulation and the corresponding numerical algorithms for the mean-field homogenization of elasto-viscoplastic composites,” *International Journal of Plasticity*, vol. 22, no. 1, pp. 131–157, 2006.
- [64] O. Pierard, J. LLorca, J. Segurado, and I. Doghri, “Micromechanics of particle-reinforced elasto-viscoplastic composites: finite element simulations versus affine homogenization,” *International Journal of Plasticity*, vol. 23, no. 6, pp. 1041–1060, 2007.
- [65] I. Doghri, L. Adam, and N. Bilger, “Mean-field homogenization of elasto-viscoplastic composites based on a general incrementally affine linearization method,” *International Journal of Plasticity*, vol. 26, no. 2, pp. 219–238, 2010.
- [66] L. Zhang and W. Yu, “A micromechanics approach to homogenizing elasto-viscoplastic heterogeneous materials,” *International Journal of Solids and Structures*, vol. 51, no. 23, pp. 3878–3888, 2014.
- [67] D. S. Dugdale, “Yielding of steel sheets containing slits,” *Journal of the Mechanics and Physics of Solids*, vol. 8, no. 2, pp. 100–104, 1960.

- [68] G. I. Barenblatt, "The mathematical theory of equilibrium cracks in brittle fracture," *Advances in Applied Mechanics*, vol. 7, pp. 55–129, 1962.
- [69] P. P. Camanho and C. G. Dávila, "Mixed-mode decohesion finite elements for the simulation of delamination in composite materials," *NASA/TM-2002-211737*, pp. 1–37, 2002.
- [70] P. W. Harper and S. R. Hallett, "Cohesive zone length in numerical simulations of composite delamination," *Engineering Fracture Mechanics*, vol. 75, no. 16, pp. 4774–4792, 2008.
- [71] J. R. Reeder, "An evaluation of mixed-mode delamination failure criteria," *NASA-TM-104210*, pp. 1–50, 1992.
- [72] A. Turon, P. P. Camanho, J. Costa, and J. Renart, "Accurate simulation of delamination growth under mixed-mode loading using cohesive elements: definition of interlaminar strengths and elastic stiffness," *Composite Structures*, vol. 92, no. 8, pp. 1857–1864, 2010.
- [73] C. Sarrado, A. Turon, J. Renart, and I. Urresti, "Assessment of energy dissipation during mixed-mode delamination growth using cohesive zone models," *Composites Part A: Applied Science and Manufacturing*, vol. 43, no. 11, pp. 2128–2136, 2012.
- [74] K. Park and G. H. Paulino, "Cohesive zone models: a critical review of traction-separation relationships across fracture surfaces," *Applied Mechanics Reviews*, vol. 64, no. 6, p. 060802, 2011.
- [75] J. R. Reeder and J. H. Crews, "Mixed-mode bending method for delamination testing," *AIAA Journal*, vol. 28, no. 7, pp. 1270–1276, 1990.
- [76] O. Allix, P. Ladevèze, and A. Corigliano, "Damage analysis of interlaminar fracture specimens," *Composite Structures*, vol. 31, no. 1, pp. 61–74, 1995.
- [77] O. Allix and A. Corigliano, "Modeling and simulation of crack propagation in mixed-modes interlaminar fracture specimens," *International Journal of Fracture*, vol. 77, no. 2, pp. 111–140, 1996.
- [78] O. Allix and A. Corigliano, "Geometrical and interfacial non-linearities in the analysis of delamination in composites," *International Journal of Solids and Structures*, vol. 36, no. 15, pp. 2189–2216, 1999.
- [79] R. Borg, L. Nilsson, and K. Simonsson, "Simulation of delamination in fiber composites with a discrete cohesive failure model," *Composites Science and Technology*, vol. 61, no. 5, pp. 667–677, 2001.
- [80] R. Borg, L. Nilsson, and K. Simonsson, "Modeling of delamination using a discretized cohesive zone and damage formulation," *Composites Science and Technology*, vol. 62, no. 10, pp. 1299–1314, 2002.
- [81] A. Turon, P. P. Camanho, J. Costa, and C. Dávila, "A damage model for the simulation of delamination in advanced composites under variable-mode loading," *Mechanics of Materials*, vol. 38, no. 11, pp. 1072–1089, 2006.

- [82] A. Turon, C. G. Davila, P. P. Camanho, and J. Costa, “An engineering solution for mesh size effects in the simulation of delamination using cohesive zone models,” *Engineering Fracture Mechanics*, vol. 74, no. 10, pp. 1665–1682, 2007.
- [83] L. C. Overgaard, E. Lund, and P. P. Camanho, “A methodology for the structural analysis of composite wind turbine blades under geometric and material induced instabilities,” *Computers & Structures*, vol. 88, no. 19, pp. 1092–1109, 2010.
- [84] J. Mosler and I. Scheider, “A thermodynamically and variationally consistent class of damage-type cohesive models,” *Journal of the Mechanics and Physics of Solids*, vol. 59, no. 8, pp. 1647–1668, 2011.
- [85] A. De-Andrés, J. Pérez, and M. Ortiz, “Elastoplastic finite element analysis of three-dimensional fatigue crack growth in aluminum shafts subjected to axial loading,” *International Journal of Solids and Structures*, vol. 36, no. 15, pp. 2231–2258, 1999.
- [86] A. Turon, J. Costa, P. Camanho, and C. Dávila, “Simulation of delamination in composites under high-cycle fatigue,” *Composites Part A: Applied Science and Manufacturing*, vol. 38, no. 11, pp. 2270–2282, 2007.
- [87] A. Pirondi and F. Moroni, “A progressive damage model for the prediction of fatigue crack growth in bonded joints,” *The Journal of Adhesion*, vol. 86, no. 5-6, pp. 501–521, 2010.
- [88] P. W. Harper and S. R. Hallett, “A fatigue degradation law for cohesive interface elements—development and application to composite materials,” *International Journal of Fatigue*, vol. 32, no. 11, pp. 1774–1787, 2010.
- [89] L. F. Kawashita and S. R. Hallett, “A crack tip tracking algorithm for cohesive interface element analysis of fatigue delamination propagation in composite materials,” *International Journal of Solids and Structures*, vol. 49, no. 21, pp. 2898–2913, 2012.
- [90] H. Khoramishad, A. Crocombe, K. Katnam, and I. Ashcroft, “Predicting fatigue damage in adhesively bonded joints using a cohesive zone model,” *International Journal of Fatigue*, vol. 32, no. 7, pp. 1146–1158, 2010.
- [91] D. Tumino and F. Cappello, “Simulation of fatigue delamination growth in composites with different mode mixtures,” *Journal of Composite Materials*, vol. 41, no. 20, pp. 2415–2441, 2007.
- [92] B. Yang, S. Mall, and K. Ravi-Chandar, “A cohesive zone model for fatigue crack growth in quasibrittle materials,” *International Journal of Solids and Structures*, vol. 38, no. 22-23, pp. 3927–3944, 2001.
- [93] O. Nguyen, E. Repetto, M. Ortiz, and R. Radovitzky, “A cohesive model of fatigue crack growth,” *International Journal of Fracture*, vol. 110, no. 4, pp. 351–369, 2001.
- [94] K. Roe and T. Siegmund, “An irreversible cohesive zone model for interface fatigue crack growth simulation,” *Engineering Fracture Mechanics*, vol. 70, no. 2, pp. 209–232, 2003.

- [95] A. Abdul-Baqi, P. Schreurs, and M. Geers, “Fatigue damage modeling in solder interconnects using a cohesive zone approach,” *International Journal of Solids and Structures*, vol. 42, no. 3-4, pp. 927–942, 2005.
- [96] N. Jagannathan, A. A. Chandra, and C. Manjunatha, “Onset-of-growth behavior of mode II delamination in a carbon fiber composite under spectrum fatigue loads,” *Composite Structures*, vol. 132, pp. 477–483, 2015.
- [97] A. Corigliano and M. Ricci, “Rate-dependent interface models: formulation and numerical applications,” *International Journal of Solids and Structures*, vol. 38, no. 4, pp. 547–576, 2001.
- [98] E. J. Kramer, “Microscopic and molecular fundamentals of crazing,” *Advances in Polymer Science*, vol. 52/53, pp. 1–56, 1983.
- [99] E. J. Kramer and L. L. Berger, “Fundamental processes of craze growth and fracture,” *Advances in Polymer Science*, vol. 91/92, pp. 1–68, 1990.
- [100] M. Musto and G. Alfano, “A novel rate-dependent cohesive-zone model combining damage and visco-elasticity,” *Computers & Structures*, vol. 118, pp. 126–133, 2013.
- [101] ———, “A fractional rate-dependent cohesive-zone model,” *International Journal for Numerical Methods in Engineering*, vol. 103, no. 5, pp. 313–341, 2015.
- [102] F. Parrinello, G. Marannano, and G. Borino, “A thermodynamically consistent cohesive-frictional interface model for mixed mode delamination,” *Engineering Fracture Mechanics*, vol. 153, pp. 61–79, 2016.
- [103] A. C. Eringen and D. G. B. Edelen, “On nonlocal elasticity,” *International Journal of Engineering Science*, vol. 10, no. 3, pp. 233–248, 1972.
- [104] J. P. Cordebois and F. Sidoroff, “Anisotropie élastique induite par endommagement,” *Comportement Mécanique des Solides Anisotropes*, no. 295, pp. 761–774, 1979.
- [105] J. Betten, “Damage tensors in continuum mechanics,” *Journal de Mécanique Théorique et Appliquée*, vol. 2, no. 1, pp. 13–32, 1983.
- [106] R. B. Nelson, “Simplified calculation of eigenvector derivatives,” *AIAA Journal*, vol. 14, no. 9, pp. 1201–1205, 1976.
- [107] J.-L. Chaboche, “Development of continuum damage mechanics for elastic solids sustaining anisotropic and unilateral damage,” *International Journal of Damage Mechanics*, vol. 2, no. 4, pp. 311–329, 1993.
- [108] Simulia. (2013) Abaqus 6.13 documentation.
- [109] R. Kress, *Linear integral equations*. Springer Science & Business Media, 2013, vol. 82.
- [110] P. Ladevèze, A. Gasser, and O. Allix, “Damage mechanisms modeling for ceramic composites,” *Journal of Engineering Materials and Technology*, vol. 116, no. 3, pp. 331–336, 1994.

- [111] R. A. Einfeld and M. S. Velasco, "Fracture parameters for high-performance concrete," *Cement and Concrete Research*, vol. 36, no. 3, pp. 576–583, 2006.
- [112] J. Roesler, G. H. Paulino, K. Park, and C. Gaedicke, "Concrete fracture prediction using bilinear softening," *Cement and Concrete Composites*, vol. 29, no. 4, pp. 300–312, 2007.
- [113] Z. Zhao, S. H. Kwon, and S. P. Shah, "Effect of specimen size on fracture energy and softening curve of concrete: Part I. Experiments and fracture energy," *Cement and Concrete Research*, vol. 38, no. 8, pp. 1049–1060, 2008.
- [114] L. Skarzynski and J. Tejchman, "Calculations of fracture process zones on meso-scale in notched concrete beams subjected to three-point bending," *European Journal of Mechanics-A/Solids*, vol. 29, no. 4, pp. 746–760, 2010.
- [115] C. Le Bellégo, B. Gérard, and G. Pijaudier-Cabot, "Chemo-mechanical effects in mortar beams subjected to water hydrolysis," *Journal of Engineering Mechanics*, vol. 126, no. 3, pp. 266–272, 2000.
- [116] C. Le Bellégo, J. F. Dubé, G. Pijaudier-Cabot, and B. Gérard, "Calibration of nonlocal damage model from size effect tests," *European Journal of Mechanics-A/Solids*, vol. 22, no. 1, pp. 33–46, 2003.
- [117] J.-Y. Wu, "A unified phase-field theory for the mechanics of damage and quasi-brittle failure," *Journal of the Mechanics and Physics of Solids*, vol. 103, pp. 72–99, 2017.
- [118] M. B. Nooru-Mohamed, *Mixed-Mode Fracture of Concrete: An Experimental Approach*. Delft University of Technology, Ph.D. Thesis, 1992.
- [119] R. K. Abu Al-Rub and S.-M. Kim, "Computational applications of a coupled plasticity-damage constitutive model for simulating plain concrete fracture," *Engineering Fracture Mechanics*, vol. 77, no. 10, pp. 1577–1603, 2010.
- [120] P. Perzyna, "Fundamental problems in viscoplasticity," in *Advances in Applied Mechanics*. Academic Press, 1966, vol. 9, pp. 243–377.
- [121] W. H. Press, B. P. Flannery, S. A. Teukolsky, and W. T. Vetterling, *Numerical Recipes in C: the Art of Scientific Computing*. Cambridge University Press, 1992.
- [122] H. A. W. Cornelissen and H. W. Reinhardt, "Uniaxial tensile fatigue failure of concrete under constant-amplitude and programme loading," *Magazine of Concrete Research*, vol. 36, no. 129, pp. 216–226, 1984.
- [123] D. P. Cole, T. C. Henry, F. Gardea, and R. A. Haynes, "Interphase mechanical behavior of carbon fiber reinforced polymer exposed to cyclic loading," *Composites Science and Technology*, vol. 151, pp. 202–210, 2017.
- [124] N. V. Akshantala and R. Talreja, "A micromechanics based model for predicting fatigue life of composite laminates," *Materials Science and Engineering: A*, vol. 285, no. 1-2, pp. 303–313, 2000.

- [125] A. N. Gent and R. P. Petrich, "Adhesion of viscoelastic materials to rigid substrates," in *Proceedings of the Royal Society of London A: Mathematical, Physical and Engineering Sciences*, vol. 310, no. 1502. The Royal Society, 1969, pp. 433–448.
- [126] C. Y. Hui, A. Ruina, C. Creton, and E. J. Kramer, "Micromechanics of crack growth into a craze in a polymer glass," *Macromolecules*, vol. 25, no. 15, pp. 3948–3955, 1992.
- [127] C. Y. Hui, A. Ruina, R. Long, and A. Jagota, "Cohesive zone models and fracture," *The Journal of Adhesion*, vol. 87, no. 1, pp. 1–52, 2011.
- [128] M. Ortiz and A. Pandolfi, "Finite-deformation irreversible cohesive elements for three-dimensional crack-propagation analysis," *International Journal for Numerical Methods in Engineering*, vol. 44, no. 9, pp. 1267–1282, 1999.
- [129] G. Z. Voyiadjis and P. I. Kattan, *Advances in Damage Mechanics: Metals and Metal Matrix Composites*. Elsevier Science, 1999.
- [130] J. P. Cordebois and F. Sidoroff, "Anisotropic damage in elasticity and plasticity," *Journal de Mécanique Théorique et Appliquée*, pp. 45–60, 1982.
- [131] A. A. Benzerga and J. Besson, "Plastic potentials for anisotropic porous solids," *European Journal of Mechanics, A/Solids*, vol. 20, no. 3, pp. 397–434, 2001.
- [132] Y. Luo, "A local multivariate lagrange interpolation method for constructing shape functions," *International Journal for Numerical Methods in Biomedical Engineering*, vol. 26, no. 2, pp. 252–261, 2010.
- [133] M. L. Benzeggagh and M. Kenane, "Measurement of mixed-mode delamination fracture toughness of unidirectional glass/epoxy composites with mixed-mode bending apparatus," *Composites Science and Technology*, vol. 56, no. 4, pp. 439–449, 1996.
- [134] C. Balzani and W. Wagner, "An interface element for the simulation of delamination in unidirectional fiber-reinforced composite laminates," *Engineering Fracture Mechanics*, vol. 75, no. 9, pp. 2597–2615, 2008.
- [135] B. Blaysat, J. P. Hoefnagels, G. Lubineau, M. Alfano, and M. G. Geers, "Interface debonding characterization by image correlation integrated with double cantilever beam kinematics," *International Journal of Solids and Structures*, vol. 55, pp. 79–91, 2015.
- [136] S. T. Pinho, L. Iannucci, and P. Robinson, "Formulation and implementation of decohesion elements in an explicit finite element code," *Composites Part A: Applied Science and Manufacturing*, vol. 37, no. 5, pp. 778–789, 2006.
- [137] A. M. Elmarakbi, N. Hu, and H. Fukunaga, "Finite element simulation of delamination growth in composite materials using LS-DYNA," *Composites Science and Technology*, vol. 69, no. 14, pp. 2383–2391, 2009.
- [138] Z. Gao, L. Zhang, and W. Yu, "Simulating the mixed-mode progressive delamination in composite laminates," in *American Society of Composites-30th Technical Conference*, 2015.

- [139] C. G. Dávila, P. P. Camanho, and A. Turon, “Effective simulation of delamination in aeronautical structures using shells and cohesive elements,” *Journal of Aircraft*, vol. 45, no. 2, pp. 663–672, 2008.
- [140] D. Xie and A. M. Waas, “Discrete cohesive zone model for mixed-mode fracture using finite element analysis,” *Engineering Fracture Mechanics*, vol. 73, no. 13, pp. 1783–1796, 2006.
- [141] C. Schuecker and B. D. Davidson, “Evaluation of the accuracy of the four-point bend end-notched flexure test for mode II delamination toughness determination,” *Composites Science and Technology*, vol. 60, no. 11, pp. 2137–2146, 2000.
- [142] B. R. K. Blackman, A. J. Brunner, and J. G. Williams, “Mode II fracture testing of composites: a new look at an old problem,” *Engineering Fracture Mechanics*, vol. 73, no. 16, pp. 2443–2455, 2006.
- [143] O. Al-Khudairi, H. Hadavinia, A. Waggott, E. Lewis, and C. Little, “Characterising mode I/mode II fatigue delamination growth in unidirectional fibre reinforced polymer laminates,” *Materials & Design (1980-2015)*, vol. 66, pp. 93–102, 2015.
- [144] ASTM, *ASTM D6115-97 Standard Test Method for Mode I Fatigue Delamination Growth Onset of Unidirectional Fiber-Reinforced Polymer Matrix Composites*, Std., 2019.
- [145] D. R. Jones, M. Schonlau, and W. J. Welch, “Efficient global optimization of expensive black-box functions,” *Journal of Global optimization*, vol. 13, no. 4, pp. 455–492, 1998.
- [146] Sandia. (2019) Dakota, a multilevel parallel object-oriented framework for design optimization, parameter estimation, uncertainty quantification, and sensitivity analysis: version 6.10 user’s manual.
- [147] ASTM, *ASTM E647-15e1 Standard Test Method for Measurement of Fatigue Crack Growth Rates*, Std., 2016.
- [148] B. L. Bak, C. Sarrado, A. Turon, and J. Costa, “Delamination under fatigue loads in composite laminates: a review on the observed phenomenology and computational methods,” *Applied Mechanics Reviews*, vol. 66, no. 6, p. 060803, 2014.
- [149] ASTM, *ASTM D6671/D6671M-19 Standard Test Method for Mixed Mode I-Mode II Interlaminar Fracture Toughness of Unidirectional Fiber Reinforced Polymer Matrix Composites*, Std., 2019.
- [150] W. Yu, “A unified theory for constitutive modeling of composites,” *Journal of Mechanics of Materials and Structures*, vol. 11, no. 4, pp. 379–411, 2016.

VITA

## VITA

### EDUCATION

- Master of Science in Aeronautics and Astronautics at Purdue University, Aug 2013 – Jun 2015. Thesis title: “Comprehensively simulating the mixed-mode progressive delamination in composite laminates.”
- Bachelor of Science in Aeronautics and Astronautics at Beihang University, Aug 2009 – Jun 2013.

### ACADEMIC EMPLOYMENT

- Graduate Research Assistant, School of Aeronautics and Astronautics, Purdue University, May 2016 – present.
- Teaching Assistant, of Aeronautics and Astronautics, Purdue University, Aug 2014 – May 2017.

### PUBLICATIONS

- Zhang, Liang, Zhenyuan Gao, Robert A Haynes, Todd C Henry, Wenbin Yu, “An anisotropic continuum damage model for high-cycle fatigue,” *Mechanics of Advanced Materials and Structures*, to appear.
- Zhang, Qi, Jiawen Xie, Zhenyuan Gao, Tyler London, David Griffiths, and Victor Oancea, “A metallurgical phase transformation framework applied to SLM additive manufacturing processes,” *Materials & Design*, vol. 166, article 107618, 2019.
- Gao, Zhenyuan, Liang Zhang, Robert A. Haynes, and Wenbin Yu, “A continuum damage model for fatigue and its integration scheme,” *American Society of Composites - 33rd Technical Conference*, 2018.

- Gao, Zhenyuan, Liang Zhang, and Wenbin Yu, “A nonlocal continuum damage model for brittle fracture,” *Engineering Fracture Mechanics*, vol. 189, pp. 481–500, 2018.
- Zhang, Liang, Zhenyuan Gao, and Wenbin Yu, “A string-based cohesive zone model for interlaminar delamination,” *Engineering Fracture Mechanics*, vol. 180, pp. 1–22, 2017.
- Gao, Zhenyuan, Liang Zhang, and Wenbin Yu, “A nonlocal constitutive model for damageable brittle and quasi-brittle materials,” 58th AIAA/ASCE/AHS/ASC Structures, Structural Dynamics, and Materials Conference, 2017.
- Gao, Zhenyuan, Liang Zhang, and Wenbin Yu, “Simulating the mixed-mode progressive delamination in composite laminates,” American Society of Composites - 30th Technical Conference, 2015.